FACULTY OF ENGINEERING OF UNIVERSITY OF PORTO

Perception-based Autonomous Underwater Vehicle Navigation for Close-range Inspection of Offshore Structures

Renato Jorge Moreira Silva

Doctoral Program in Electrical and Computer Engineering

Supervisor: Professor Andry Maykol Gomes Pinto

Second Supervisor: Professor Aníbal Castilho Coimbra de Matos

June 4, 2025

Abstract

Operation and maintenance (O&M) costs constitute a significant part of the total expenses of offshore wind power. The development of new and improved solutions for inspecting and monitoring these structures is an important contribution, fostering sustainable green energy sources, as well as making them more cost-effective. Autonomous Underwater Vehicles (AUVs) are becoming a prominent solution for these operations, however, state-of-the-art technologies still do not allow completely autonomous platforms to perform such intervention tasks due to the lack of security and reliability provided.

Therefore, this work proposes three main contributions to improve the ability of these autonomous systems of interacting with the environment. Through this thesis a novel bio-inspired AUV is presented, designed specifically to overcome current limitations in underwater intervention capabilities. Its blended wing body morphology, inspired by manta rays, provides a streamlined body where strategic thruster placement enables fine-tuned position and velocity control in 6 degrees of freedom, required for close-range inspection tasks. The vehicle's modular architecture, composed of independent navigation, perception, propulsion and power subsystems, enhances scalability, adaptability and system reliability while providing redundancy through dual power cylinders for critical operations. Real-world tests demonstrated RAYA's capabilities across multiple areas, validating its structural integrity, kinematic control, perception systems and autonomous navigation capabilities. The perception system was rigorously validated across diverse controlled environments. The inspection assessments demonstrated high accuracy in structural dimension estimation, with errors below 1.5% when reconstructing an indoor pool environment. Additionally, real-world trials validated the vehicle's seabed mapping capabilities, successfully mapping an area with depths varying between 1.71 and 2.58 meters.

This novel AUV platform lays the foundation for the development of new methodologies in fundamental building blocks of manipulation-based docking maneuvers, such as exploration and manipulation. Hence, this research proposes a coarse-to-fine approach for 3D reconstruction of underwater structures (C2FARUS) that enables systematic exploration without prior knowledge of the underwater environment. Starting with no initial information, the methodology gradually builds and refines its understanding through four interconnected stages: coarse exploration using multibeam sonar, object identification through geometric feature analysis, definition of safe inspection zones, and optimized path planning for detailed reconstruction. When benchmarked against state-of-the-art methods, C2FARUS achieved an 87.04% completeness in reconstruction tasks, with an accuracy of 0.0076 meters. Additionally, the system completed inspection paths approximately 38% faster than the other compared approaches. Real-world trials validated the method's capability to segment complex geometries and detect fine-scale components such as anodes, with relative errors below 2.83% for structural dimensions.

Finally, to advance manipulation-based docking capabilities, this work proposes NEMU, a comprehensive evaluation metric for underwater motion planning that integrates effectiveness (energy efficiency and planning time), safety (obstacle avoidance and path optimization), and adapt-

ability (accuracy of real hardware execution) considerations. The metric was extensively validated using a 6-DoF manipulator capable of lifting 10kg with high-accuracy joint positioning of 0.1º, benchmarking 22 different planners across varying complexity scenarios. Results revealed optimal planners for different operational conditions: BiEST demonstrated superior performance in low-complexity tasks with 40% lower global costs, while BKPIECE emerged as optimal for complex manipulation scenarios, showing 42% better adaptability. Real-world validation using an underwater motion capture system demonstrated the metric's reliability, with planned trajectories executed with average position errors of 0.0064 ± 0.0023 meters.

The methodologies and technologies developed through this research represent a comprehensive solution addressing critical limitations in autonomous underwater systems, marking a cutting-edge advancement for more complex intervention tasks with enhanced efficiency, safety, and reliability. This work contributes to advancing offshore operations, particularly in the growing wind energy sector where reliable inspection and maintenance capabilities are crucial for sustainable operations.

Resumo

Os custos de Operação e Manutenção (O&M) constituem uma parte significativa das despesas totais do sector da energia eólica offshore. O desenvolvimento de novas e melhores soluções para a inspeção e monitorização destas estruturas é uma contribuição importante, promovendo fontes de energia verde sustentáveis e tornando-as mais rentáveis. Os Veículos Autónomos Submarinos (AUVs) estão a tornar-se uma solução proeminente para estas operações, contudo, as tecnologias atuais ainda não permitem que plataformas completamente autónomas realizem tais tarefas de intervenção devido à falta de segurança e fiabilidade fornecida.

Desta forma, este trabalho propõe três contribuições principais para melhorar a capacidade destes sistemas autónomos de interagir com o ambiente. Através desta tese é apresentado um novo bio-inspirado AUV, projetado especificamente para superar as limitações atuais nas capacidades de intervenção subaquática. A sua morfologia de corpo alado, inspirada em raias manta, proporciona um corpo hidrodinâmico onde o posicionamento estratégico dos propulsores permite um controlo preciso de posição e velocidade em 6 graus de liberdade, necessários para tarefas de inspeção de curta distância. A arquitetura modular do veículo, composta por subsistemas independentes de navegação, perceção, propulsão e energia, melhora a escalabilidade, adaptabilidade e fiabilidade do sistema, proporcionando redundância através de cilindros de energia duplos para operações críticas. Os testes em ambiente real demonstraram as capacidades do RAYA em várias áreas, validando a sua integridade estrutural, controlo cinemático, sistemas de perceção e capacidades de navegação autónoma. O sistema de perceção foi rigorosamente validado em diversos ambientes controlados. Os ensaios de inspeção demonstraram alta precisão na estimativa das dimensões estruturais, com erros inferiores a 1,5% durante a reconstrução de uma piscina interior. Adicionalmente, testes em ambiente real validaram as capacidades de mapeamento do fundo do mar, mapeando com sucesso uma área com profundidades entre 1,71 e 2,58 metros.

Esta nova plataforma AUV estabelece as bases para o desenvolvimento de novas metodologias em blocos fundamentais de manobras de acoplamento baseadas em manipulação, como exploração e manipulação. Assim, esta investigação propõe uma abordagem grosseira-para-fina para reconstrução 3D de estruturas subaquáticas (C2FARUS) que permite exploração sistemática sem conhecimento prévio do ambiente subaquático. Começando sem informação inicial, a metodologia constrói e refina gradualmente a sua compreensão através de quatro etapas interligadas: exploração grosseira usando sonar multifeixe, identificação de objetos através de análise de características geométricas, definição de zonas seguras de inspeção e planeamento otimizado de trajetórias para reconstrução detalhada. Quando comparado com métodos do estado da arte, o C2FARUS alcançou uma completude de 87,04% em tarefas de reconstrução, com uma precisão de 0,0076 metros. Adicionalmente, o sistema completou trajetórias de inspeção aproximadamente 38% mais rápido que as outras abordagens comparadas. Ensaios em ambiente real validaram a capacidade do método para segmentar geometrias complexas e detetar componentes de escala fina como ânodos, com erros relativos abaixo de 2,83% para dimensões estruturais.

Finalmente, para avançar as capacidades de acoplamento baseado em manipulação, este trabalho propõe NEMU, uma métrica de avaliação abrangente para planeamento de movimento subaquático que integra considerações de eficácia (eficiência energética e tempo de planeamento), segurança (evitamento de obstáculos e otimização de trajetória) e adaptabilidade (precisão de execução em hardware real). A métrica foi extensivamente validada usando um manipulador com 6 graus de liberdade capaz de levantar 10kg com posicionamento de alta precisão das juntas de 0,1º, avaliando 22 planeadores diferentes em cenários de complexidade variada. Os resultados revelaram planeadores ótimos para diferentes condições operacionais: BiEST demonstrou desempenho superior em tarefas de baixa complexidade com custos globais 40% menores, enquanto BKPIECE emergiu como ótimo para cenários de manipulação complexa, mostrando 42% melhor adaptabilidade. A validação em ambiente real usando um sistema de captura de movimento subaquático demonstrou a fiabilidade da métrica, com trajetórias planeadas executadas com erros médios de posição de 0.0064 ± 0.0023 metros.

As metodologias e tecnologias desenvolvidas através desta investigação representam uma solução abrangente que aborda limitações críticas em sistemas autónomos submarinos, marcando um avanço de vanguarda para tarefas de intervenção mais complexas com eficiência, segurança e fiabilidade melhoradas. Este trabalho contribui para o avanço das operações offshore, particularmente no crescente sector da energia eólica onde capacidades fiáveis de inspeção e manutenção são cruciais para operações sustentáveis.

Acknowledgments

First and foremost, I would like to express my profound gratitude to my supervisor, Andry Pinto, whose mentorship has been invaluable. His consistent encouragement to push boundaries and strive for excellence has shaped not only this thesis but my approach to research. I am grateful not only for his academic guidance but also for his willingness to teach and encourage me at every step of this journey. His character and dedication have set an inspiring example that I will carry forward.

I am equally thankful to my co-supervisor, Aníbal Matos, for sharing his wealth of experience and providing crucial advice throughout this process. His efforts in ensuring the necessary conditions for the completion of this thesis were instrumental to its success.

The collegiate environment has been enriched by an exceptional group of colleagues who became dear friends. To Daniel Campos, Maria Inês, Rafael Claro, Pedro Almeida, João Dionísio, Francisco Neves, Lourenço Pinho, João Marques, Diogo Silva, and Eduardo Gonçalves - thank you for the incredible memories we've created over these past five years. From our adventurous car rides to Vigo and unforgettable trips to Girona, to the range of missions we tackled together - from simple operations in Leixões to the complex and exhilarating challenges in Viana. Your support with my Nessie project, no matter how crazy it seemed, has been invaluable. The group we formed has been a source of great pride, and each of you has left an indelible mark on this journey.

A special acknowledgment goes to my unique colleague Pedro Leite, a person whom I am immensely proud to call friend for the past decade. From our first year together, we have grown and faced countless challenges side by side. Whether during late-night gaming sessions or intense work hours, your consistent friendship and support since day one have been invaluable. Throughout these years, we've achieved numerous milestones together, with this PhD being perhaps the craziest one of all. Having you by my side has been an immeasurable source of strength. You're the friend whose support never wavered, even during our wild nights at Queima. The one who kept me laughing with your constant pranks, who taught me invaluable lessons about life, and who I'll miss tremendously as we move forward in our careers. Words cannot fully express what your friendship means to me, and I will always be in your debt. These ten years of friendship have been a gift, and I wish you all the happiness in the world.

With all my heart, I want to thank my girlfriend, Ana Claro, for all the support and love. Her encouragement has pushed me to become a better person across all aspects of life - academically, professionally, and personally. Her unconditional love, shared adventures, and companionship through difficulties have been invaluable. Her unique view of life has inspired me to cross boundaries I never thought possible, and my love and gratitude for her grow with each passing day. Her wisdom and presence have made this challenging journey not just manageable, but meaningful.

Family has been my foundation throughout this process. I am grateful to my brother, Pedro Silva, for his timely support and ability to provide both assistance and necessary distractions, and to Isa, my sister's girlfriend, who has embraced me as a brother and brought additional joy to

my life. I extend my gratitude to my girlfriend's parents, Né and Cândida, whose support and kindness have made them an integral part of my support system. To my father, Jorge Silva, who has been my lifelong role model - thank you for all your support and love. You have not only supported every decision I've made but have shown me through example what it means to work hard and pursue your dreams. And finally to my mother, Fátima Silva, whom I admire and love. Her unwavering strength and constant encouragement have not only made it possible for me to pursue my dreams with no hesitations, but have also shown me what true resilience looks like. I hope they are as proud of me as I am of them.

I extend my sincere thanks to all those who contributed directly or indirectly to the completion of this doctorate - your impact, whether large or small, has helped shape this journey.

The completion of this thesis would not have been possible without this network of support, guidance, and encouragement. Each person mentioned here has contributed uniquely to this achievement, and for that, I am eternally grateful.

Renato Jorge Moreira Silva

Official Acknowledgments

Renato Jorge Moreira Silva acknowledges the Portuguese Government through the FCT (Foundation for Science and Technology) for the PhD grant 2020.08349.BD (DOI: https://doi.org/10.54499/2020.08349.BD).
This work was also financed by the ERDF – European Regional Development Fund through the Operational Programme for Competitiveness and Internationalisation - COMPETE 2020 under the PORTUGAL 2020 Partnership Agreement - The EU Framework Programme for Research and Innovation 2014-2020, under grant agreement No. 871571.

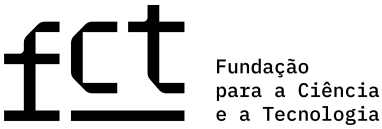

Renato Jorge Moreira Silva

"The future belongs to those who believe
in the beauty of their dreams."

Eleanor Roosevelt

Contents

List of Figures

List of Tables

Abbreviations and Symbols

2D	Two-dimensional
3D	Three-dimensional
AO	Asymptotic Optimality
ATSP-PL	Asymmetric Travelling Salesman Problem, with Precedence Loss
AUV	Autonomous Underwater Vehicle
BiEST	Bi-directional Expansive-Spaces Trees
BiTRRT	Bi-directional Transition-based Rapidly-exploring Random Tree
BWB	Blended Winged Body
C2FARUS	Coarse-to-Fine Approach for 3D Reconstruction of Underwater Structures
CAD	Computer-aided design
CALM	Catenary Anchor Leg Mooring
CFRP	Carbon Fiber–Reinforced Polymer
CoB	Center of Buoyancy
CoM	Center of Mass
Consistent-MDMTSP	Consistent Multiple Depot Multiple Traveling Salesman Problem
CPP	Coverage Path Planning
CRAS	Centre of Robotics and Autonomous Systems
CWIF	Caithness Windfarm Information Forum
DCL	Dynamic Control Layer
DH	Denavit–Hartenberg
DoF	Degrees of Freedom
DP	Dynamic Programming
DVL	Doppler Velocity Log
EEPPA	Energy-Efficient Path Planning Algorithm
Eff	End-Efector
EKF	Extended Kalman Filter
EST	Expansive-Spaces Trees
EU	European Union
FLS	Forward-looking sonars
FMT	Fast Marching Tree
FOG	Fiber Optic Gyro
FOV	Field Of View
GA	Genetic Algorithm
GNAT	Geometric Nearneighbor Access Tree
GPS	Global Positioning System
IMU	Inertial Measurement Unit

INS	Inertial Navigation System
KCL	Kinematic Control Layer
KPIECE	Kinodynamic motion Planning by Interior Exterior Cell Exploration
LBTRRT	Lower Bound Tree Rapidly-exploring Random Tree
LiDAR	Light Detection and Ranging
MBES	Multibeam Echosounder
MPP	Motion Planning Problem
MVS	Multiview stereo
NBV	Next-Best-View
NEMU	plaNner Evaluation Metric for Underwater intervention
O&M	Operations and Maintenance
OMPL	Open Motion Planning Library
OWF	Offshore Wind Farm
PCA	Principal Component Analysis
PDST	Path-Directed Subdivision Tree
POM	Polyoxymethylene
ProjEST	Projection Expansive-Spaces Trees
PRM	Probabilistic RoadMap
ROS	Robot Operating System
ROV	Remotely Operated Vehicle
RRT	Rapidly-exploring Random Tree
RRT*	Rapidly exploring Random Tree Star
RTK	Real Time Kinematic
SOV	Service Operation Vessel
SPARS	SPArse Roadmap Spanner
STRIDE	Search Tree with Resolution Independent Density Estimation
SW	Sliding Window
TRRT	Transition-based Rapidly-exploring Random Tree
TSP	Travelling Salesman Problem
UAV	Unmanned Aerial Vehicle
UK	United Kingdom
VP	View Planning
WMO	World Meteorological Organization

Chapter 1

Introduction

The transition to green energy is critical in addressing the pressing challenges of climate change and environmental degradation. Among renewable energy sources, wind power has emerged as a key contributor, providing sustainable and clean electricity to meet the growing global demand [1]. In 2023 alone, Europe installed 18.3 GW of new wind capacity, with onshore wind accounting for 79% of new installations (14.5 GW). Looking ahead, the European Union (EU) is projected to install 200 GW of new wind power capacity over 2024–2030, averaging 29 GW annually. However, to meet its 2030 climate and energy targets, the EU must achieve an average annual build-out of 33 GW [2].

In this context, offshore wind energy emerges as a key solution. Compared to onshore wind turbines, offshore wind farms (OWFs) offer several advantages that allows the scaling of the turbines to increase the total energy production. This benefit makes OWFs an attractive solution for achieving energy transition goals, despite the significant investment required. Thus, offshore wind power, a critical component of Europe's energy transition, is expected to ramp up significantly towards the end of the decade. Forecasts indicate that by 2030, the EU's installed wind power capacity will reach 393 GW, with a target of 425 GW [3, 2]. These efforts align with the European Union's broader ambition to become the first climate-neutral continent by 2050, a goal enshrined in the European Green Deal [4]. Offshore renewables are pivotal in achieving this target, providing a sustainable pathway to decarbonizing energy systems and reducing reliance on fossil fuels [5]. Initiatives such as WindFloat Atlantic and Atlantis projects highlight the importance of offshore wind farms in harnessing the vast energy potential of maritime environments.

The exponential growth of annual offshore wind installations (see figure 1.1) calls for cyclical monitoring and inspection to ensure the safety and efficiency of wind farm facilities. Operation and maintenance costs constitute a significant part (may account for up to 30 %) of the total costs of offshore wind power [6]. Offshore wind farm (OWF) operations and maintenance (O&M) activities are particularly challenging due to the large-scale environment and the complexity of the structures involved, both below and above water. Floating wind turbines, for example, are secured to the seabed through multiple mooring lines attached to their support structure. These underwater moorings require regular inspection and maintenance to detect potential cracks and

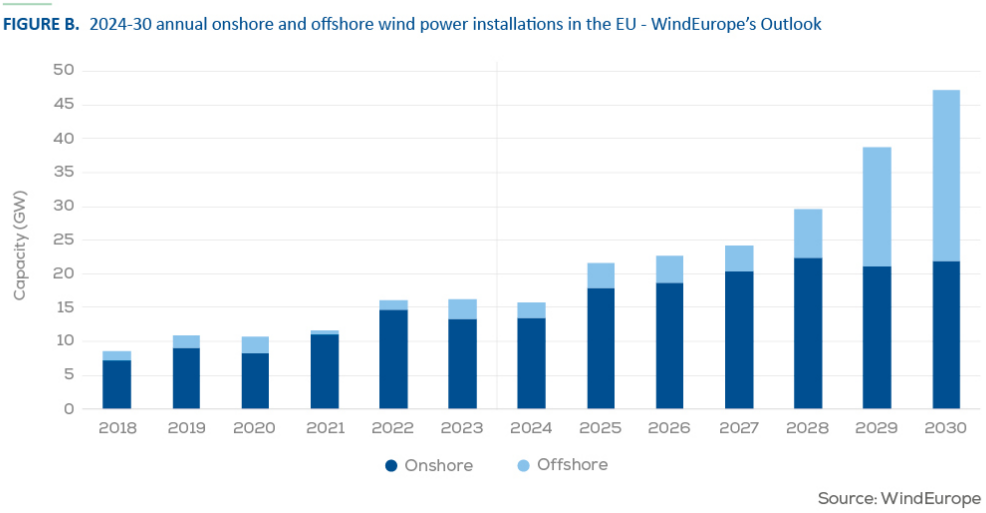

Figure 1.1: Annual onshore and offshore wind power installations in the EU [2].

material fatigue. Due to the deep-water environment, surface-level observations are insufficient [7]. Other inspections include surveys of cable arrays, seabed, and submerged structures to ensure there is no structural damage or sediment displacement. Additionally, above-water inspections of emersed structures, such as wind turbine blades, towers, and transition pieces, are essential to maintain safety and longevity.

Therefore, the development of improved and new solutions for operation and maintenance of offshore structures is crucial to make offshore wind power more cost-effective and safe. By deploying autonomous robotic systems, wind farm operators can reduce total investment costs by more than 20% while enhancing safety conditions for maintenance technicians [8]. Robotic-based systems such as remotely-operated vehicles, already play an important role in conducting underwater surveys. Nevertheless, many of these technologies typically require manual deployment, remote operation and manual retrieval of the systems [9]. These limitations highlight the need for innovative solutions to ensure continuous and reliable inspections. Autonomous systems, such as Autonomous Underwater Vehicles (AUVs), offer a promising alternative by enabling efficient and high-precision monitoring of submerged structures while minimizing risks to human operators [10, 11].

AUVs have already demonstrated their ability to complete complex inspection tasks with high precision and reliability and they are increasingly being considered as alternatives to conventional inspection methods involving divers or Remotely Operated Vehicles (ROVs) [10]. AUVs can carry advanced sensors, including high-resolution multibeam sonars, synthetic aperture sonars, and high-definition cameras, enabling detailed inspections and hydrographic surveys [12]. These vehicles are now widely used for various offshore applications, including pipeline inspections [13], rig move surveys, harbor inspections [14] and cathodic protection surveys with high precision,

using advanced sensing and navigation systems [15]. As technology advances, AUVs will play an increasingly significant role in offshore operations and ocean exploration.

1.1 Motivation

Autonomous Underwater Vehicles offer a promising alternative, potentially enabling continuous, cost-effective, and safer underwater operations. However, the development of intervention-capable AUVs faces several fundamental technical and operational challenges in areas such as close-range sensing, workspace optimization, and manipulation planning, that current solutions have not adequately addressed [16, 17].

The first major challenge lies in design and hydrodynamic efficiency. The conventional morphology of current intervention AUVs represents a significant limitation in their operational capabilities. Traditional designs typically follow either torpedo-shaped configurations, optimized for survey missions but poorly suited for intervention tasks [18], or open-frame structures that prioritize payload capacity and manufacturing simplicity over hydrodynamic efficiency. These geometric approaches severely limit intervention capabilities. The flat surfaces and sharp edges characteristic of box-like designs generate substantial drag and unpredictable vortex formations when the vehicle attempts to maintain position in varying currents [19]. This becomes particularly problematic during intervention operations, where the vehicle must simultaneously manage external disturbances and manipulator reaction forces while maintaining precise positioning. The geometric configuration of these vehicles leads to compromises in manipulator placement and integration. Traditional designs typically require the manipulator to be mounted on the front or bottom of the vehicle, creating an unfavorable distribution of forces during intervention tasks. This arrangement often results in a limited manipulator workspace and frequently requires vehicle movement to compensate for the manipulator's restricted reach, adding complexity to intervention operations. Moreover, this configuration generates thruster turbulence in the manipulation workspace, disrupting manipulation tasks.

Some existing vehicles have operational weights close to 1000 kg [20, 21], with some reaching up to 3500 kg [22]. This excessive weight has cascading effects throughout the system's operation cycle. The deployment and recovery of such heavy vehicles require specialized handling equipment and support vessels, significantly increasing operational costs and complexity [23]. The substantial mass also impacts the vehicles' dynamic behavior, requiring more powerful thrusters and consequently higher energy consumption to maintain precise positioning during intervention tasks. The weight challenge becomes particularly acute during intervention operations, where the vehicle must maintain stable positioning while managing additional forces from manipulation activities. The high inertia of these heavy vehicles makes them less responsive to control inputs and more susceptible to disturbances, requiring more energy and more sophisticated control systems to maintain the precise positioning necessary for intervention tasks.

These limitations significantly affect AUVs' ability to perform precise inspection and intervention tasks, particularly when operating near underwater structures. The need for accurate

three-dimensional (3D) data gathering and close-range navigational capabilities becomes especially critical when creating detailed environmental representations required for autonomous operations. Accurate 3D representations of underwater structures have become increasingly crucial across multiple industries and applications. In the offshore energy sector, where high value infrastructures operate continuously underwater, these models serve as the foundation for critical maintenance decisions and structural integrity assessments. Regular comparison of detailed 3D models allows engineers to detect and monitor structural deterioration, biofouling accumulation, and potential damage before they lead to costly failures [24]. For offshore wind farms, where a single day of downtime can result in substantial revenue losses, these representations enable predictive maintenance strategies that optimize operational efficiency while minimizing intervention costs. These representations are also especially crucial for enabling long-term autonomous operations through underwater docking capabilities as high-fidelity representations can significantly enhance autonomous docking operations [25]. To achieve this goal, the vehicle must not only understand the exact geometry of the docking structure but also have detailed knowledge of potential obstacles. This level of environmental awareness becomes particularly crucial in scenarios where docking stations are integrated into existing offshore infrastructure. The transition from short-term inspection missions to persistent autonomous operations makes underwater docking stations critical [26]. These docking stations serve as vital infrastructure for battery recharging, data transfer, and mission updates, effectively extending the operational duration of autonomous vehicles from hours to months. However, successful autonomous docking operations require accurate models of the docking structures and their surrounding environment. The precision of these models directly impacts the reliability and safety of docking maneuvers, where even small positioning errors could result in collision or failed attempts.

The challenges of close-range inspection operations present a distinct set of problems that fundamentally affect the quality and completeness of underwater structure reconstruction. Current underwater inspection systems rely primarily on visual and sonar technologies [27]. However, in underwater environments, vision-based underwater vehicles commonly encounter challenges such as turbidity and low illumination. Sonar imaging systems serve as an alternative to optical imaging systems to address such disturbances since acoustic signals can propagate over longer distances, even under dark and turbid conditions [28]. Nonetheless, multibeam sonars acquire sequential data, making complete 3D representation of underwater structures challenging: the vehicle must follow precise trajectories to ensure thorough coverage from various angles and perspectives. The nature of multibeam sonar data acquisition adds another layer of complexity to the inspection task. Unlike other sensing modalities, sonar data quality is highly dependent on the distance between the sensor and the target structure [29]. Operating too far from the structure results in low-resolution data and sparse point clouds, while moving too close introduces navigation risks and potential blind spots in the sensor coverage. This creates a fundamental challenge in determining the optimal inspection distance that balances data quality with navigational safety. Furthermore, the limited field of view of multibeam sonars means that multiple passes are often required to capture complete structural information, increasing the complexity of path planning

and execution. Current systems also lack effective methodologies for guaranteeing high coverage while maintaining optimal data acquisition conditions. The absence of standardized approaches for defining and executing inspection trajectories often results in ad-hoc solutions that may miss critical areas or fail to capture sufficient detail for subsequent intervention tasks. This limitation becomes particularly apparent when dealing with complex structures where complete coverage requires carefully planned viewpoints and systematic execution of inspection patterns.

To address these challenges, this thesis proposes advancing autonomous underwater vehicle technology through three interconnected innovations aimed at enabling persistent autonomous operations. The first contribution introduces a bio-inspired vehicle design specifically optimized for close-range inspection and intervention tasks. This novel design tackles the limitations of traditional AUV platforms by designing a vehicle capable of acquiring heterogeneous data from multiple sensors (multibeam sonar, profiler sonar, cameras), while its morphology and manufacturing approach optimize maneuverability, intervention capabilities and hydrodynamic efficiency. The bio-inspired shape enables stable hovering while performing manipulation tasks and fine-tuned control in all 6 degrees of freedom (DoF), essential capabilities for close-range operations, that in conjunction with the integrated sensors enable close-range inspection capabilities and the ability to create accurate 3D underwater environmental representations. These design innovations make it possible for a single vehicle to execute complex inspection and intervention tasks such as manipulation-based docking.

The second contribution presents a coarse-to-fine approach for underwater exploration, addressing a fundamental building block for persistent autonomous operations. This methodology, that starts without prior knowledge of the environment, enables close-range navigation to structures while ensuring high resolution and accuracy sonar data acquisition, allowing AUVs to create accurate 3D models of their environment. Through inspection patterns definition and trajectory planning based on sonar data specifications, the system ensures high structure coverage and consistent data collection for comprehensive environmental mapping. This capability will change AUVs short-term deployment platforms to persistent autonomous systems that can operate for extended periods.

Finally, the third contribution tackles the manipulation problem, the other fundamental building block for persistent autonomous operations. To this end, this thesis introduces a comprehensive evaluation metric for underwater manipulation strategies, designed to enable the comparison of state-of-the-art manipulation planners. This metric provides standardized methods for assessing and comparing different manipulation approaches, considering multiple variables according to the requirements of underwater robots for O&M tasks: the energy used by the manipulator throughout an entire mission, the distance to the closest obstacle, the path length and the accuracy of the real hardware to executed the motion planned. Through quantitative evaluation of manipulation strategies in realistic underwater scenarios, this metric will enable the selection of optimal approaches for docking procedures, advancing the development of reliable autonomous docking capabilities through manipulation.

1.2 Objectives

The main goal for this work is to advance persistence autonomous underwater operations through the development of a novel bio-inspired AUV while tackling fundamental building blocks such as exploration and manipulation, to enable docking maneuvers. This research work is focused in four objectives:

- Design and validate a bio-inspired intervention-capable AUV that achieves enhanced hydrodynamic efficiency through a blended wing body design, enables stable operation during manipulation tasks with a 6 DoF arm and maintains precise control in all 6 DoF during close-range operations;
- Develop a coarse-to-fine methodology for underwater structure exploration that enables close-range navigation to achieve fine 3D representations of underwater structures through high resolution and accuracy sonar data acquisition;
- Establish a metric for underwater motion planning evaluation that provides quantitative evaluation for assessing planner performance, validates motion planning strategies in realistic underwater scenarios and enables objective comparison of different planning approaches;
- Validate the developed systems through comprehensive real-world experiments that verify the structural integrity and kinematic control of the developed AUV, demonstrate its autonomous navigation capabilities in different scenarios, assess the reconstruction method capability in exploring and segmenting submerged objects, and benchmark multiple planners applied to a 6 DoF manipulator in geometrically constrained scenes;

1.3 Contributions

This section highlights the key contributions of this research to the field of autonomous underwater inspection, particularly for offshore infrastructure. The innovations presented herein have advanced the capabilities of AUVs, demonstrating significant practical impact and potential real-world application.

The main contributions can be categorized into three core areas:

1. A novel bio-inspired AUV for Inspection and Intervention of Underwater Structures:
    - A new bio-inspired AUV (RAYA) prepared to equip a 6 DoF manipulator to assist in the operations and maintenance activities of underwater structures. Its bio-inspired blended winged body morphology provides a more streamlined body than other state-of-the-art intervention AUVs, and, by enabling a strategic thruster configuration that achieves higher torques, allows the execution of complex manoeuvres in all 6 DoFs needed for close range inspection and intervention missions. This possibility is supported by an analysis of the vehicle's buoyancy and gravitational forces that ensures

the vehicle's capacity to perform any manoeuvres in a 3D space, as well as hovering while operating a manipulator arm with a 5 kg payload for intervention missions.

- Featuring a modular architecture with five modules, addressing navigation, perception, propulsion, and system power separately, this AUV design enhances scalability and adaptability, with easier upgrades and maintenance, thanks to the independence of each module. The inclusion of two power cylinders guarantees a failsafe mechanism, as each cylinder can independently provide the AUV with sufficient locomotor capacity for rescue.
- RAYA is a heavily research oriented vehicle, thus, the perception, localization, and navigational sensors and actuators integrated within this AUV build were specifically selected to facilitate advanced autonomous tasks - such as intervention, inspection, and navigation - and were evaluated through qualitative and quantitative assessments in various real-world environments. This comprehensive testing aimed to verify the structural integrity and kinematic control of the vehicle, validate the accuracy of 3D reconstructions, acquire seabed data points for mapping via autonomous trajectories, and conduct a visual inspection of an underwater structure and the ocean floor.

2. C2FARUS - A coarse-to-fine approach for 3D reconstruction of underwater structures using a multibeam sonar

    - A novel coarse-to-fine approach called C2FARUS enables AUVs to systematically explore, detect, and reconstruct underwater structures while addressing the challenge of close-proximity navigation. By defining navigational regions based on object dimensions and multibeam sonar specifications, the system ensures high-resolution sonar data capture through close-range inspection while mitigating associated risks, ultimately enabling fine 3D reconstruction of underwater structures.
    - C2FARUS enhances 3D representations accuracy and completeness by optimizing data acquisition through a combined Genetic Algorithm (GA) and Rapidly-exploring Random Tree (RRT) path planning approach, which generates efficient inspection trajectories from a combination of inspection scans and transitional paths, to capture multiple angles and perspectives while minimizing blind spots, thereby addressing common issues of sparse point clouds and limited data in underwater environments.
    - Experiments conducted in a controlled underwater environment using real data, provided validation for the developed method in exploring and segmenting complex submerged geometries, including the detection of critical smaller components like anodes. The system achieved remarkable dimensional accuracy with a maximum relative error of only 3.22% in object measurements.
    - C2FARUS was compared against two state-of-the-art methods adapted for autonomous underwater vehicles to evaluate the effectiveness of the proposed method to efficiently and safely achieve fine 3D reconstructions. The proposed coarse-to-fine approach

achieved the highest completeness and accuracy at 87.04% and 0.0076 meters, respectively.

3. NEMU - A new planner evaluation metric for underwater intervention

   - A new planner evaluation metric composed by several heterogeneous parameters to evaluate the motion planner for underwater robots in specialized tasks, such as the inspection and monitoring of man-made structures.
   - Comprehensive validation and benchmarking of multiple motion planners in realistic underwater scenarios, utilizing a 6 DoF electrified robotic arm and a motion capture system to evaluate trajectory performance during pick and place operations in geometrically constrained environments.
   - Comprehensive analysis of external underwater forces (including buoyancy and drag) on manipulator performance through qualitative and quantitative evaluations across multiple scenarios, comparing simulated trajectories against real motions captured by a 3D underwater motion capture system.

1.4 Publications

1. **Silva, R., Matos, A., Pinto, A.M.** (2022). *Multi-criteria metric to evaluate motion planners for underwater intervention*. Autonomous Robots, 46, 971–983. https://doi.org/10.1007/s10514-022-10060-x

2. **Silva, R., Matos, A., Pinto, A.M.** (2024). *Raya: A Bio-Inspired AUV for Inspection and Intervention of Underwater Structures*. Submitted in IEEE Access.

3. **Silva, R., Matos, A., Pinto, A.M.** (2024). *A Coarse-to-Fine Approach for 3D Reconstruction of Underwater Structures Using Multibeam Sonar*. Submitted in IEEE Journal of Oceanic Engineering.

4. **R. Silva, P. Pereira, A. Matos and A. Pinto**. "Volumetric Gradient-Aware Methodology for the Exploration of Foreign Objects in the Seabed," OCEANS 2024 - Halifax, Halifax, NS, Canada, 2024, pp. 1-4, https://doi.org/10.1109/OCEANS55160.2024.10754344.

5. **Agostinho, L.R., Ricardo, N.C., Silva, R.J., Pinto, A.M.** (2021). *A Modular Inductive Wireless Charging Solution for Autonomous Underwater Vehicles*. 2021 IEEE International Conference on Autonomous Robot Systems and Competitions (ICARSC), Santa Maria da Feira, Portugal, pp. 68-73. https://doi.org/10.1109/ICARSC52212.2021.9429785

Master's thesis developed from this research:

1. **Vale, T.** (2022). *Scheduling Algorithms for Underwater Pick and Place Tasks for Offshore WindFarm Intervention Tasks*. M.Sc. dissertation. https://hdl.handle.net/10216/145056

My contribution to this Master's thesis included insights and expertise in underwater manipulation, helping shape the methodology and experimental design. This collaboration leveraged the motion planning evaluation framework developed in this thesis to analyze scheduling algorithms for underwater pick-and-place operations.

1.5 Document Structure

This document is divided in 6 major components:

- Chapter 1 introduces the research context, highlighting the significance of autonomous underwater vehicles in offshore wind farm inspections. It presents the key challenges, research objectives, and contributions of this work;

- Chapter 2 presents a comprehensive literature review examining autonomous underwater vehicles and their capabilities for operation and maintenance inspections. This chapter explores relevant literature on state-of-the-art environment exploration techniques using both visual and sonar technologies, and evaluates common motion planning approaches for different degrees of freedom robotic manipulation;

- Chapter 3 details the development of a novel bio-inspired AUV (RAYA) designed specifically for underwater navigation and manipulation. The vehicle features a modular architecture that enhances safety, scalability, and maintainability through independent subsystems. Extensive field trials demonstrate the RAYA's capabilities across multiple domains: structural integrity, kinematic control, 3D reconstruction accuracy, autonomous seabed mapping, and visual inspection of submerged structures;

- Chapter 4 introduces a Coarse-to-Fine Approach for 3D Reconstruction of Underwater Structures (C2FARUS) using sonar data. This method enables AUVs to systematically explore, detect, recognize, and reconstruct submerged structures to support future intervention tasks. The chapter presents extensive experimental validation in simulated and controlled underwater environments, demonstrating the system's capability to segment complex geometries and detect fine-scale components such as anodes. Comparative analysis against two state-of-the-art methods validates C2FARUS's performance;

- Chapter 5 introduces NEMU, a novel evaluation metric for assessing motion planners in underwater manipulation tasks. The chapter presents comprehensive benchmarking of various planners for a 6-DoF manipulator performing pick-and-place operations in constrained underwater environments. Through both qualitative and quantitative analyses, the study presents a benchmark of multiple motion planners in a controlled underwater environment captured using a 3D underwater motion capture system, validating the metric's effectiveness in identifying optimal planning strategies;

- Chapter 6 synthesizes the key research contributions and findings of this thesis. It summarizes the novel developments in bio-inspired AUV design, underwater exploration methodology, and underwater manipulation planning, while highlighting their practical impact on offshore wind farm inspection capabilities;

Chapter 2

Literature review

The use of autonomous underwater vehicles in inspection and maintenance operations represents a transformative approach for offshore industries, offering enhanced safety and operational capabilities in challenging underwater environments. This paradigm shift involves not only the deployment of AUVs for basic survey missions but also the integration of sophisticated capabilities such as underwater manipulation, precise navigation in close proximity to structures, and autonomous exploration of underwater environments. The evolution from traditional methods using human divers and remotely operated vehicles to autonomous systems has driven innovations in vehicle design, perception systems, and motion planning strategies to address the unique challenges of underwater operations.

This chapter reviews the state-of-the-art in autonomous underwater robotics, particularly focusing on developments relevant to offshore inspection and intervention tasks. First, Section 2.1 provides an overview of current practices for underwater inspection on offshore wind farms, highlighting their limitations, and defining solutions to allow autonomous inspection to be explored. Section 2.2 examines existing AUV platforms designed for intervention capabilities, analyzing their morphologies, control architectures, and operational limitations. Next, Section 2.3 explores state-of-the-art approaches for 3D exploration, tracing their evolution from aerial applications to underwater environments, and analyze both model-based and model-free approaches. Section 2.4 reviews motion planning strategies for underwater manipulation, considering the specific challenges of coordinating vehicle and manipulator movements in subsea environments. Finally, Section 2.5 presents a critical review of the current state of autonomous underwater systems, identifying key technological gaps and research opportunities that motivate the contributions of this thesis. Throughout this review, we identify current limitations in existing approaches and highlight the research gaps that this thesis aims to address.

2.1 General overview

Offshore wind farms are critical assets for renewable energy production, requiring regular operation and maintenance activities to ensure their reliability, safety, and efficiency. O&M tasks

encompass a wide range of activities, including monitoring the performance of turbines, repairing structural components, and maintaining subsea assets. Given the harsh marine environment and the distributed nature of offshore wind farms, O&M is one of the most challenging and cost-intensive aspects of offshore energy operations. The complexities of O&M in offshore wind farms arise from several interrelated factors [30, 31, 32]:

- **Remote location**: Offshore wind farms are typically located in deep waters far from shore to maximize wind resources and minimize visual and noise impacts. This remote location increases the logistical challenges of accessing and maintaining the infrastructure;
- **Harsh environmental conditions**: Severe weather including strong currents, high waves, and unpredictable weather, further complicate operations, leading to delays, higher costs, and increased risks to personnel and equipment;
- **Highly Specialized Workforce**: The necessity for skilled technicians trained in offshore safety and extreme working conditions is highlighted as a significant cost driver in O&M operations;
- **Expensive Equipment**: Specialized vessels, including Service Operation Vessels (SOVs) and jack-up vessels, are essential for transporting technicians and heavy equipment or replacing major components like blades and gearboxes. These vessels represent substantial capital and operational costs;
- **Limited Accessibility**: Harsh sea conditions restrict safe access to turbines, delaying maintenance and leading to increased downtime.

Offshore wind farms rely on a complex network of underwater infrastructure that is essential for the generation, transmission, and distribution of renewable energy. The key underwater components that require close inspection and maintenance include the foundations supporting the wind turbines, the subsea cables responsible for transmitting electricity to shore, and the scour protection systems installed to mitigate seafloor erosion. Maintaining the structural integrity of the wind turbine foundations is a critical underwater operation and maintenance task. These substructures, typically consisting of large steel or concrete monopiles, jackets, or gravity-based structures, depending on water depth and seabed characteristics [33], must be thoroughly examined for signs of corrosion, damage, or deformation. Regular inspection of welds, joints, and transition pieces is essential, along with monitoring the condition of corrosion protection systems such as sacrificial anodes and protective coatings [34]. The subsea cable network forms another crucial component that requires regular maintenance. This network includes both inter-array cables connecting individual turbines and export cables transmitting power to shore. Critical O&M tasks include inspecting cable burial depth to ensure proper protection, essential for protection against mechanical damage and excessive heating and monitoring for exposure or free spans that could lead to damage [35]. Additionally, regular thermal imaging and electrical testing are performed to detect potential failures before they occur [36]. Scour protection systems, designed to prevent erosion around

foundation structures, require ongoing monitoring and maintenance. Typical solutions like riprap protection and rockbags, need regular inspection to verify their position and integrity [37]. Multibeam echosounder (MBES) bathymetry survey and side scan sonar survey using service vessels or ROVs are the two most used methods [38].

Human divers and remotely operated vehicles have been heavily used for underwater inspection of offshore wind farm infrastructure [39]. However, while effective for detailed close-range inspection and intervention tasks, professional divers face severe operational constraints such as restriction to depths, limited bottom time due to decompression requirements and operational weather conditions and sea states. The World Meteorological Organization (WMO) uses the term 'sea state' to describe the local conditions of the sea surface over a period of approximately 30 minutes, particularly focusing on wind waves and swell patterns resulting from wind interaction [40]. These conditions are classified according to the Douglas Sea Scale, as shown in table 2.1, providing a standardized method for describing sea surface conditions. Additionally, diving operations in offshore environments carry significant risks [41]. Thus, ROVs emerged as a solution to overcome some limitations of human diving operations, enabling inspection at greater depths and in more challenging conditions. However, the usage of ROVs require a dedicated surface vessel which is operating the ROV during the complete mission and the umbilical connection, while ensuring a steady communication with the operator, restricts vehicle maneuverability.

Table 2.1: Douglas Sea Scale [40].

Degree	Wave height (m)	Description
0	0	Calm (glassy)
1	0-0.1	Calm (rippled)
2	0.1-0.5	Smooth (wavelets)
3	0.5-1.25	Slight
4	1.25-2.5	Moderate
5	2.5-4	Rough
6	4-6	Very rough
7	6-9	High
8	9-14	Very high
9	> 14	Phenomenal

Autonomous Underwater Vehicles offer several significant advantages for offshore inspection operations. Economically, these vehicles can operate continuously for extended periods without the need for costly support vessels and large crews that are typically required for ROV operations. The ability to carry multiple sensor types simultaneously enables AUVs to collect comprehensive datasets during a single mission. Modern AUVs can integrate visual cameras, multibeam sonars, and various environmental sensors, providing rich, multi-modal data for inspection and monitoring tasks. However, current AUV limitations particularly relevant to offshore wind farm operations include vehicle design inefficiencies, with many existing intervention-capable AUVs relying on designs that compromise maneuverability and energy efficiency. The lack of systematic approaches for underwater exploration presents another critical challenge. Additionally, underwater

manipulation remains a significant hurdle, with most existing systems requiring specific solutions tailored to the unique challenges.

Therefore, to address these challenges, this review will highlight the current state-of-the-art in AUV technology for offshore wind farm inspections, focusing on three key areas:

- Available AUV solutions: explore different AUV platforms, their design approaches and impact on operational capabilities;
- Three-dimensional exploration methodologies: study techniques for processing visual and sonar data, later focusing on methods that address the creation of underwater 3D representations;
- Motion planning strategies for underwater manipulation: analyze current state-of-the-art algorithms for motion planning in aerial context and the specific solutions developed in the underwater domain.

2.2 Autonomous underwater vehicles

Autonomous underwater vehicles have evolved significantly over the last decades, with designs optimized for different operational requirements. This vehicles offer several significant advantages over traditional inspection methods, making them increasingly attractive for offshore operations. AUVs operate with minimal human intervention during mission execution, relying on pre-programmed objectives that are carried out autonomously once the vehicle is deployed. This autonomous operation not only reduces the potential for human error during critical mission phases but also enhances operational reliability. Additionally, unlike ROVs, AUVs operate without a physical tether, significantly improving their maneuverability and access capabilities. The absence of an umbilical eliminates the risk of entanglement with underwater structures and removes the drag forces that typically constrain ROV movements, enabling AUVs to operate effectively in more complex environments [42].

These advantages have driven significant developments in AUV technology, leading to specialized vehicles optimized for different operational requirements. Current AUV designs can be broadly categorized into two main classes based on their operational capabilities: survey-class AUVs focused on data collection and environmental monitoring, and intervention-capable AUVs designed for physical interaction with their environment. Survey-class AUVs are primarily designed for data collection and environmental monitoring missions, characterized by their streamlined, torpedo-shaped designs that optimize hydrodynamic efficiency and endurance. These vehicles can complete a variety of subsea tasks in civil and military fields, such as bathymetric mapping [43], mine hunting [44, 45], ocean pollutant monitoring [46] and pipeline following and inspection [47]. Some research and commercial solutions present in the state-of-the-art (figure 2.1) are:

- The HUGIN family of AUVs [52], developed by Kongsberg Maritime, represents one of the most successful commercial platforms in this category. Recent HUGIN series operates

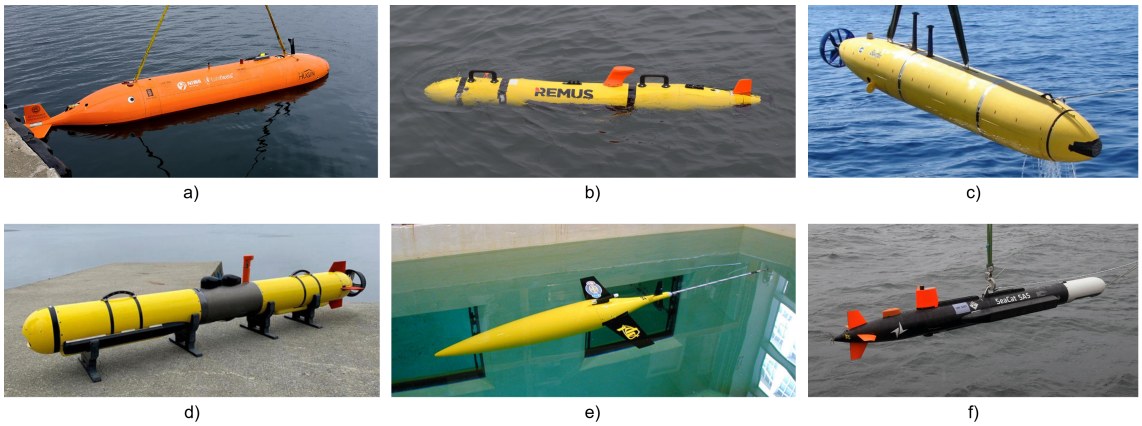

Figure 2.1: Different survey-class AUVs available in the state-of-the-art: (a) HUGIN 3000 [48]. (b) REMUS 100 [49]. (c) Bluefin-21 [50]. (d) Iver4-900 [51]. (e) Seaglider[1]. (f) Seacat[2].

at depths ranging up to 6000 meters, with mission durations extending up to 100 hours. These vehicles are typically equipped with advanced sensor payloads including multibeam echosounders, and sub-bottom profilers, cameras and volume search sonar, making them particularly effective for detailed seabed mapping and inspection tasks [53, 54]. These vehicles feature enhanced autonomy and navigational accuracy through the integration of inertial navigation system (INS), Doppler velocity log and global positioning system [55].

- The REMUS (Remote Environmental Monitoring UnitS) series, particularly the REMUS 100, has become an industry standard for shallow water operations. The REMUS series can operate in depths up to 6000 meters and is widely deployed for search and recover missions, mine countermeasures [56], seabed mapping [57] and environmental monitoring [58]. Its compact size and light weight make it particularly suitable for rapid deployment from small vessels. The REMUS 100 is equipped with a DeltaT multibeam echosounder, a sidescan sonar, GPS, IMU, DVL and a depth sensor [59].

- Bluefin Robotics' vehicles, notably the Bluefin-21, represent another significant development in survey-class AUVs. These vehicles incorporate modular designs that allow for mission-specific sensor configurations while maintaining the hydrodynamic efficiency characteristic of torpedo-shaped vehicles. The Bluefin-21 can operate at depths up to 5000 meters, making it suitable for deep-sea survey operations [60].

- ATLAS ELEKTRONIK's SeaCat AUV[1] exemplifies modern developments in compact survey platforms. With a length of 2.5 meters, a weight of approximately 140 kg and an operating depth up to 600 meters, the SeaCat combines efficient hydrodynamics with versatile payload options, enabling the collection of high-resolution data of the seafloor and marine

[1] *Naval News: German Navy to equip Frankenthal-class MCM vessels with SeaCat AUV.* URL: https://www.navalnews.com/naval-news/2023/10/german-navy-to-equip-frankenthal-class-mcm-vessels-with-seacat-auv/, accessed at December 2024

environments. It uses an inertial measurement unit that is supported by Doppler velocity log, GPS and depth sensor data [61].

- The Seaglider AUV[2], developed by the University of Washington and now manufactured by Kongsberg Maritime, represents a unique approach to long-duration ocean monitoring. Unlike traditional propeller-driven AUVs, Seaglider uses changes in buoyancy combined with wings to achieve forward motion through the water column. This innovative design enables exceptional endurance, with missions lasting several months and covering thousands of kilometers while consuming minimal power [62]. Seaglider excels in oceanographic data collection, including temperature, salinity, and oxygen measurements [63] up to 6000 meters depth. Its energy-efficient design makes it particularly valuable for long-term environmental monitoring missions, though its relatively slow speed and limited maneuverability restrict its use in more dynamic inspection tasks.

- L3Harris Iver line of AUVs, comprised of several models, represents a serie of compact and versatile platforms. The Iver4-900 model, for example, with a length of approximately 2.5 meters and weighing less than 105 kg, is particularly suited for coastal and shallow water operations. The vehicle operates at depths up to 300 meters with mission durations extending to 20 hours depending on speed and sensor configuration [51]. Its modular design allows for various sensor configurations including side-scan sonar, and water quality sensors, compass, gyroscope and INS [64].

Despite their operational success in data collection missions, these survey-class AUVs face limitations when physical interaction with the environment is required. Their designs prioritize hydrodynamic efficiency and long-duration operations over manipulation capabilities, making them unsuitable for intervention tasks such as grasping objects [65, 66], valve-turning operations on panels [67, 68], force regulation tasks [69, 70] and cooperative manipulation [71].

Multiple robotic vehicles and solutions have been developed for offshore inspection or intervention [72]. The first AUVs capable of performing intervention tasks were developed during projects like ODIN [73] and AMADEUS [74]. The Oceans Systems Laboratory from Heriot-Watt University were also pioneers in this area, considering that the SPINAV project presented a proof-of-concept of AUV inspection, leak detection and mission adaptation [75]. Over the years, several research and commercial solutions have been emerging to allow more diverse and complex intervention tasks (figure 2.2), namely:

- The first significant development was performed by the University of Hawaii in the SAUVIM project [79], which focused on free-floating underwater manipulation. These solutions combined sonars, underwater video cameras, and ultrasonic motion trackers to perform the recovery of an object lying on the seafloor. The SAUVIM vehicle is semi-autonomous, requiring user control for manipulation and/or intervention tasks, but is able to perform path planning and navigation tasks independently of an operator;

[2] *Seaglider - Autonomous Underwater Vehicle.* URL: `https://apl.uw.edu/project/project.php?id=seaglider`, accessed at December 2024

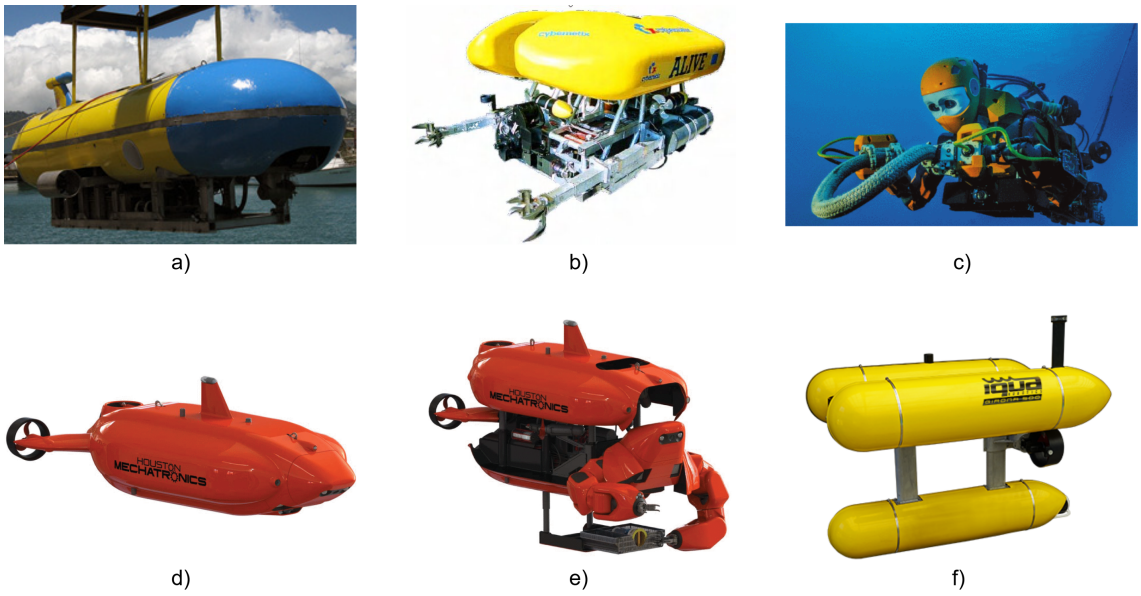

Figure 2.2: Different intervention-capable AUVs available in the state-of-the-art: (a) SAUVIM [76]. (b) ALIVE [77]. (c) OceanOne [78]. (d) Aquanaut in survey mode. (e) Aquanaut in intervention mode[20]. (f) Girona 500[3].

- ALIVE (Autonomous Light Intervention VEhicle) [22], developed under an EU project, was one of the first successful demonstrations of autonomous underwater intervention. The vehicle weighs approximately 3500kg and measures 4m in length, 2.2m in width, and 1.6m in height. The vehicle was equipped with a 7-function (6 DoF) manipulator arm and demonstrated capabilities in autonomous docking and valve-turning operations.

- The Aquanaut [20], which is a hybrid vehicle, that combines the capabilities of both inspection AUVs and intervention ROVs. This vehicle possesses two different configurations, depending on the task being performed (inspection or intervention), being able to change configuration on the fly. The vehicle uses wireless communication to receive simple commands from an operator.

- The Girona 500[3] [80] is an AUV capable of performing different O&M tasks, through the change of its payload, increasing the versatility of the vehicle. The vehicle can be equipped with a manipulator [67] for intervention tasks or a sensor payload for inspections [81, 82]. However, while the system is autonomous, with the user only having to define the mission, changes in the payloads of the vehicle can require small changes in the control system [83]. The overall dimensions of the vehicle are 1.5m in length, 1m in width and 1m in height, with a weight of less than 200 kg.

- OceanOne [78], developed at Stanford University, presents a unique humanoid design approach. The vehicle is human sized and weighs less than 200kg. Its anthropomorphic design includes two arms with haptic feedback capabilities, enabling both autonomous operation

[3] *Girona 500 AUV* URL: `https://iquarobotics.com/girona-500-auv`, accessed at December 2024

and intuitive teleoperation. The vehicle is designed to accomplish operations common to human divers that include the assembly of structures and the delicate handling of samples, artifacts, and other irregularly-shaped objects using navigation with bimanual manipulation and stereovision capabilities.

Recent trends in intervention-capable AUV development show a clear evolution toward more compact and efficient designs while maintaining robust manipulation capabilities. This progression has been driven by the need to balance operational requirements such as stability during intervention tasks with practical considerations like deployment and recovery operations. However, significant challenges remain in achieving the optimal combination of manipulation capability and vehicle maneuverability. To maximize the AUVs ability to perform inspection and intervention tasks, the design should assure movement and operational efficiency. Under this scope, bio mimetic AUVs, with design/propulsion inspired from aquatic animals, can provide more efficient solutions by reducing drag or improving maneuverability. Batoid fishes or Manta rays are motion-efficient with great maneuverability, thus implicating that replicating their geometrical layout and movements in AUVs can bring efficiency benefits [84]. McColgan and McGookin [85] developed a bio-inspired AUV, the RoboSalmon, which can mimic the propulsion and steering of fish to increase movement and maneuverability efficiency when compared to conventional propellers, making them particularly suitable to operate in small spaces with obstacles. Gorma et al. [86] proposed a fish-shaped AUV, the RoboFish, composed of a flexible body that simulates fish propulsion, and is able to efficiently generate sufficient trust, showing improved manoeuvrability compared to conventional shaped AUVs. In the SABUVIS project, the AUV shape designed by Marcin et al. [87] was acquired by producing a 3D scan of a real carp body. The vehicle is propelled forward by the undulation of the tail, along with pectoral fin servomotors for directional control, producing less noise. The Mantabot, proposed by Liu et al. [88] was designed to mimic Manta rays' propulsion movement due to their efficient swimming and high maneuverability.

The evolution of AUV technology demonstrates a clear progression from simple survey vehicles to increasingly sophisticated platforms capable of complex intervention tasks. Survey-class AUVs like HUGIN and REMUS have established reliable solutions for data collection and mapping, while intervention-capable vehicles such as GIRONA 500 and Aquanaut have pushed the boundaries of autonomous manipulation. Bio-inspired designs represent the latest frontier in AUV development, offering potentially revolutionary approaches to underwater locomotion and control. Despite these advances, significant challenges remain in achieving the optimal balance between vehicle capabilities, operational efficiency, and practical deployment considerations.

2.3 Three-dimensional exploration methodologies

Three-dimensional exploration plays a pivotal role in numerous scientific and industrial applications, from infrastructure inspection to environmental monitoring. While methodologies for 3D

exploration in terrestrial and aerial environments are well-established, their adaptation to underwater environments presents unique challenges that demand innovative solutions. This section examines the evolution of 3D exploration methodologies, tracing their development from air-based approaches to underwater applications, highlighting the technological advances and research efforts that address the specific demands of subsea operations.

Traditional methods for inspecting and monitoring diverse types of structures are often expensive, repetitive, time consuming and potentially dangerous for human operators. To overcome this issue, several inspection tasks have been carried out by different vehicles such as Unmanned Aerial Vehicles (UAVs), Autonomous Surface Vehicles (ASVs) and Autonomous Underwater Vehicles for air-based and underwater approaches. Air-based 3D exploration relies typically on technologies such as Light Detection and Ranging (LiDAR) and photogrammetry. These methods are widely used for applications ranging from topographic mapping to infrastructure inspection and autonomous navigation. LiDAR systems employ lasers to measure distances and create high-resolution 3D point clouds of the environment. This technology is particularly effective for airborne surveys, where it combines with GPS and inertial measurement units to achieve precise positioning and mapping. Photogrammetry, on the other hand, uses overlapping images to generate 3D models by triangulating feature points.

Most planning methods for 3D exploration and inspection can be categorized into two categories:

- Model-based methods: rely on prior knowledge of the target structure or environment, utilizing pre-existing Computer-aided design (CAD) models or geometric information to plan and execute inspection tasks. These methods can generate optimal inspection paths and viewpoints when accurate models are available, enabling efficient coverage of known structures;

- Model-free methods: partially eliminate the need for a prior model through autonomous exploration. These approaches are particularly valuable in unknown or dynamic environments where pre-existing models may be unavailable or unreliable. Unfortunately, without the guidance of a prior model, they are limited to conducting local planning to explore unknown regions while simultaneously scanning the known surface.

According to Bicher *et al.* [89], to enable autonomous inspection, robotic systems require sophisticated path planning algorithms capable of generating comprehensive coverage trajectories that simultaneously optimize sensor performance and adhere to kinematic constraints. To accomplish this, the authors proposed a novel fast iterative algorithm for model-based structural inspection. Utilizing a dynamic two-phase optimization strategy, the algorithm systematically identifies and refines viewpoints. The initial phase focuses on minimizing travel expenses between candidate perspectives, followed by a comprehensive path optimization that takes into account vehicle constraints and sensor limitations. Extensive evaluation studies reveal the high–performance the proposed methodology in challenging scenarios (figure 2.3).

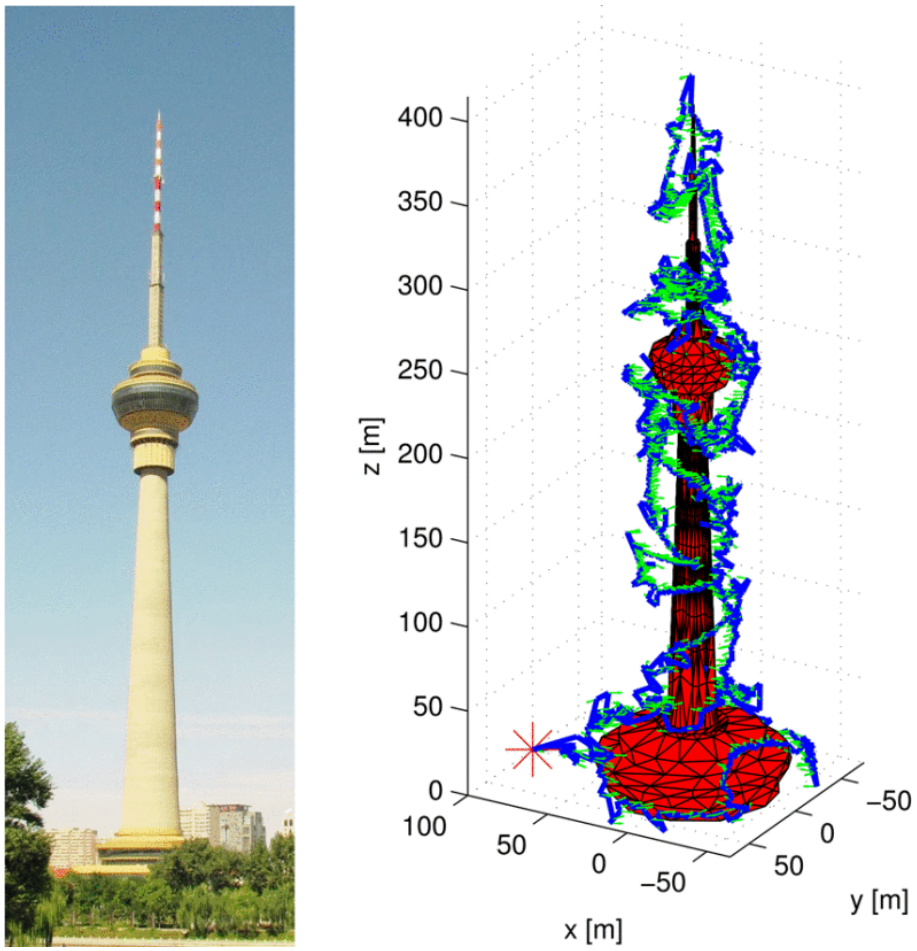

Figure 2.3: Large scale structure inspected using Bicher's approach [89].

Rafael [90], on the other hand, focused on optimizing the energy consumption during an inspection procedure by selecting a path that directly minimizes the energy consumption of the vehicle. As a result, the author proposed a novel Travelling Salesman Problem (TSP) formulation, named ATSP-PL (Asymmetric Travelling Salesman Problem, with Precedence Loss), of which the Precedence Loss designation is related to the objective function, where the loss of moving from a current position to the next one depends on the previous one. Together with an energy model of the vehicle, the developed Energy Efficient Path Planning Algorithm (EEPPA), depicted in figure 2.4, outputs the inspection path as a sequence of viewpoints.

Next-Best-View (NBV) [91] planning represents an iterative approach to environmental exploration where a robot continuously determines optimal viewpoint configurations for 3D reconstruction. This method can be applied in both partially known environments, where some structural information is available, and completely unknown scenarios where the robot must progressively discover its surroundings during the mission. NBV planning addresses two distinct objectives: exploration, which focuses on covering and understanding the 3D volume of space, and inspection, which emphasizes the quality and completeness of surface reconstruction. These different

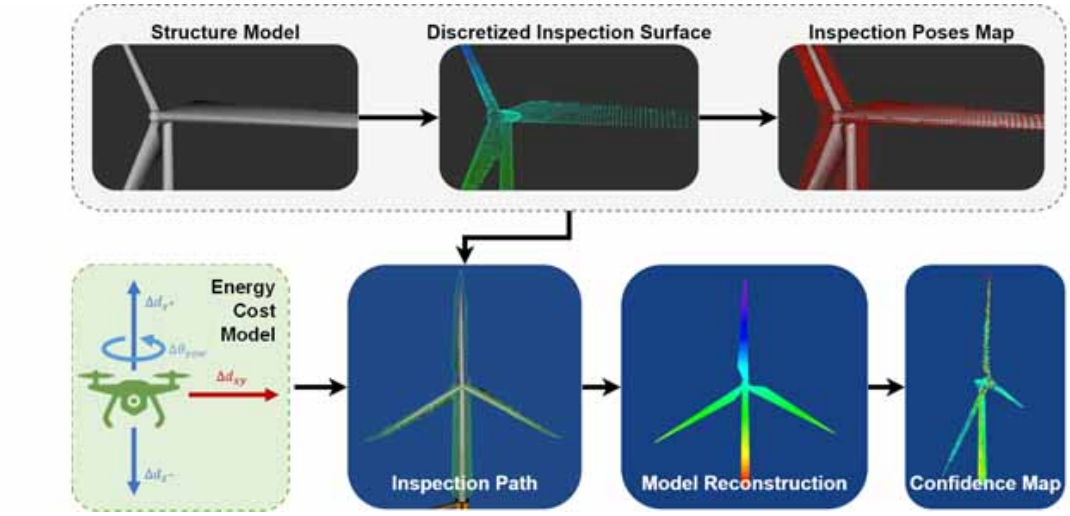

Figure 2.4: Scheme of EEPPA inspection path components, including the mapping of the relevant viewpoints solved using the ATSP-PL, the UAV energy model, the generated inspection path and the correspondent model reconstruction [90].

objectives have led to the development of specialized planning strategies, each optimized for their specific task requirements.

Differently from the classical surface frontier-based approaches [92, 93], Hardouin *et al.* identify the incomplete areas directly from the online map and generate candidate sensor viewpoints in the free space, to complete them. The proposed NBV planning method for single [94] and multiple agents [95], simultaneously explore and inspect large-scale unknown environments by greedily assigning each configuration to the robots, according to the information they locally provide to the fleet. Optimal paths are then computed by solving a variant of the Travelling Salesman Problem (TSP), and updated when unknown areas are completed.

Multiview stereo (MVS) offers another approach to high-quality 3D representations by processing multiple calibrated images captured from different viewpoints. Unlike real-time methods, MVS operates offline, analyzing the complete set of images simultaneously to generate detailed 3D models through feature matching and geometric triangulation. The study presented by Song *et al.* [96] addresses a view-path-planning problem during 3-D scanning of a large-scale structure based on multiview stereo (MVS) for unmanned aerial platforms. The strategy starting from an unknown environment first generates a coarse model from a simple overhead scanning and then plans an inspection path to cover the entire surface of the coarse model. To deal with defective factors of MVS such as occlusions, textureless surfaces, and insufficient parallaxes, the authors propose a novel view-path-planning method for 3-D scanning based on an online MVS reconstruction algorithm. The suggested method incrementally reconstructs the target model online and iteratively plans view paths by analyzing the current partial reconstructions. The presented metodology is capable of constructing a complete 3-D model in a single scanning trial without the need for rescanning.

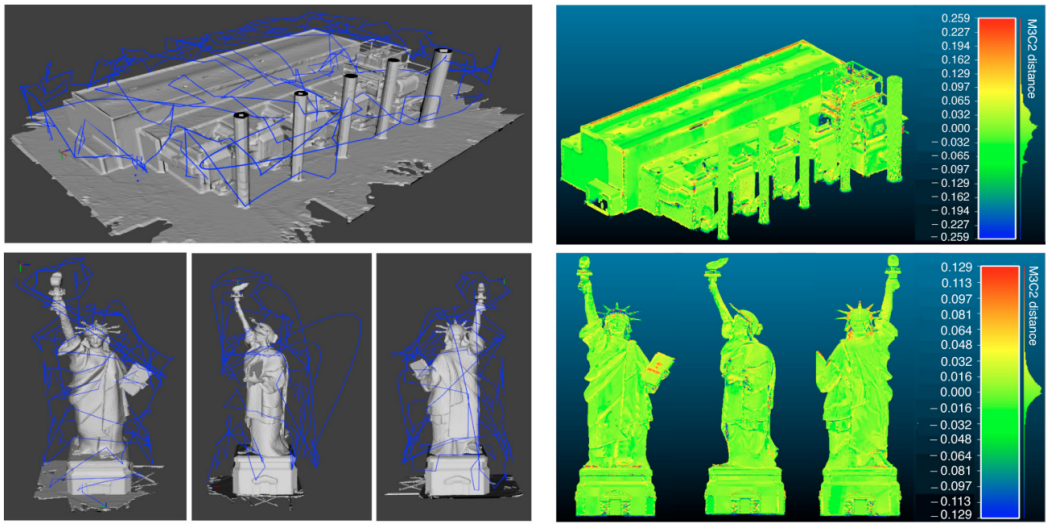

Figure 2.5: Reconstructed mesh and 3D exploration path for two different scenarios using the single agent NBV planning method proposed by Hardouin *et al.* [94].

Other approaches combines the strengths of both model-based and model-free methods. SOAR [97], a LiDAR-Visual heterogeneous multi-UAV planner, presented by Zhang *et al.*, enables simultaneous exploration and photographing for fast autonomous reconstruction of complex scenes. The authors make use of a team of collaborative AUVs allowing for the object to be scanned in par-

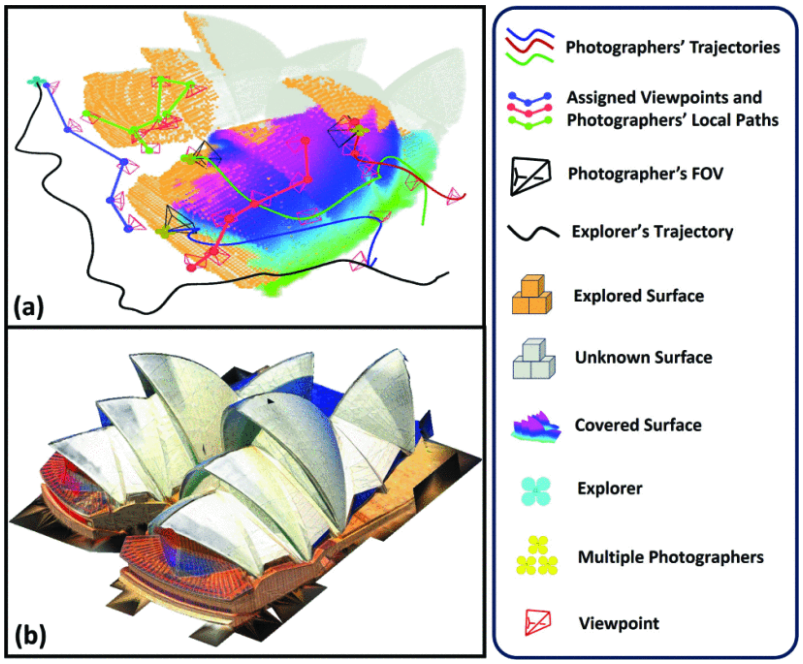

Figure 2.6: SOAR framework's execution process [97].

allel with the coarse model generation. The method categorizes the vehicles into explorers (AUV equipped with a LiDAR sensor) and photographers (equipped with RGB cameras). An explorer provides comprehensive scene information through surface frontier-based exploration, while viewpoints are incrementally generated from uncovered surfaces and assigned to photographers using Consistent Multiple Depot Multiple Traveling Salesman Problem (Consistent-MDMTSP). SOAR was evaluated in complex simulation environments and presented shorter path length and fight time than a model free method and a model-based method from the state-of-the-art, while assuming ideal communication conditions.

Despite the success of air-based methods, these face limitations, particularly pronounced in underwater environments, such as dependency on line-of-sight, sensitivity to environmental conditions, and reliance on GPS for georeferencing. These constraints hinder their direct application in the underwater domain. The ability to create accurate three-dimensional representations of underwater structures is fundamental for autonomous underwater operations. Underwater 3D exploration enables critical capabilities such as environment mapping for navigation, target identification for manipulation tasks, and structural inspection for maintenance operations. However, the underwater environment presents unique challenges for perception systems. One of the most significant challenges of underwater perception lies in the limited quality of information returned by sensors [98]. Light attenuation and scattering affect visual sensors, while acoustic sensors face resolution limitations and noise challenges. These constraints have driven the development of specialized exploration methodologies that can operate effectively despite these limitations. Different sensing modalities and inspection approaches have emerged, each offering distinct advantages and limitations in underwater scenarios.

The applications of underwater 3D exploration span multiple domains in offshore industries. In offshore wind farms, these techniques are essential for monitoring foundation structures, detecting structural deformation, and planning maintenance interventions [99]. The oil and gas sector relies on 3D representations for pipeline inspection, seabed mapping, and subsea infrastructure monitoring [100]. In scientific applications, detailed 3D models enable archaeological preservation, marine habitat mapping, and environmental impact assessment [101]. Particularly crucial is the role of underwater exploration in enabling autonomous intervention tasks. Accurate environmental models are prerequisites for motion planning, collision avoidance, and precise manipulation, especially in complex underwater structures where traditional navigation methods may be insufficient [102, 103, 104].

The choice of sensing modality significantly impacts the quality and applicability of the underwater exploration methods. Each type of sensor offers distinct advantages and faces specific challenges in the underwater environment. Current approaches primarily rely on two sensing modalities: optical sensors and acoustic devices. Visual sensors, including standard cameras and structured light systems, can provide high-resolution data and rich texture information. Recent advances in underwater imaging systems have demonstrated dense and accurate 3D information from harsh underwater environments [105]. However, optical methods face significant limitations in turbid waters where light scattering and absorption severely affect image quality. The effective-

ness of these systems is highly dependent on water clarity and ambient lighting conditions, with their operational range typically limited to a few meters in optimal conditions [106]. On the other hand, sonar systems, particularly multibeam sonars, have become the preferred choice for underwater exploration due to their robustness to water conditions. Unlike optical sensors, acoustic devices can operate effectively in turbid waters and at longer ranges [28]. However, sonar systems present their own set of challenges. Multibeam sonars capture data line by line, requiring precise vehicle motion for comprehensive coverage. Additionally, the resolution of sonar data degrades with distance, creating a fundamental trade-off between coverage range and reconstruction detail [107].

Table 2.2: Comparison of different features of multibeam, forward-looking and profiling sonars.

Feature	**Multibeam Sonar**	**Forward-Looking Sonar**	**Profiling Sonar**
Primary Direction	Downward (seafloor)	Forward	Radial (360° or sector)
Coverage Area	Wide, perpendicular to motion	Narrow cone/fan, ahead of the vehicle	Single line or small sector
Number of Beams	Multiple beams	Single or multiple beams	Single or few rotating beams
Resolution	High spacial resolution for wide-area mapping	High range resolution for close distances	High range resolution for close distances
Range	Long (100–1000 meters)	Short to medium (10–200 meters)	Short to medium (10–300 meters)
Update Rate	Slow	Real-time or near real-time	Slow (rotational or stepwise)
Main Use	Mapping Bathymetry	Navigation Obstacle avoidance	Structural inspection
Limitations	Lower resolution	Limited range	Slow scanning Limited field of view

Sonar systems have become fundamental tools for underwater perception due to their ability to operate effectively in conditions where optical systems fail. Different types of sonar systems offer varying features and capabilities (see table 2.2) for 3D exploration tasks:

- Multibeam sonars represent one of the most widely used systems in the underwater environment. These devices emit multiple acoustic beams in a fan-shaped pattern perpendicular to the vehicle's direction of motion. By combining the returns from each beam, they create a bathymetric profile of the seabed or structure being surveyed [108]. Modern multibeam systems can generate hundreds of beams per ping, though their data acquisition remains inherently sequential, capturing one line at a time. This characteristic necessitates precise vehicle motion control to achieve complete coverage of the target structure;

- Forward-looking sonars (FLS) provide a different approach to underwater sensing. Unlike multibeam systems, FLS devices emit a small number of acoustic beams in a forward-facing pattern, typically covering a wider horizontal angle but smaller vertical aperture. These systems are particularly valuable for obstacle detection and navigation [109] but can also contribute to 3D reconstruction through multi-view integration. Their ability to provide real-time imagery of the environment ahead of the vehicle makes them especially useful for close-range operations [110];

- Profiling sonars, also known as scanning sonars, operate by mechanically rotating a narrow acoustic beam to build up a detailed profile of underwater structures. These systems can achieve higher resolution than traditional multibeam sonars but require longer acquisition times due to their mechanical scanning nature. They are particularly effective for detailed inspection of underwater structures where precise dimensional measurements are required [111].

Underwater exploration strategies must address the unique challenges of the marine environment while ensuring efficient and reliable data collection. As explained previously, traditional exploration approaches developed for aerial or terrestrial applications require significant adaptation for underwater use due to the fundamental differences in sensing capabilities, environmental conditions, and operational constraints. Complementary to model-based and model-free categories, current underwater exploration strategies can be classified according to their approach to environment coverage and data acquisition.

Coverage-based strategies

Coverage-based strategies focus on ensuring complete spatial exploration of the target area or structure. These methods typically implement systematic scanning patterns, such as lawnmower trajectories or spiral paths, to methodically cover the inspection space [112]. The lawnmower pattern consists of parallel tracklines with specified overlap between adjacent passes. This overlap is determined by sensor characteristics and desired data density. On the other hand, spiral patterns are particularly suited for circular structures or radial exploration, beginning either from the periphery or the center of the area of interest.

These strategies offer several distinct advantages. Their systematic nature ensures complete coverage of the target area when executed under ideal conditions [113], making them particularly reliable for standardized inspection tasks. Additionally, the predetermined paths simplify mission planning and execution, reducing computational requirements during operation and makes it easier to estimate mission duration and energy requirements, facilitating operational planning. However, coverage-based strategies also present significant limitations in underwater applications. Their rigid nature makes them poorly suited to adapting to unexpected obstacles or changing environmental conditions (e.g. the lawnmower problem does not account for obstacles) [112]. The predefined patterns may not optimize data collection quality, particularly in underwater environments where sonar data quality varies significantly with acquisition angle and distance [114]. These approaches often result in redundant coverage of areas that may not require detailed inspection, potentially misestimating the exploration cost of certain areas, leading to inefficient use of mission time and energy resources [115].

Coverage-based strategies remain valuable for specific applications where systematic coverage is prioritized over adaptive behavior. Early developments in this field demonstrated fundamental approaches. Galceran and Carreras [116] introduced a Coverage Path Planning (CPP) method based on Morse decomposition to minimize redundant coverage for underwater vehicles imaging

the ocean floor. Their method determined sweep directions for each cell and adjusted boustrophedon path spacing based on ocean depth, demonstrating effectiveness through simulations with real-world data. The boustrophedon decomposition is similar to the trapezoidal decomposition but it only considers vertices where a vertical segment can be extended both above and below the vertex. The vertices where this occurs are called critical points. Similarly, Paull et al. [117, 118] developed an online coverage method specifically for vehicles equipped with side-looking sensors, targeting mine countermeasure operations. Their approach used multiobjective optimization with hexagonal grid decomposition to maximize information gain from sensor measurements. While effective for non-convex areas, the method didn't address obstacle avoidance.

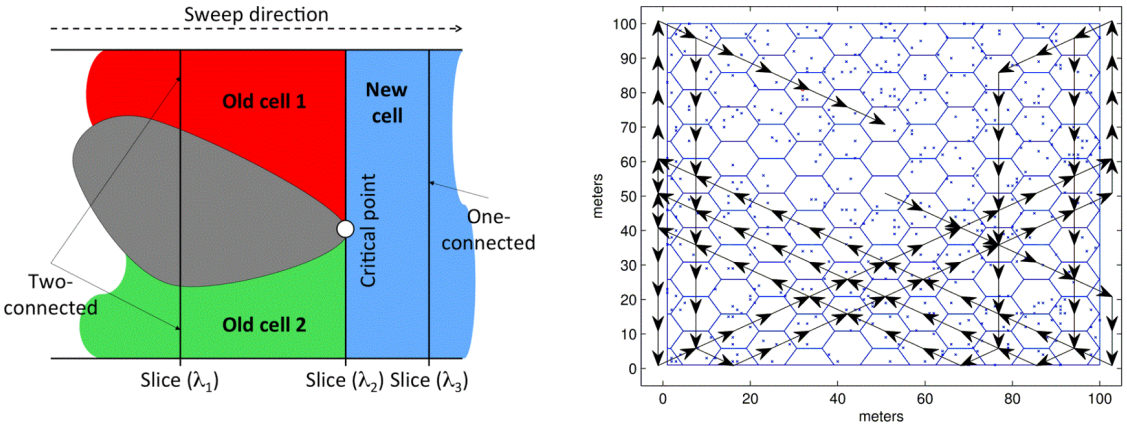

Figure 2.7: Two different examples of cell determination. Left figure - Morse-based boustrophedon cell decomposition [116]. Right figure - regular exact hexagonal cell decomposition [117].

More recent implementations have advanced these concepts with sophisticated approaches. Palomeras et al. [119] developed a View Planning (VP) algorithm that optimizes underwater exploration by minimizing the number of viewpoints while maximizing information gain. When no prior map exists, the system begins by gathering preliminary bathymetric data to create an octree representation of the environment. This octree structure, where each internal node has eight children, efficiently represents the three-dimensional space. Using this initial model, the algorithm employs an offline view-planner to compute the minimum set of sensor configurations required to cover the volume of interest, while considering both the mapping sensor's characteristics and vehicle safety constraints. The final exploration path is generated by solving the traveling salesman problem across the selected viewpoints, with the RRT* (Rapidly exploring Random Tree Star) algorithm determining collision-free trajectories between positions.

Adaptive exploration strategies

Adaptive exploration strategies represent a more sophisticated approach, modifying the exploration path based on real-time sensor feedback and environmental conditions. These methods continuously evaluate the quality of collected data and adjust the vehicle's trajectory to optimize sensing conditions, similarly to previously shown aerial methods that use MVS or approaches like

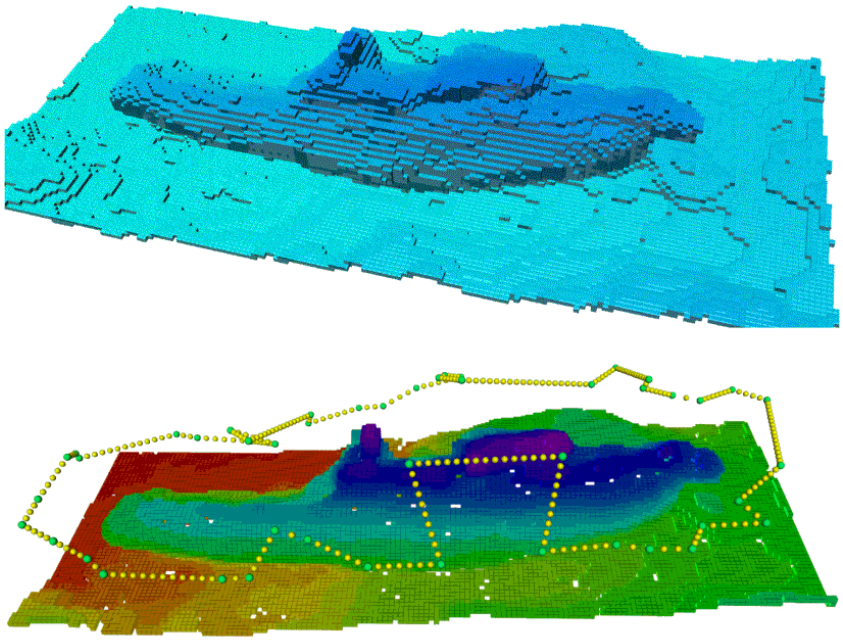

Figure 2.8: Octree model generated from a multibeam survey over a shipwreck, using Girona 500 AUV, and the resulting plan computed by the view-planner [119].

SOAR. For instance, some approaches implement information gain techniques to identify areas requiring additional inspection or different viewing angles. Adaptive exploration strategies offer several distinct advantages for underwater operations. The primary benefit lies in their ability to dynamically adjust to environmental conditions and data quality requirements in real-time. This adaptability enables improved data collection by modifying vehicle trajectories based on sensor feedback, particularly valuable in scenarios where environmental conditions can change rapidly. Additionally, these strategies often achieve more efficient coverage by prioritizing areas of interest or regions requiring additional inspection. However, these strategies also present significant limitations and implementation challenges. The computational complexity of real-time path adaptation can strain onboard processing resources, particularly when handling multiple data streams and environmental variables simultaneously. The requirement for continuous sensor processing and trajectory replanning can impact system response time, potentially affecting the vehicle's ability to react to rapid environmental changes. Furthermore, the effectiveness of adaptive strategies heavily depends on the quality and reliability of sensor feedback, which can be compromised in challenging underwater conditions such as turbid waters or strong currents. Amigoni *et al.* [120] analyzed the relationship between exploration efficiency and two key factors: the frequency of decision-making processes and the rate at which new measurements are integrated into environmental maps. This study show that although increasing perception and decision frequencies generally increases performance, when these frequencies become too high, performance starts to degrade due to increased computational effort.

Several research efforts have developed adaptive exploration strategies for autonomous underwater inspection. Vidal's [111] approach proposes an online algorithm for iterative structure mapping without requiring prior environmental knowledge. This method operates within user-defined parameters including a safe exploration depth and a bounded exploration area. The algorithm executes a three-step process: first, it incorporates profiling sonar data into a 2D grid map, where voxels are classified into different states (empty, unseen, occluded, occplane, occupied, or viewed); second, it generates potential viewpoints based on the current map state; and finally, it plans a safe path to guide the vehicle to the selected viewpoint. Two different kind of viewpoints are generate. Range viewpoints are designed to move the robot toward locations where sonar data could reveal new information about the scene and camera viewpoints are generated so that new optical information about the scene can be obtained by the camera. Both viewpoints are generated at a configurable distance from occplane voxels, along the perpendicular of the surface, but while range viewpoints consider occplane voxels adjacent to occupied voxels, camera viewpoints are generated by firstly detecting occupied voxels adjacent to viewed voxels. The best viewpoint is considered to be the closest one according to the euclidean distance. Figure 2.9 show an example of world representation, map generation and viewpoint generation using Vidal's approach. In the presented situation, the camera viewpoint was selected (solid orange arrow), while the range viewpoint was discarded (light red arrow).

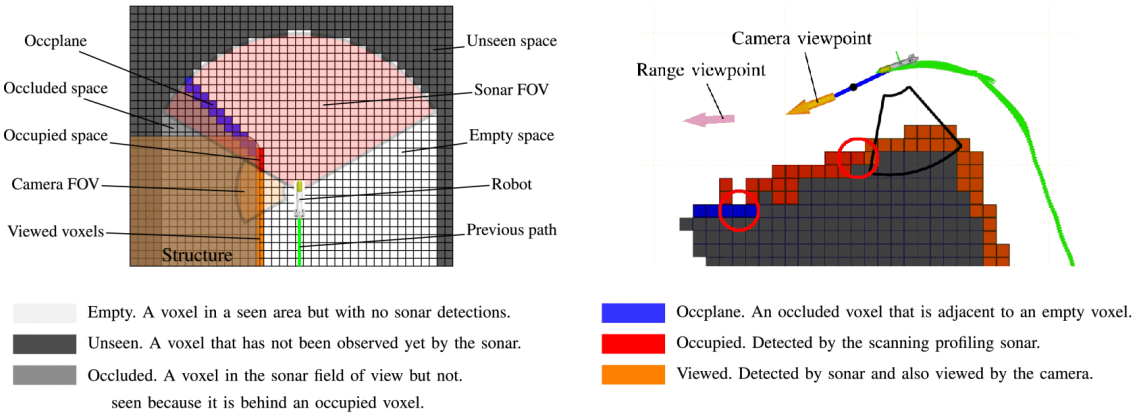

Figure 2.9: Synthetic example of world representation, map generation and viewpoint generation using Vidal's approach [111].

Recently, Vidal et al. [121] expanded their previous approach with new features, such as the ability to autonomously explore the environment even when it is completely empty or when the robot is initially far from any obstacle in the environment. Their new proposal combines view planning (VP) algorithm with frontier-based (FB) methods introducing a strategy to map empty space, removing the restriction of having to start the exploration in front of occupied space. The set of different cell labels was changed from 6 to eight labels, so that they represent the most important data related to the exploration problem.

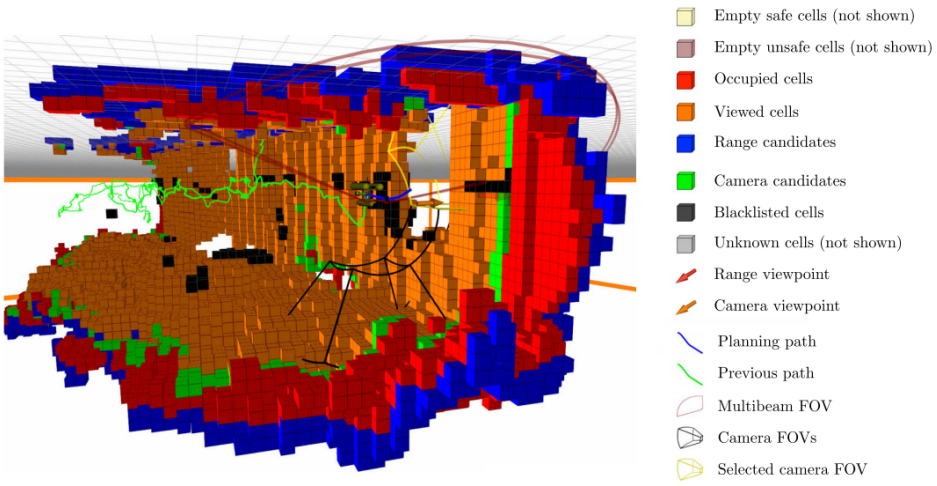

Figure 2.10: Girona 500 AUV performing an exploration of the breakwater structure and the different cell labels used from Vidal's underwater exploration method [121].

Building on similar principles, another method introduces a probabilistic next-best-view planner specifically designed for hover-capable AUVs operating in unknown environments [122]. This approach implements an iterative scanning strategy where the vehicle explores the environment from multiple viewpoints. The proposed methodology requires the definition of a set of input

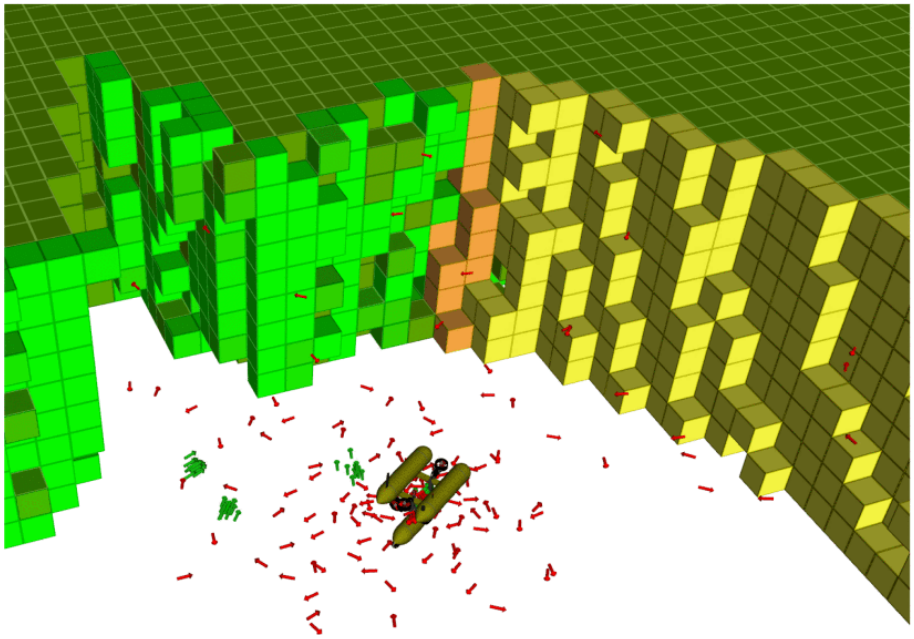

Figure 2.11: Example of the samples generated around the vehicle during an iteration of the probabilist NBV planning algorithm. Candidate samples are shown as red arrows, probabilistic samples are shown as green arrows, green voxels represent unknown areas and light green voxels represent occupied areas [122].

parameters, including the exploration area limits, the AUV safety limits, the position of an initial viewpoint, the parameters of the scanning sensor, and the parameters for the NBV planning algorithm. During the acquisition of a scan the vehicle keeps its position, as static as possible, and the sensor is moved using a high accuracy pan and tilt positioner. The system selects optimal viewpoints from randomly sampled candidates using a utility function evaluation that takes into account visibility and distance to be traveled until reaching the viewpoint (see figure 2.11). After selection, the planner generates collision-free trajectories to these locations using the rapidly-exploring random tree star (RRT*) algorithm, allowing the AUV to navigate safely and acquire new sensor data, which is then registered and integrated with previous scans to build a comprehensive environmental model.

Hurtós [123] demonstrated another application of adaptive methods through the development of a robust framework for underwater chain detection, following, and mapping. Their work presents two chain link detectors (one for horizontal and one for vertical chains), utilizing data from both forward-looking sonar and multibeam sensors. The methodology follows a systematic approach: first, the vehicle executes a predefined lawnmower survey pattern over the target area to collect initial data (see figure 2.12). During this phase, the detection module processes acoustic images using local pattern-matching techniques to identify chain links, taking advantage of

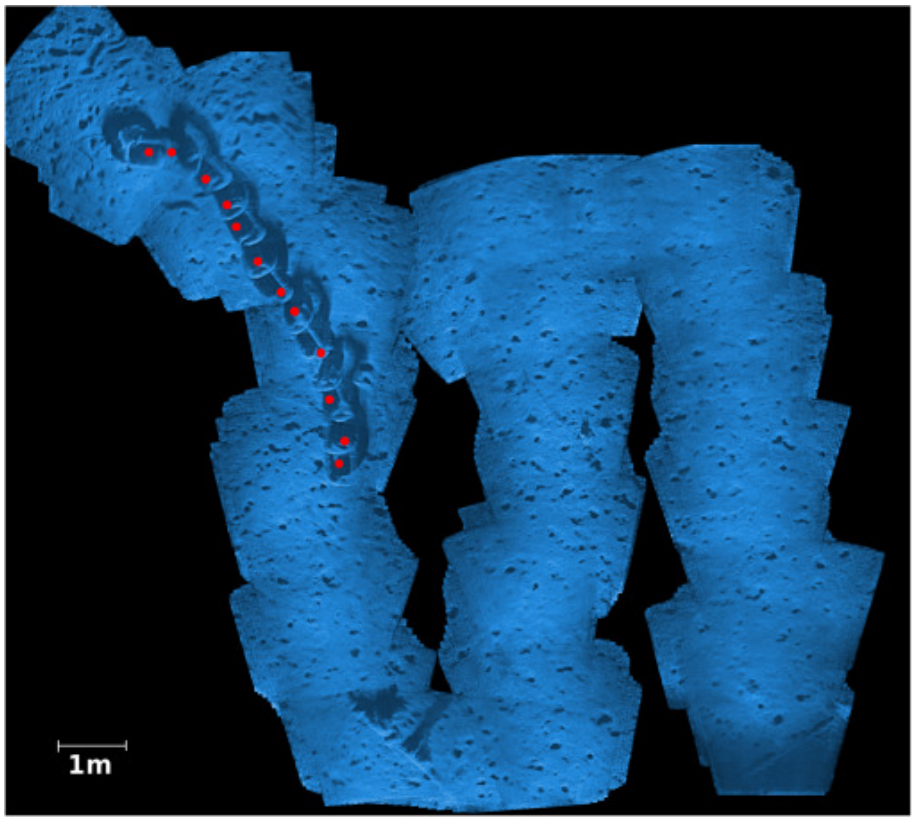

Figure 2.12: Acoustic mosaic generated by registering the sonar frames along the vehicle trajectory with the link waypoints overlaid in red [123].

the sonar's high frame rate. Once links are detected, the system employs a k-means clustering algorithm to associate multiple detections with corresponding waypoints, effectively constructing a trajectory along the chain. The exploration continues with a specialized high-level controller guiding the vehicle through these waypoints, simultaneously following the chain while maintaining awareness of upcoming links.

2.4 Motion planning strategies for manipulation

Underwater manipulators have become essential tools in offshore industries, enabling complex intervention tasks that would be dangerous or impossible for human divers. The majority of existing underwater manipulators used on underwater vehicles are anthropomorphic, designed to resemble a human arm. These manipulators are composed of a sequence of rigid bodies (links) interconnected by means of revolute joints with a suitable angular displacement between them, and grippers or other interchangeable tools attached at the end-effector [124].

Underwater manipulators are designed to perform a diverse range of intervention tasks in marine environments: in the offshore energy sector, these systems routinely conduct pipe inspection, valve operations, and surface cleaning operations [125, 126, 127]; maritime operations benefit from their capabilities in salvage operations, mine disposal, and clearing underwater debris including abandoned fishing nets [128, 129, 130]; the scientific community employs these manipulators for precise tasks such as geological sampling, biological specimen collection, and archaeological preservation work [131, 132].

Underwater manipulators are mounted on vehicles in different configurations, each designed to optimize specific operational requirements and mission objectives. The most common configuration places the manipulator at the front of the vehicle [124], providing maximum visibility for operators and optimal workspace accessibility. However, alternative mounting configurations have emerged to address specific operational challenges. Bottom-mounted manipulators, as demonstrated in vehicles like the GIRONA 500 and SAUVIM, offer distinct advantages in certain scenarios. This configuration provides better stability during manipulation tasks as the manipulator increase the vertical separation between the vehicle's center of buoyancy and center of mass [83]. Additionally, bottom mounting can protect the manipulator during transit and allow for more streamlined vehicle designs when the manipulator is not in use. Some advanced systems employ dual-arm configurations, particularly relevant for complex manipulation tasks requiring coordinated tool use or object handling. The DexROV project exemplifies this approach, with two manipulators mounted side by side at the front of the vehicle, enabling more sophisticated intervention capabilities [133]. This configuration, while more complex to control, provides enhanced dexterity and redundancy in manipulation tasks. Recent developments have explored reconfigurable mounting systems that allow the manipulator to be repositioned based on mission requirements. The Aquanaut vehicle represents this new direction, featuring a design that can reconfigure from a hydrodynamically efficient survey mode to an intervention mode with dual manipulators [20]. This adaptability is particularly valuable since it addresses the traditional trade-off between

hydrodynamic efficiency during transit and effective manipulation capability during intervention tasks.

Motion planning for underwater manipulation presents unique challenges that go beyond traditional robotic applications. The underwater environment introduces complex hydrodynamic effects, varying currents, and coupled dynamics between the vehicle and manipulator that must be considered when generating feasible trajectories. Additionally, the limited accuracy of underwater perception systems and the inherent uncertainty in vehicle positioning add layers of complexity to the planning problem [134]. Some works try to identify high performing planners available in the Open Motion Planning Library (OMPL) used by MoveIt![4] [135] when carrying out grasp executions [136], however these works only study the performance of these planners above water and through comparisons between singular indicators. The most used metrics currently in the state-of-the-art to describe the planners are: solved runs, computing time and path length. Take solved runs as the percentage of total runs of the planner resulting in feasible paths. In this case, higher values of solved runs means higher performance. Total computing time is the time it takes for planners to produce feasible or optimized paths with path simplification, and shorter times are considered as higher performances. Finally, path length is measured by the length of the sum of motions for a produced path and shorter lengths are considered as higher performance. These metrics are analyzed individually with conclusions directly related to performance. None of the metrics presented take into account the safety of the manipulator during the execution of the trajectory, nor the quality of the trajectory executed by a real manipulator when compared to the planned one. These limitations result in conclusions that are often inappropriate for highly complex environments, such as the underwater environment.

Sampling-based motion planners build a representation of the configuration space through random sampling, without requiring complete knowledge of the environment. These can be probabilistic complete [137], which means that the probability that the planner will return a solution (if one exists) approaches one as the number of samples tends to infinity. OMPL includes non-optimizing and optimizing planners. When compared with non-optimizing ones is expected that the last ones will produce shorter path lengths but with higher computational efforts and computational time. These planners can also have a time-invariant goal which means that they stop computing as soon as a path is found that satisfies the optimization objective. Additionally, planners can also be classified into multi-query planners, which are planners that build a roadmap of the entire environment that can be used for multiple queries. Table 2.3 shows the most common OMPL planners.

One of the most common sampling-based motion planner is the Probabilistic RoadMap (PRM) [137]. PRM is a planner that constructs a roadmap of valid states in the state space that approximate the connectivity of the state space. Near-by states are connected by valid motions. These way, finding a motion plan that connects two given states is reduced to a discrete search in the roadmap. OMPL contains a number of variants of PRM. LazyPRM [148] is a planner that constructs a roadmap just like PRM does, but that uses lazy collision checking. PRMstar [146] au-

[4]Ioan A. Sucan and Sachin Chitta, "MoveIt", [Online] Available at moveit.ros.org.

Table 2.3: Most common OMPL planners and their classification into time-invariant goal, optimizing planners and multi-query planners.

Planner id	Time-invariant goal	Optimizing planners	Multi-query
BiEST [138]	✓		
EST [138]	✓		
ProjEST [138]	✓		
TRRT [139]	✓	✓	
BiTRRT [139]	✓	✓	
RRT [140]	✓		
SBL [141]	✓		
BKPIECE [142]	✓		
PDST [143]	✓		
RRTConnect [144]	✓		
STRIDE [145]	✓		
RRTstar [146]		✓	
PRM [137]			✓
PRMstar [146]		✓	✓
LBTRRT [147]	✓	✓	
LazyPRM [148]			✓
LazyPRMstar [149]		✓	✓
SPARS [150]		✓	✓
KPIECE [142]	✓		
SPARStwo [151]		✓	✓
FMT [152]	✓	✓	
LBKPIECE [142]	✓		

tomatically computes the number of neighbors based on the coverage of the space, guaranteeing optimality of solutions. LazyPRMstar [149] builds a roadmap of feasible configurations but edges are not immediately checked for collision. If a better candidate path is found, then all edges along that path are checked for collision.

SPArse Roadmap Spanner technique (SPARS) [150] is an asymptotic near-optimality planner. Asymptotic optimality (AO) implies that as more time is invested in constructing the roadmap, the quality of solutions improves and converges to optimal at infinity. SPARS relaxes the optimality guarantees by utilizing graph spanners, thus becoming Asymptotic Near-Optimality. SPARStwo [151] is a variant of the SPARS algorithm which removes the dependency on having the dense graph and uses a different approach to identifying interfaces and computing shortest paths through said interfaces.

Another common sampling-based motion planner is the Rapidly-exploring Random Tree (RRT) method [140]. RRT is a randomized data structure that is iteratively expanded by applying control inputs that drive the system slightly toward randomly-selected points. One of its advantages is that it an be directly applied to nonholonomic and kinodynamic planning. The RRTConnect method is a bidirectional version of RRT (i.e., it grows two trees) and it usually outperforms the original RRT algorithm [144]. This planner has already been used to perform free-floating manipulation

with an AUV and the results demonstrate its potential to deal with advanced underwater manipulation tasks [153]. Another variants are the RRTstar [146], Lower Bound Tree RRT (LBTRRT) [147], Transition-based RRT (TRRT) and Bi-directional TRRT (BiTRRT) [139]. RRTstar is an asymptotically-optimal incremental sampling-based motion planning algorithm. This algorithm checks whether the new sampled node can be connected to other near nodes, similar to PRMstar. LBTRRT uses an extra lower bound tree. The combination of the two trees, is faster to maintain than the tree maintained by RRTstar. TRRT takes into consideration state costs and uses transition tests from stochastic optimization methods to accept or reject new potential states.

The Expansive-Spaces Trees (EST) method [138] stands for Expansive Space Trees. It is a tree-based motion planner that measures the density of the explored space, biasing exploration toward parts of the space with lowest density. Bi-directional EST (BiEST) [138] grows two trees, similar to RRTConnect. Projection EST (ProjEST) [138] uses a grid imposed on a projection of the state space to detect the less explored area of the space. The variant that grows two trees, which expands in the same manner as EST and uses lazy collision-checking, is called Single-Query Bi-Directional Probabilistic Roadmap Planner with Lazy Collision Checking (SBL) [141].

Other sampling-based motion planner strategies like STRIDE (Search Tree with Resolution Independent Density Estimation) and PDST (Path-Directed Subdivision Tree) try to detect the less explored area of the space [145, 143], like EST. But while STRIDE uses a Geometric Nearneighbor Access Tree (GNAT) to estimate the density of the configuration space, PDST makes use of a binary space partition of a projection of the state space. KPIECE (Kinodynamic motion Planning by Interior Exterior Cell Exploration) [142] is a tree-based planner that uses discretization to guide the exploration of the state space. Its bi-directional variant is called BKPIECE and the variant which incorporates lazy collision checking is the LBKPIECE. Finally, Fast Marching Tree (FMT) [152] performs a lazy dynamic programming recursion on a set of probabilistically-drawn samples to grow a tree of paths, which moves steadily outward in cost-to-come space.

Current state-of-the-art underwater manipulation systems are predominantly designed to operate with prior knowledge of target objects and their positions. This reliance on pre-existing object information limits their ability to adapt to unfamiliar scenarios or handle novel objects autonomously. Furthermore, the lack of publicly available underwater manipulation datasets hinders the development of more advanced manipulation strategies and limits the ability to benchmark and compare different approaches [154]. Additionally, while significant advances have been made in motion planning for general robotics applications, underwater manipulation systems often diverge from using these state-of-the-art planners. Instead, the field has largely developed application-specific solutions tailored to the unique challenges of the underwater environment. This trend reflects the distinctive requirements of underwater operations, where factors such as hydrodynamic effects, vehicle-manipulator coupling, and environmental uncertainties necessitate specialized approaches. For instance, for the GIRONA 500 AUV, authors started by developing a specialized planner for valve turning operations that considers both vehicle stability and manipulator constraints, rather than adapting existing general-purpose planners [155]. Their approach divided the control problem into two tasks: the docking maneuver followed by constant forward thrust to

maintaining vehicle position, and a basic grasp planning methodology for valve and connector manipulation as shown in figure 2.13.

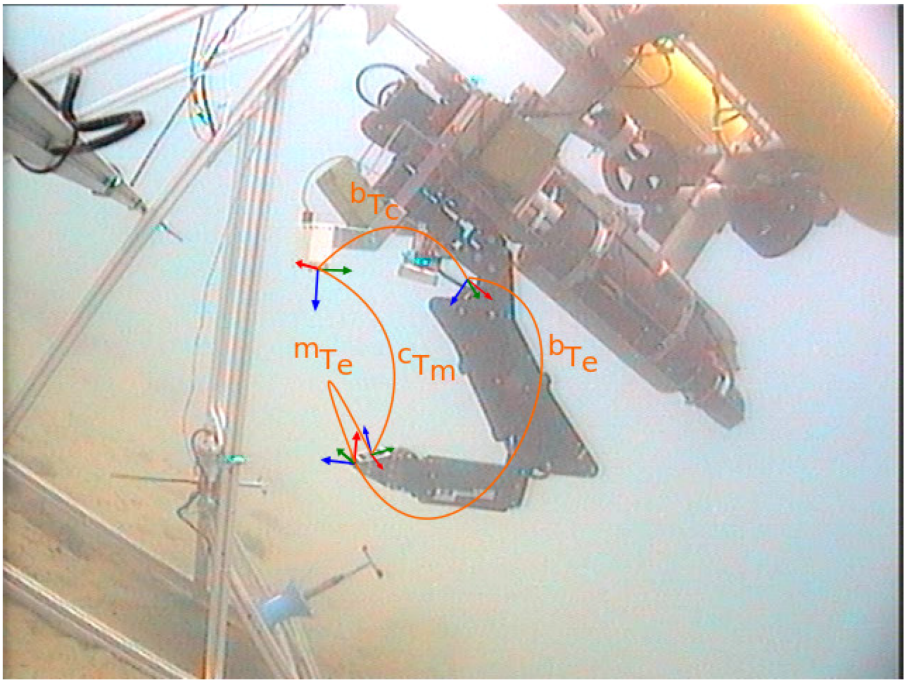

Figure 2.13: Girona 500 AUV performing a fixed-base manipulation [155].

This hierarchical structure ensures stable vehicle positioning during manipulation, a crucial requirement not typically addressed in general-purpose planners. The grasp planning methodology implements a waypoint-based approach for generating end-effector trajectories. For valve manipulation tasks, the system defines three key waypoints: a pre-manipulation position for safe approach, a manipulation position for the actual interaction, and a post-manipulation position for safe retreat. Similarly, for connector operations, the system establishes multiple waypoints including approach positions, manipulation positions, and specific waypoints for unplugging and plugging actions. This structured approach ensures collision-free trajectories around the known panel geometry while maintaining appropriate end-effector orientations throughout the manipulation sequence. The proposed system generates joint motions by computing the required joint velocities based on the Cartesian distance between the end-effector's current position and the target waypoint. This computation is achieved by multiplying the Cartesian distance by the pseudo-inverse of the manipulator's Jacobian matrix evaluated at the end-effector position, effectively transforming the desired Cartesian motion into corresponding joint velocities that guide the end-effector toward the waypoint. The system's robustness was evaluated through multiple valve turning and connector manipulation trials. Performance testing was conducted in both controlled and real environments. The system achieved approximately 80% success rate in water tank trials, which decreased to 60% in sea trials. This performance reduction was primarily attributed to vision system limitations, particularly false detections caused by variable illumination conditions in the

marine environment.

Later, the Girona 500 AUV was used to achieve free floating autonomous underwater manipulation [156]. Authors proposed a control architecture (figure 2.14) for the whole system, with particular attention on a suitable grasp planning strategy. The grasp planning strategy was designed to ensure effective and precise grasping while the AUV remains in motion.

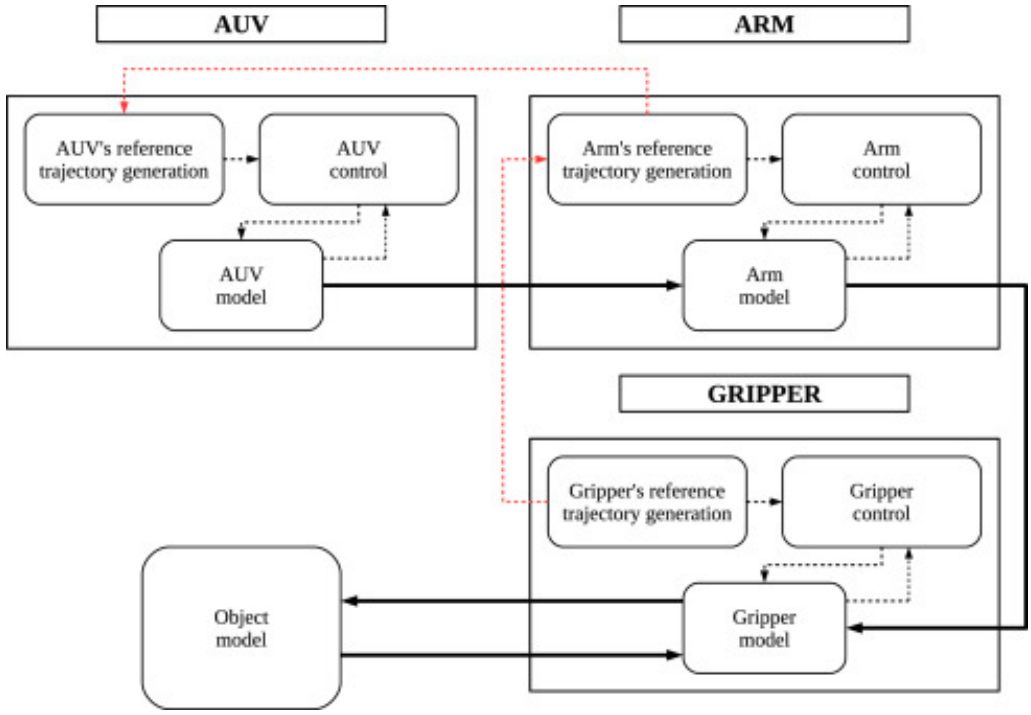

Figure 2.14: Girona 500 AUV control architecture [156].

The grasp planning strategy begins with identifying suitable contact points on the object's surface. These contact points are selected to optimize several grasp quality criteria. Among these criteria are the shape of the grasp polygon formed by the contact points, with the goal of achieving a configuration as close to a regular polygon as possible. The algorithm operates by iteratively adjusting initial candidate contact points through the application of virtual forces. These forces are calculated based on the desired grasp quality improvements, such as enlarging the grasp polygon, achieving an equilateral configuration, and aligning the grasp with the object's inherent symmetries. These adjustments continue until the points converge to a configuration that meets the defined thresholds for grasp quality. The control system employs a decoupled strategy, where the dynamics of the AUV and the manipulator arm are treated separately. This approach simplifies the control architecture and ensures robustness by treating the interaction between the vehicle and the arm as external disturbances. Further decoupling is achieved by separating the motion control of the gripper from that of the arm, allowing the two components to function independently yet cohesively. The effectiveness of the proposed strategy was validated through simulations, which tested its performance under various conditions, including different AUV speeds and dynamic

environmental interactions.

The TRIDENT project took a different approach, implementing a custom multi-layer control architecture, as depicted in figure 2.15, specifically designed for floating manipulation, incorporating vehicle-arm coordination strategies not typically found in standard planning frameworks [65]. The authors presented a task priority based control and coordination framework that integrates dynamic control of both the vehicle and manipulator, with a focus on system safety and/or its good operational conditions.

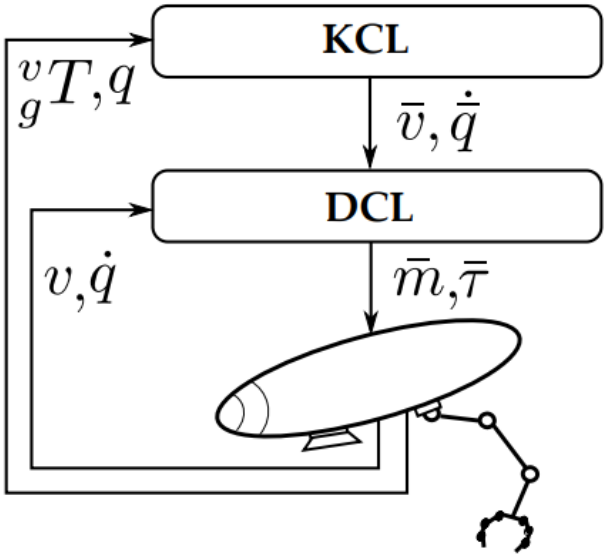

Figure 2.15: TRIDENT's two layered architecture [65].

The high-level control layer, the Kinematic Control Layer (KCL), handles the task specifications and generates Cartesian references for both the vehicle and manipulator end-effector, while the low-level layer, the Dynamic Control Layer (DCL), is responsible for real-time tracking of the velocity vector generated by the previous layer. TRIDENT's control architecture introduced several innovations to the task-priority framework. The approach incorporated scalar inequality constraints through activation functions and algorithmic regularization, enhancing the system's ability to handle multiple constraints simultaneously. Furthermore, they implemented a Dynamic Programming (DP) technique between the vehicle and manipulator control loops, enabling optimal arm control regardless of vehicle velocity. This decoupling proved particularly advantageous as it allowed the vehicle and manipulator controllers to operate at different rates, improving the system's overall robustness to disturbances. In both simulation and sea trials the system was able to satisfy all the safety constraints, such as joint limits, and recovering the black box from the bottom of the pool.

The Ocean One humanoid robot introduced yet another specialized approach, utilizing a custom constraint-based task framework [157]. Their system handles multiple constraints simultane-

ously, including joint limits, self-collision avoidance, and obstacle avoidance, while specifically accounting for the underwater environment's effects on manipulation tasks.

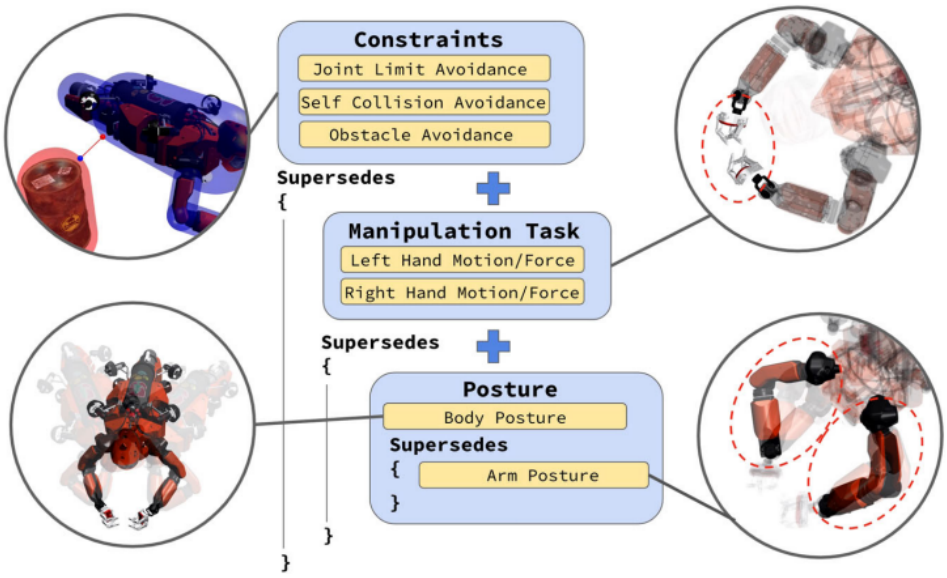

Figure 2.16: Ocean One hierarchical task priority system [157].

The framework incorporates hydrodynamic models and implements specialized force control strategies essential for underwater manipulation. The proposed hierarchical task priority system (shown in figure 2.16) is organized with three distinct tasks: Constraint Task (Highest Priority), Manipulation Task (Medium Priority) and Posture Task (Lowest Priority). The highest priority is given to the constraint task, which acts as a critical safety mechanism. This task continuously monitors potential risks such as self-collision, joint movement limits, and potential collisions with environmental obstacles. Should any constraint approach violation, this task immediately intervenes, effectively filtering out any actions from other tasks that might compromise the robot's safety. The manipulation task operates at a medium priority, focusing on controlling the robot's two hands. It leverages the entire robot's body actuations and kinematics to enable precise hand movements and interactions. At the lowest priority is the posture task, which optimizes the robot's body positioning relative to its hands. This task takes advantage of the redundancy in the robot's arms to fine-tune the hands' inertial properties, ensuring the most effective positioning for the manipulation task at hand. The most innovative aspect of this control system is its design philosophy. With a minimal set of control inputs directed specifically to the hands, the entire robot can be piloted. So, instead of using a complex motion planning algorithm that would precompute trajectories, the control architecture achieves robot navigation and manipulation through a hierarchical system that uses human interfaces to enable interaction while avoiding micromanagement.

2.5 Critical Review

AUVs already play an important role in several operations and maintenance activities. Nevertheless, many of these technologies have limited autonomy and range of exploration, and the ability to carry out autonomous intervention operations is still very limited. As shown in the comparison of different AUV characteristics in the state-of-the-art, in table 2.4, designs are usually based on torpedo shaped platforms, which provide improved hydrodynamic efficiency and long endurance, coupled to long range and depth capacity. However, traditional torpedo-shaped AUVs are mostly underactuated systems with strong nonlinearity and coupling in their control systems, making precise positioning and intervention tasks particularly challenging [158]. Open-frame structures are also commonly found in research, which are usually implemented in AUVs with low-speed operation, since drag force is quadratically proportional to the vehicle's velocity, and open-frame structures are not very hydrodynamic-efficient. This approach is, however, easier to access and maintain, as well as implement modularity.

Table 2.4: Resume of different AUV characteristics of the state-of-the-art.

AUV	Type	Shape	Max Depth (m)	Weight (kg)	Length (m)	Sensors	Key Features
HUGIN	Survey	Torpedo	6000	2200	6.6	Multibeam echosounder, sub-bottom profiler, cameras, volume search sonar, INS, DVL, GPS	Advanced sensor suite, INS/DVL/GPS navigation
REMUS 100	Survey	Torpedo	100	40	2.1	DeltaT MBES, sidescan sonar, GPS, IMU, DVL, depth sensor	Compact size, lightweight and modular payload options
Bluefin-21	Survey	Torpedo	5000	750	4.93	Mission configurable sensors	Modular design, mission-specific configuration
SeaCat	Survey	Torpedo	600	140	2.5	IMU, DVL, GPS, depth sensor	Compact platform, IMU/DVL/GPS navigation
Seaglider	Survey	Glider	6000	50	1.8	Temperature, salinity, oxygen sensors	Buoyancy-driven, exceptional endurance
Iver4-900	Survey	Torpedo	300	105	2.5	Side-scan sonar, compass, gyro, INS	Modular design, shallow water operations
SAUVIM	Intervention	Box-shaped	6000	6000	3.5	Sonars, cameras, ultrasonic motion trackers	Semi-autonomous manipulation
ALIVE	Intervention	Box-shaped	-	3000	4.0	GPS, INS, imaging sonar, cameras	7-function manipulator, autonomous docking
Aquanaut	Intervention	Transformable	300	1050	2.9	INS, DVL, Stereo Camera, Multibeam sonar, Laser scanner	Transformable design, hybrid operation
Girona 500	Intervention	Open frame	500	200	1.5	Mission configurable sensors	Reconfigurable payload, versatile operation
OceanOne	Intervention	Humanoid	500	200	1.8	Stereovision cameras	Humanoid design, bimanual manipulation

The evolution of intervention-capable AUVs reveals significant challenges in balancing capability with operational practicality. Early developments were characterized by robust but heavy designs. The ALIVE project, with its 7-DoF manipulator and autonomous docking capabilities, demonstrated one of the first successful autonomous underwater interventions, but its 3500 kg mass severely limited maneuverability and complicated deployment operations. SAUVIM, while achieving significant milestones in autonomous manipulation with its advanced control architecture, faced similar operational challenges due to its 6000 kg weight. More recent developments show progress toward more practical solutions. While more recent developments like the GIRONA 500 have achieved intervention capabilities in a more compact 200kg platform, and the Aquanaut has introduced an innovative transformable design weighing 1050kg, challenges remain in combining efficient locomotion with effective manipulation capabilities.

The autonomous exploration of underwater environments presents another critical challenge that current solutions have not fully addressed. The task of exploring a volume with given bounds

but unknown content requires accurate localization, multi-modal sensing, and reactive navigation capable of responding to environmental changes [159]. The underwater robotic exploration literature is notably scarce [121], reflecting the complexity of developing reliable solutions for this domain. Current approaches to underwater exploration often rely on basic coverage patterns, such as lawn-mower trajectories, which while ensuring complete coverage, fail to adapt to the specific requirements of close-range inspection tasks. The quality of sonar data varies significantly with acquisition distance and angle, creating a fundamental challenge in maintaining optimal sensing conditions throughout the exploration. For instance, multibeam sonars provide high-resolution mapping capabilities, with resolution varying based on factors like frequency, range, and beam configuration, but operating at close ranges increases collision risks and requires more sophisticated navigation control. Furthermore, existing approaches rarely consider the trade-off between data quality and operational safety, leading to either overly conservative exploration patterns or compromised data collection. Environmental factors add another layer of complexity to underwater exploration. Varying currents can affect vehicle stability and trajectory execution, while turbidity and changing lighting conditions can impact sensor performance. Most current solutions lack robust mechanisms for adapting exploration strategies based on real-time assessment of environmental conditions and data quality. This limitation becomes particularly evident in offshore environments where conditions can change rapidly and unpredictably.

A significant gap exists in the adaptation of state-of-the-art motion planners for underwater applications. While RRT-Connect [153] and other sampling-based planners have been successfully implemented in some underwater scenarios, they typically require significant modifications to handle the unique constraints of underwater operations. These include compensation for hydrodynamic effects that can vary with velocity and orientation, managing the coupled dynamics between vehicle and manipulator where forces in one system directly affect the other, and adapting to environmental uncertainties such as varying currents and visibility conditions. The field has largely developed application-specific solutions rather than adapting established planning frameworks, resulting in limited standardization and reusability. Furthermore, the field lacks standardized evaluation frameworks and performance metrics for underwater manipulation tasks. Current evaluation methods vary widely, from basic success rate measurements to complex multi-criteria assessments, making it difficult to objectively compare different approaches. The absence of standardized benchmarking protocols that consider factors such as energy efficiency, path optimality, and robustness to environmental disturbances hinders the systematic improvement of underwater manipulation capabilities.

These limitations in current underwater robotic systems highlight the need for innovative solutions that can address these challenges comprehensively. Future developments must focus on creating more efficient and practical vehicle designs that optimize the trade-off between hydrodynamic efficiency and manipulation capability, developing robust exploration strategies that can operate without prior environmental knowledge while maintaining data quality, and establishing standardized methods for evaluating and comparing different approaches in underwater robotics.

Chapter 3

Autonomous Underwater Vehicle for Inspection and Intervention of Underwater Structures

The evolution from short-term deployment platforms to persistent autonomous systems represents a critical advancement needed in underwater robotics, particularly for offshore wind farm operations. Achieving true persistent autonomy requires vehicles designed specifically for extended independent operation through several key innovations. The vehicle morphology must optimize both hydrodynamic efficiency and intervention capabilities, enabling stable hovering during manipulation tasks while maintaining efficient transit between inspection sites. Integration of heterogeneous sensors - including multibeam sonars, profiling sonars, and visual cameras - must be achieved while preserving streamlined design and minimizing operational weight, allowing comprehensive environmental perception without compromising vehicle dynamics. Strategic thruster configurations need to provide fine-tuned control in all 6 degrees of freedom, essential for both close-range inspection operations and precise manipulation tasks. The vehicle architecture should enhance reliability through system redundancy and independent subsystems, ensuring operational continuity even in case of partial failures. These design principles enable critical capabilities such as autonomous docking for battery recharging and data transfer, extended inspection missions without surface support, and complex intervention tasks including manipulation-based docking maneuvers. Such innovations in vehicle design would transform AUVs from platforms requiring frequent deployment and recovery to truly persistent autonomous systems capable of extended operations in offshore environments.

This chapter is organized as follows: section 3.2 presents RAYA's bio-inspired concept and design principles, including thruster configuration and sensitivity analysis. Section 3.3 details the hardware architecture and system functionalities, describing each module's role and capabilities. Section 3.4 details experimental validation across multiple scenarios and environments executed to validate the different aspects of RAYA, such as: navigation, perception, propulsion and system power. Lastly, in section 3.5 the conclusions and final specifications of the vehicle are discussed.

3.1 Introduction

Despite significant advances in autonomous underwater vehicle technology, current platforms face several challenges in achieving persistent autonomous operations. Traditional torpedo-shaped AUVs are optimized for survey tasks but lack the maneuverability required for complex intervention operations. Existing intervention-capable vehicles often rely on box-like open-frame designs that compromise hydrodynamic efficiency and generate significant drag forces during positioning tasks. Their substantial operational weights, frequently exceeding 1000 kg, necessitate specialized deployment equipment and increase energy consumption during precise maneuvering. Additionally, conventional designs struggle to optimally integrate multiple sensor types while maintaining efficient thruster configurations, leading to compromises in either perception capabilities or vehicle control.

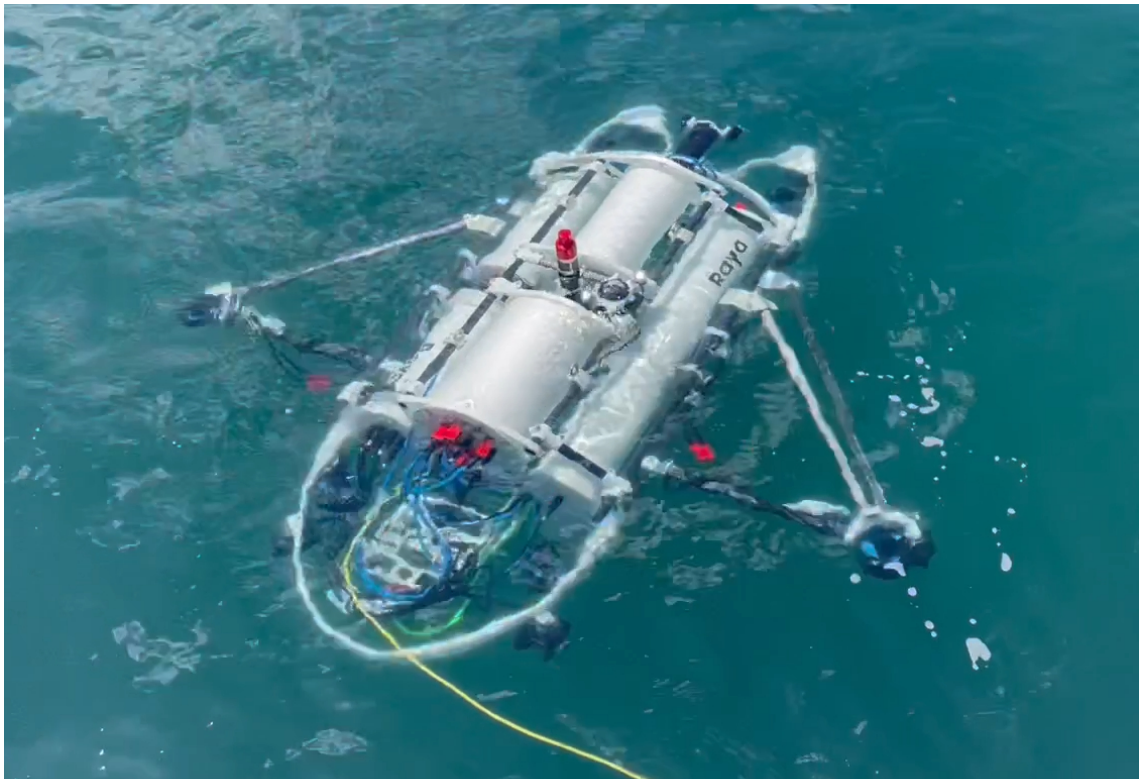

Figure 3.1: RAYA autonomous underwater vehicle.

To address these limitations, this chapter presents the design and development of a novel bio-inspired AUV that addresses the current challenges in underwater navigation and intervention tasks in offshore environments. RAYA (figure 3.1) represents an innovative approach to autonomous underwater operations, combining precise maneuvering capabilities with robust manipulation abilities in a compact and efficient platform, featuring multiple heterogeneous sensors for real-time data processing and a 6 DoF eletric manipulator. The major contributions of this chapter include innovations in both vehicle design and system integration. Drawing inspiration from manta rays, its streamlined morphology and strategic thruster placement enables high maneuverability needed

for close-range operations while maintaining hydrodynamic efficiency. RAYA's bio-inspired design allows for fine-tuned position and velocity control in all 6 DoFs, which combined with an electric manipulator capable of handling payloads up to 5 kg with high-precision joint positioning of 0.1°, enables sophisticated intervention tasks while maintaining stable vehicle positioning. The modular architecture enhances scalability and adaptability through independent subsystems: dual power cylinders provide redundant locomotor capacity for thrusters ensuring operational reliability, while separate cylinders house the system power, navigation, and perception modules. These design innovations are validated through comprehensive field trials demonstrating the vehicle's capabilities across multiple domains, from structural integrity and kinematic control to autonomous navigation and environmental mapping.

3.2 The RAYA AUV: a bio-inspired concept

In the first concepts of the AUV, enabling the vehicle to hover was a challenging issue, as the thrusters were too close to the CoM to generate enough momentum to balance the vehicle. Additionally, the open-frame structure generates significant drag forces, hindering its speed and water current operation. Specifically, in the field of AUV design, researchers have implemented bio-inspired solutions to replace the classic thruster propulsion system by fin propulsion [160, 161, 162]. The shape of the vehicle is also influenced by highly streamlined aquatic animals, which provides the vehicle with excellent hydrodynamic properties [163, 164, 165].

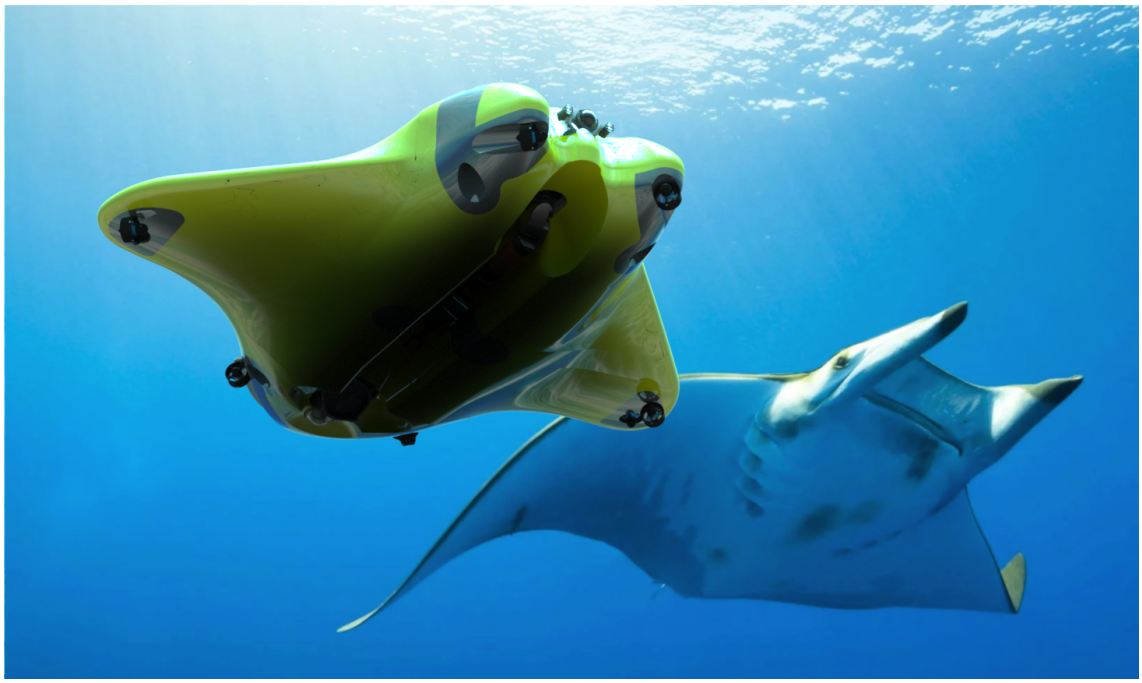

Figure 3.2: RAYA's biomimicry inspiration.

Adopting this design philosophy, RAYA has a manta ray bio-inspired Blended Winged Body (BWB) shape design, which is an already proven and established streamlined shape for underwater

locomotion, with excellent hydrodynamic characteristics when swimming or gliding [166]. The bio-inspiration is evidenced in figure 3.2, highlighting the vehicle's conceptual fairing. This fairing is still in the early design phase and has neither been constructed nor studied in detail. As such, all experiments in real environment showcased in section 3.4 and the dynamic model, that can be found in reference [167], were accomplished with the open-frame structure. Nevertheless, the manta ray concept design provides a streamlined body to house essential components, such as cylinders and sensors, and features two large-span wings. The smooth intersection between the body and wings of manta rays contributes to a reduced surface resistance, naturally enhancing hydrodynamic performance [168]. The wings also increase the overall moment of inertia of the AUV, making it more resistant to roll and pitch changes. During motion, an optimized wing design can balance lift forces that enhance horizontal stability. And during hovering operations, their large surface area provides additional damping and added mass effects that improve horizontal stability as well [169, 170]. Furthermore, this configuration allows for positioning thrusters farther from the CoM, extending the moment arms and improving the efficiency for executing tilting manoeuvres. An added benefit of this particular form is that the pincer-like shape at the front allows the front thrusters to be placed even further from the CoM without significantly restricting the manipulator range of motion.

RAYA's structure and shape are achieved using numerical analysis techniques that ensure an efficient design and accomplish a defined set of goals. Due to its bio inspired morphology, and strategic thruster configuration, the vehicle is capable of executing complex manoeuvres and hovering while performing inspection and intervention missions. Thus, the design of the RAYA AUV accounts for certain essential features:

- **Modular Arrangement:** The electronic components are distributed among five cylinders composing four different modules: mission control and navigation, perception, propulsion, and system power, where two of the cylinders are dedicated to propulsion. The dimensions of each module cylinder can be found in table 3.1. The AUV's design allows for easy removal and replacement of each cylinder, facilitating quick adjustments or replacements. This modular approach minimizes maintenance time and supports operational flexibility.

Table 3.1: Mechanical specifications of RAYA's cylinders.

Cylinders	Diameter [mm]	Length [mm]	Weight [kg]
2x Propulsion	200	1130	14.7
1x System power	200	530	31.4
1x Navigation	230	490	13.0
1x Perception	320	440	21.8

- **Load Distribution:** The design strategically positions carbon fiber–reinforced polymer (CFRP) tubes to handle the majority of the mechanical stress, while the Polyoxymethylene (POM) components bear significantly lower stress. This approach ensures that the critical stresses are distributed effectively, minimizing the risk of structural failure.

- **Buoyancy and Stability:** The combination of CFRP's low density and positive buoyancy of the POM components ensures that the vehicle maintains a balanced buoyancy. This design helps the AUV achieve a neutral or positive buoyancy state, allowing it to float to the surface if all thrusters are turned off.
- **Hydrodynamic Efficiency:** The vehicle's hull shape is inspired by bio-mimicry, specifically the manta ray. This streamlined, blended winged-body design reduces drag and improves hydrodynamic performance. The hull's shape contributes to enhanced stability and maneuverability, particularly during hovering and close-range inspection tasks. The pincer-like front shape facilitates optimal thruster placement, further enhancing the vehicle's balance and operational efficiency.

The requirements for the RAYA were discussed and validated based on the needs of offshore operations and maintenance tasks. As such, the main objectives of the system were defined: close range inspection of offshore structures and underwater interventions. For this, a list of the functional requirements is presented in table 3.2 pertaining to perception, navigation, and operational capabilities.

Table 3.2: System requirements for RAYA.

Configuration	AUV & ROV
Charging	Wired
Operating conditions	3 (Douglas sea scale)
Water currents	Maximum of 0.5 m/s
Manoeuvrability (DoFs)	Surge, sway, heave, yaw, pitch and roll
Operational capabilities	Underwater manipulation Visual inspection and guidance 3D structures detection Sea bed mapping Environment reconstruction
Operating depth	Up to 150 m
Remote operation delay	Movement: $<$ 10 ms Manipulator: $<$20 ms Other functions: $<$100 ms
Wireless comm	Up to 1 km
Comm bandwidth	500 kbps to 1 Mbps
Localization	GPS, IMU and DVL

The frame and hull design of the RAYA AUV is a critical aspect of its overall performance and functionality. Designed with a focus on strength, buoyancy, and hydrodynamic efficiency, the structure supports the vehicle's complex maneuvers and operational tasks. Key elements of the frame and hull design include:

- **Cylinders and frame:** The RAYA AUV is primarily composed of five sealed cylinders, as shown in figure 3.3, each dedicated to a crucial aspect of the vehicle's functionality:

- **Mission Control and Navigation:** This cylinder houses the vehicle's core navigation systems, including the Inertial Measurement Unit (IMU), Doppler Velocity Log (DVL), and GPS for precise positioning and obstacle avoidance.

- **Perception:** This cylinder contains sensors for environmental mapping and inspection, including three visual cameras, a multibeam sonar, and a pipe profiling sonar.

- **Propulsion Power and Actuation:** Two cylinders dedicated to managing the propulsion system. Each of these cylinders actuates six thrusters, providing comprehensive control over the vehicle's movement.

- **System Power:** Provides overall power to the vehicle's systems, ensuring continuous operation.

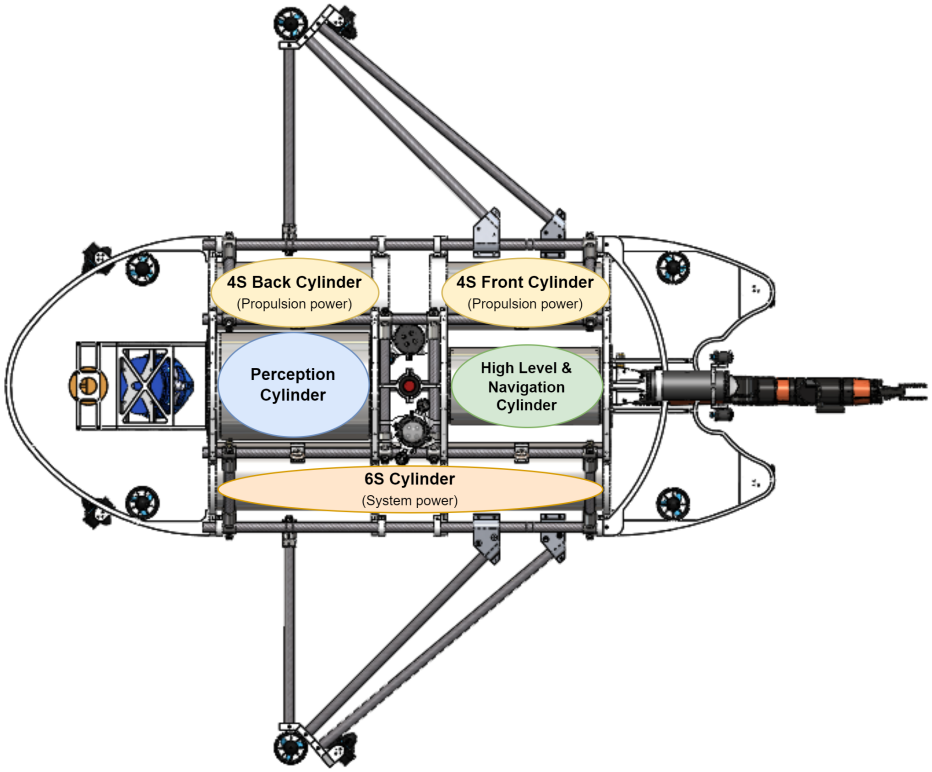

Figure 3.3: RAYA's cylinders (names and locations).

The cylindrical modules housing all essential electronic components, including batteries, computers, and communication devices, are made from Polyoxymethylene, which offers ease of machining and cost-effectiveness. The frame that supports these cylinders and sensors is constructed from Carbon Fiber Reinforced Polymer tubes and anodized AW 6061 aluminum connectors. This combination ensures that heavier loads are transferred effectively to the CFRP tubes, which provide higher strength and stiffness compared to POM.

- **Support Structures:** Additional support structures, also crafted from POM, position and secure various sensors and actuators such as sonars, visual cameras, thrusters, and the manipulator. These structures are produced through conventional milling, which ensures precision and cost-effectiveness. The flexibility of POM allows for quick alterations or replacements as needed.

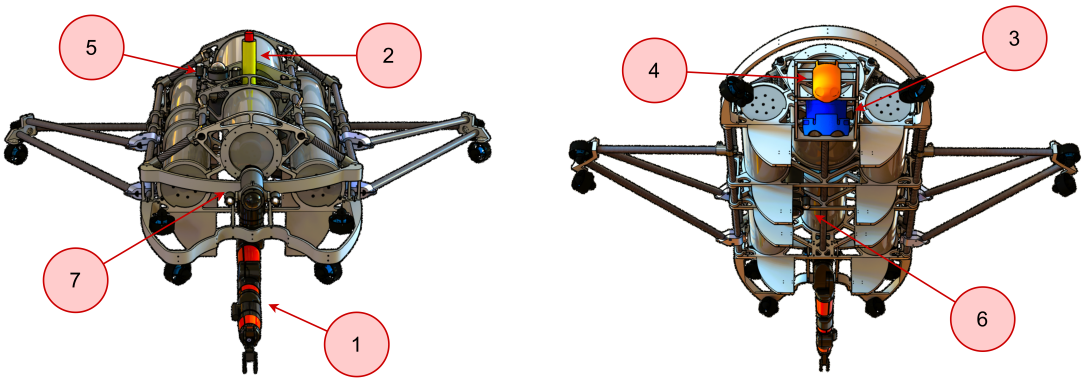

Figure 3.4: RAYA AUV open frame design and exposed sensors/actuators: (1) 6 Dof manipulator arm - Bravo7; (2) Profiling sonar - Profiler 831L; (3) Multibeam sonar - M3 sonar; (4) DVL - Nortek DVL 300; (5) Top facing camera; (6) Bottom facing camera; (7) Front facing camera.

RAYA is equipped with high-level mission control and vehicle navigation using an inertial measurement unit, a doppler velocity log, and a global positioning system localization for precise positioning and potential obstacle avoidance. RAYA's perception module collects and processes data from three visual cameras, a multibeam sonar, and a pipe profiling sonar for mapping structures. The vehicle is prepared to be equipped with a 6 degree of freedom manipulator and can lift objects of up to 5 kg apparent weight. The weight and general description of the different sensors and actuators equipped outside the cylinders can be found in table 3.3. An image of the RAYA's open frame design can be found in figure 3.4 where the exposed sensors and manipulator are identified.

Table 3.3: Description and weight of RAYA's exposed sensors and actuators.

Sensors	Description	Weight [kg]
1x M3 sonar	Multibeam sonar	4.6
1x Nortek DVL 300	Doppler velocity log	1.3
12x T200	Thrusters	0.344
1x Bravo 7	6 DoF manipulator	9.5
1x Profiler 831L	Profiling sonar	1.2
3x Camera	Visual inspection	0.8

Thruster's configuration and sensitivity analysis

The buoyancy force acts upon the center of buoyancy (CoB), in the opposing direction of gravity. A key part of designing an AUV is analysing its CoB and CoM. For the vehicle to float, the resulting force, between gravity and buoyancy, must be positive. Consider the position of the vehicle, in the local coordinate frame, defined as $\boldsymbol{q} = [x_B, y_B, z_B]$, any deviations in the $x_B y_B$ plane (horizontal), between the CoM and the CoB will cause a righting moment over a pivot point located between the two centres, over which the body will rotate until the centres are vertically aligned [171]. If the centres are close and aligned, the thrusters spend less energy in righting the vehicle's orientation, allowing for longer operation times. Figure 3.5 shows the origin of the global frame of reference, and the positive axis direction of the thrusters. The CoM and CoB of the whole vehicle can be written as:

$$CoM = \frac{\sum(Component_{CoM} \times Component_{Mass})}{\sum Component_{Mass}}, \tag{3.1}$$

$$CoB = \frac{\sum(Component_{CoB} \times Component_{Volume})}{\sum Component_{Volume}}. \tag{3.2}$$

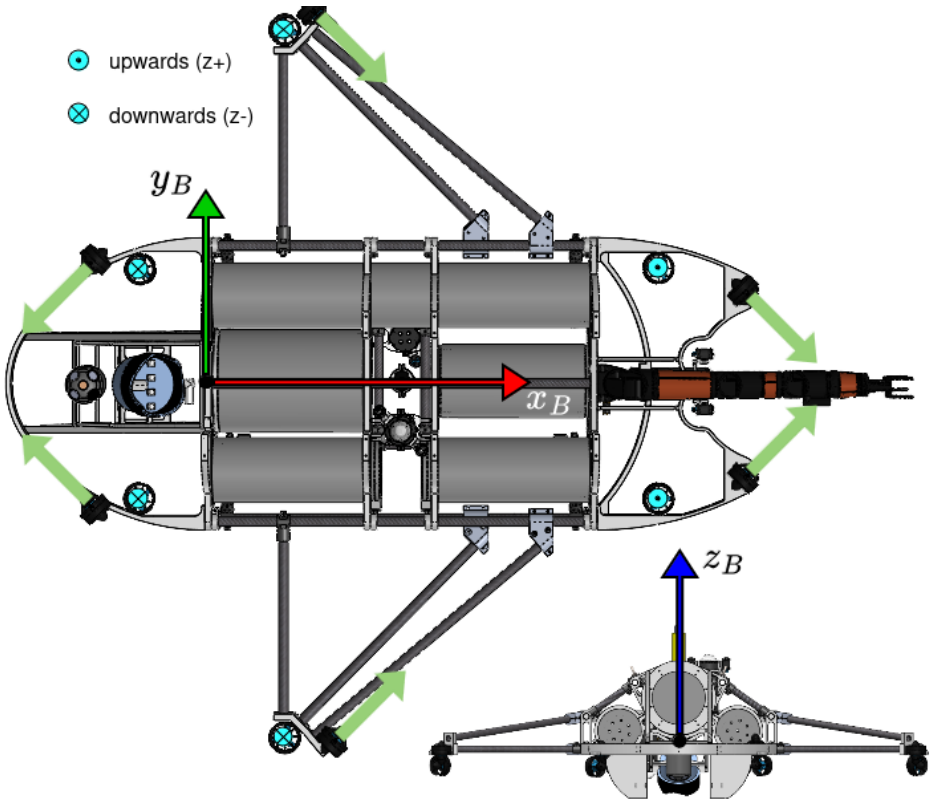

Figure 3.5: Vector representation of the RAYA's thrusters. The horizontal thrusters are represented by the green arrows at a 45-degree angle with the x_B axis (red). The vertical thrusters are represented by the light blue circles.

Due to the shift of the CoM provoked by the manipulator's movement, a sensitivity analysis must be performed to validate the placement of the thrusters. For this purpose, four critical scenarios were considered:

- **Scenario 1:** A full rotation of the vehicle about the x_B axis in travelling state;
- **Scenario 2:** A full rotation of the vehicle about the y_B axis in travelling state;
- **Scenario 3:** A full rotation of the manipulator in the $x_B y_B$ plane while the vehicle is hovering, as shown in figure 3.6;
- **Scenario 4:** A full rotation of the manipulator while holding a 5 kg payload in the $x_B y_B$ plane, and the vehicle is hovering. The payload is a block of steel with density, 7750 kg/m^3.

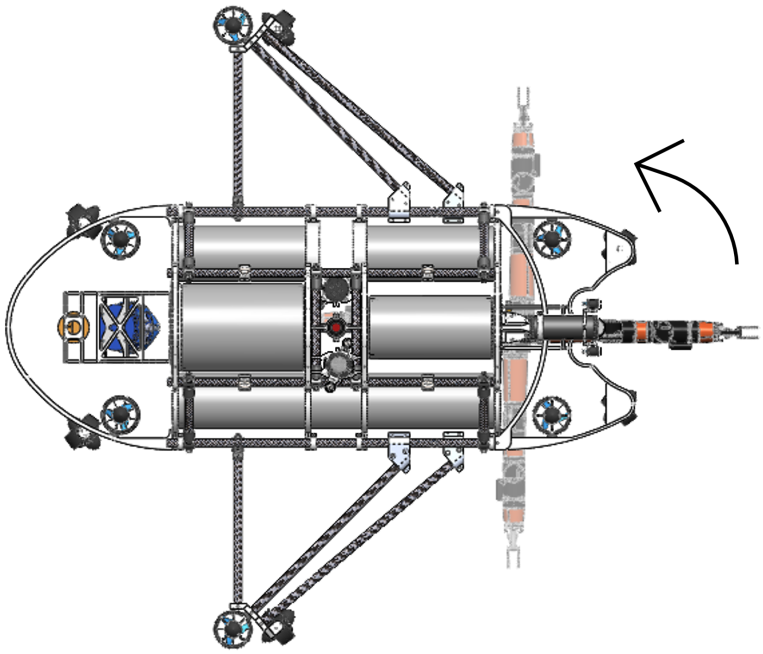

Figure 3.6: Manipulator movement during critical scenarios number 3 and 4.

In a travelling state (scenarios 1 and 2), the manipulator is retracted towards the back of the vehicle, as shown in figure 3.7. In this configuration, the CoM is located at $[558.7, -2.4, 66.2] \times 10^{-3}$ m and the CoB is located at $[558.8, -3.0, 99.6] \times 10^{-3}$ m. Gravity exerts a total downwards force of 1648.3 N, and the surrounding water exerts a total upwards force of 1654.5 N, confirming that the vehicle is positively buoyant, with a resulting force of 6.2 N.

For scenarios 3 and 4, the manipulator performs a rotational movement as illustrated in figure 3.6. The CoM and CoB shift can be observed in figure 3.8 and figure 3.9, respectively. While the payload causes larger variations in the CoM, the CoB is not as affected due to the considered material's high density. These leads to larger distances between the two centers, and therefore, larger righting moments.

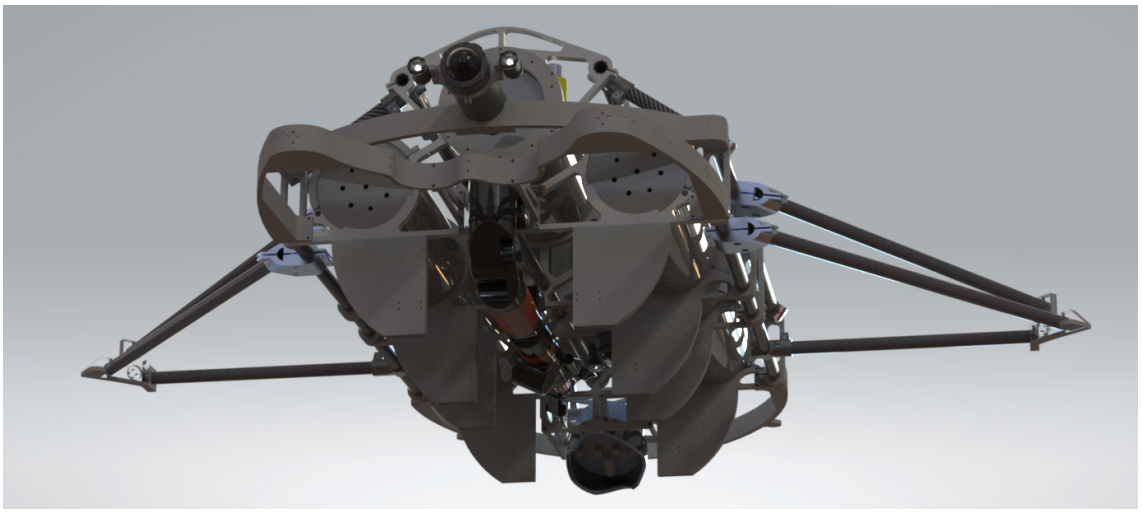

Figure 3.7: RAYA's travelling configuration: manipulator accommodated below the cylinders.

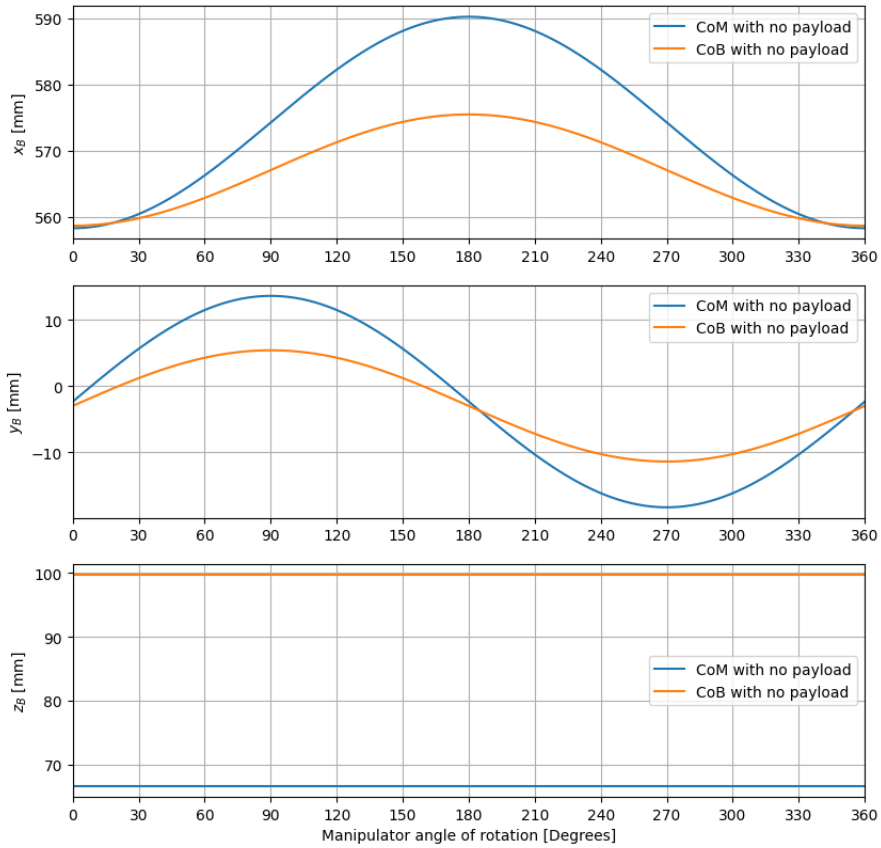

Figure 3.8: RAYA's CoM and CoB shift with no payload.

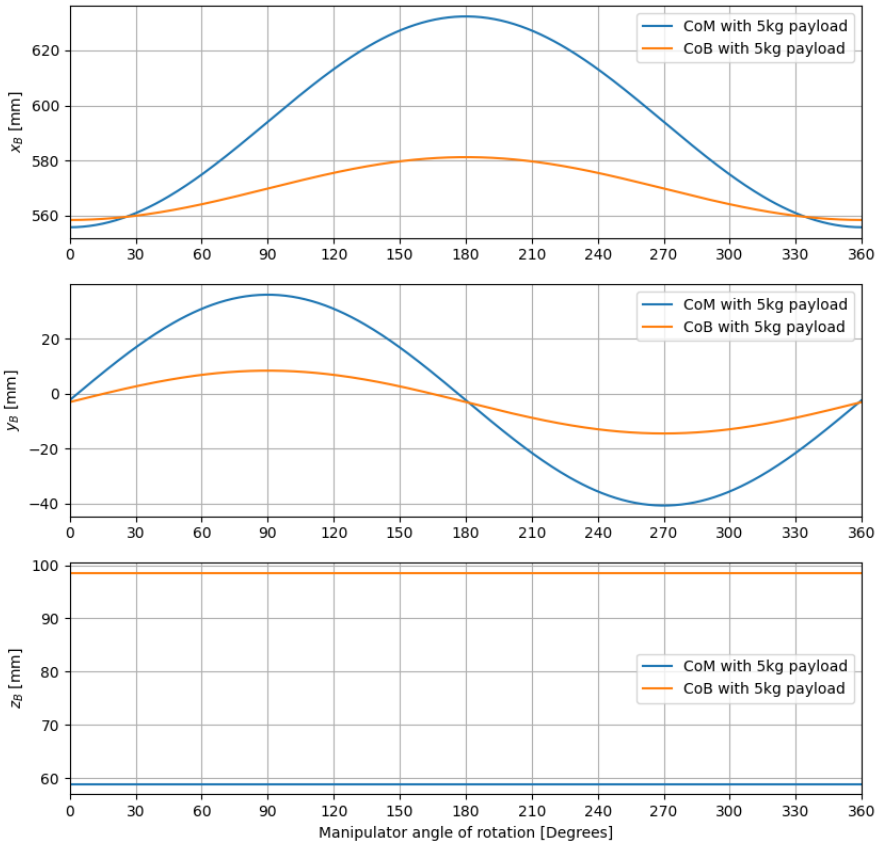

Figure 3.9: RAYA's CoM and CoB shift with 5 kg payload.

Considering the pose of the AUV relative to a global fixed frame as $\boldsymbol{\eta} = [x_N, y_N, z_N, \phi_N, \theta_N, \psi_N]$, where $[x_N, y_N, z_N]$ represent the translation of the vehicle along the respective axes, and $[\phi_N, \theta_N, \psi_N]$ represents the roll, pitch, and yaw of the vehicle. Based on the expression given by Fossen [172] for a 6 DoF nonlinear dynamic equation of motion, the dynamic model of the RAYA AUV can be expressed as:

$$\boldsymbol{M}\dot{\boldsymbol{\nu}} + \boldsymbol{C}(\boldsymbol{\nu})\boldsymbol{\nu} + \boldsymbol{D}(\boldsymbol{\nu})\boldsymbol{\nu} + \boldsymbol{g}(\boldsymbol{\eta}) = \boldsymbol{\tau}, \tag{3.3}$$

where $\dot{\boldsymbol{\nu}}$ and $\boldsymbol{\nu}$ are the acceleration and velocity vectors of the body fixed frame, $\boldsymbol{M}$, $\boldsymbol{C}(\boldsymbol{\nu})$, and $\boldsymbol{D}(\boldsymbol{\nu})$, are the system's inertia matrix, the Coriolis centripetal matrix, and the damping matrix, respectively, and $\boldsymbol{\tau}$ is the vector of control inputs. The parameters of these matrices, excluding $\boldsymbol{g}(\boldsymbol{\nu})$ (which is shown in equation 3.7) can be found in Leitão's work [167]. The parameters were obtained via CFD, with the software OpenFoam for the open-frame vehicle. Considering the thruster force vector $\boldsymbol{f} = [f_x, f_y, f_z]^T$, the moment arms $\boldsymbol{l} = [l_x, l_y, l_z]^T$ as the distance of the

thrusters to the local origin coordinate, and C and S as $\cos(\pi/4)$ and $\sin(\pi/4)$, respectively, and representing the orientation of the horizontal thrusters, the configuration matrix of the thrusters, $\boldsymbol{T}$, can be defined as:

$$\boldsymbol{T} = \begin{bmatrix} \boldsymbol{T}_v & \mathbf{T}_h \end{bmatrix} \in \mathbb{R}^{6\times 12}, \tag{3.4}$$

$$\boldsymbol{T}_v = \begin{bmatrix} 0 & 0 & 0 & 0 & 0 & 0 \\ 0 & 0 & 0 & 0 & 0 & 0 \\ 1 & -1 & -1 & 1 & -1 & -1 \\ l_y & -l_y & -l_y & l_y & -l_y & -l_y \\ -l_x & l_x & l_x & -l_x & l_x & l_x \\ 0 & 0 & 0 & 0 & 0 & 0 \end{bmatrix}, \tag{3.5}$$

$$\boldsymbol{T}_h = \begin{bmatrix} C & C & -C & C & C & -C \\ S & S & S & -S & -S & -S \\ 0 & 0 & 0 & 0 & 0 & 0 \\ -Sl_z & -Sl_z & -Sl_z & Sl_z & Sl_z & Sl_z \\ Cl_z & Cl_z & -Cl_z & Cl_z & Cl_z & -Cl_z \\ Sl_x - Cl_y & Sl_x - Cl_y & -Sl_x + Cl_y & -Sl_x - Cl_y & -Sl_x - Cl_y & Sl_x + Cl_y \end{bmatrix}. \tag{3.6}$$

Considering that each thruster is identified by a three-letter code referring to its position and orientation: F-front; M-middle; B-back; R-right; L-left; V-vertical; H-horizontal, T is the configuration matrix of the vertical and horizontal thrusters in the following order: FRV, MRV, BRV, FLV, MLV, BLV; FRH, MRH, BRH, FLH, MLH, BLH.

The matrices $\boldsymbol{M}$, $\boldsymbol{C}(\boldsymbol{\nu})$, and $\boldsymbol{D}(\boldsymbol{\nu})$, affect the vehicle's motion by influencing the dynamics, but they are not critical in determining the vehicle's ability to complete maneuvers. This is because these matrices primarily affect the rate at which the vehicle responds to inputs, but do not fundamentally limit the vehicle's maneuverability as they are proportional to either the vehicle's velocity or acceleration. Instead, maneuverability is primarily determined by the restoring forces, represented by $\boldsymbol{g}(\boldsymbol{\eta}) \in \mathbb{R}^6$. Thus, for the purpose of this analysis, $\boldsymbol{\tau} = \boldsymbol{g}(\boldsymbol{\eta})$. The vector of gravitational/buoyancy forces and moments, $\boldsymbol{g}(\boldsymbol{\eta})$, can be expressed as:

$$\boldsymbol{g}(\boldsymbol{\eta}) = \begin{bmatrix} (W+B)sin(\theta_N) \\ -(W+B)cos(\theta_N)sin(\phi_N) \\ -(W+B)cos(\theta_N)cos(\phi_N) \\ -(y_gW + y_bB)cos(\theta_N)cos(\phi_N) + (z_gW + z_bB)cos(\theta_N)sin(\phi_N) \\ (z_gW + z_bB)sin(\theta_N) + (x_gW + x_bB)cos(\theta_N)cos(\phi_N) \\ -(x_gW + x_bB)cos(\theta_N)sin(\phi_N) + (y_gW + y_bB)sin(\theta_N) \end{bmatrix}, \tag{3.7}$$

where W is the gravity force, B is the buoyancy force, and $[x_g, y_g, z_g]$ and $[x_b, y_b, z_b]$ are the local positions of the CoM and CoB, respectively.

Given that the $\boldsymbol{T}$ matrix is singular, the total force exerted by each thruster, represented by the vector $\boldsymbol{t}$, can be calculated as:

$$\boldsymbol{t} = \boldsymbol{T}^{\dagger}\boldsymbol{g}(\boldsymbol{\eta}), \text{where } \boldsymbol{t} \in \mathbb{R}^{12}. \tag{3.8}$$

Following this procedure, it is possible to map the force exerted by each thruster for any given configuration. For each scenario, the forces exerted by the thrusters can be seen in figure 3.10, where only the vertical thrusters are shown, since the horizontal thrusters do not contribute significantly to balancing the body.

The upper and lower limits are defined by the thruster's capacity: 5.25 kgf in the positive direction, and 4.1 kgf in the negative direction. In scenario 1, the forces applied by the thrusters are antisymmetrical in the $x_B z_B$ plane (vertical plane that crosses the mid-section of the vehicle), with the middle thrusters being the most overworked, reaching 22 N when the vehicle is at a roll of 90 degrees. In scenario 2, the forces applied by the thrusters are symmetrical in the $x_B z_B$ plane,

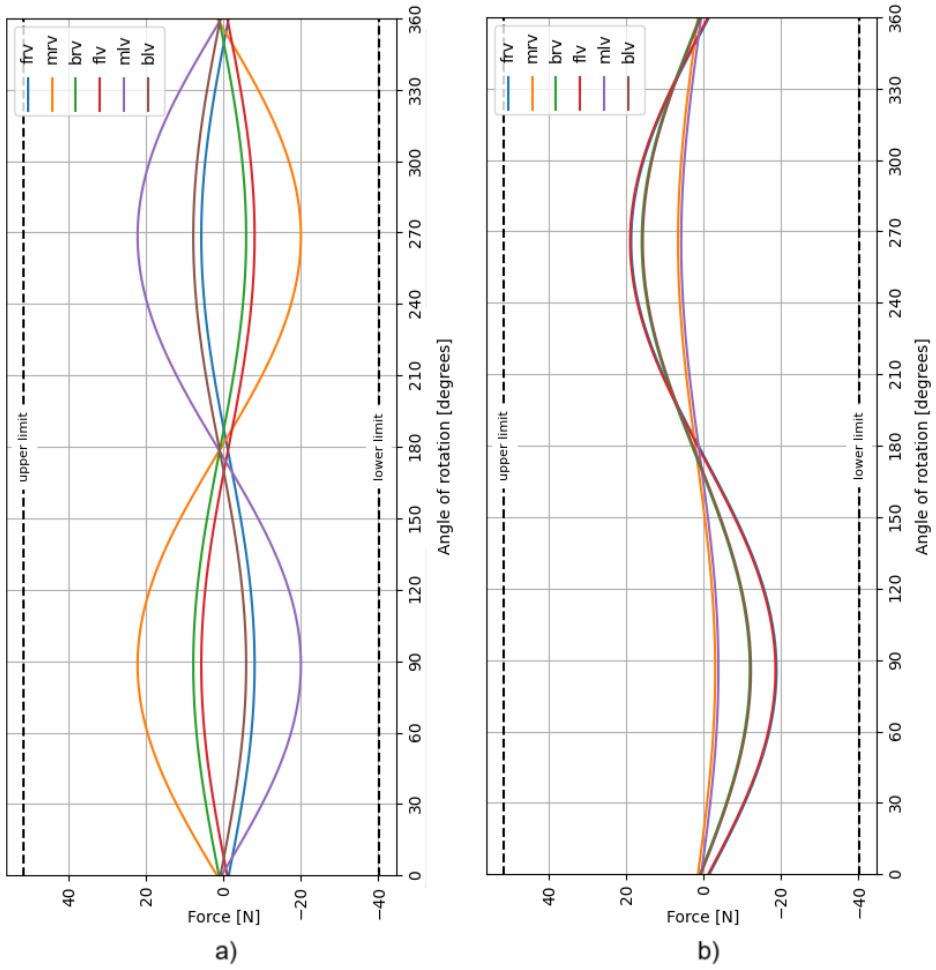

Figure 3.10: Thruster sensitivity analysis in each scenario. Figures (a) and (b) depict the forces exerted by the thrusters for a full rotation in roll and pitch.

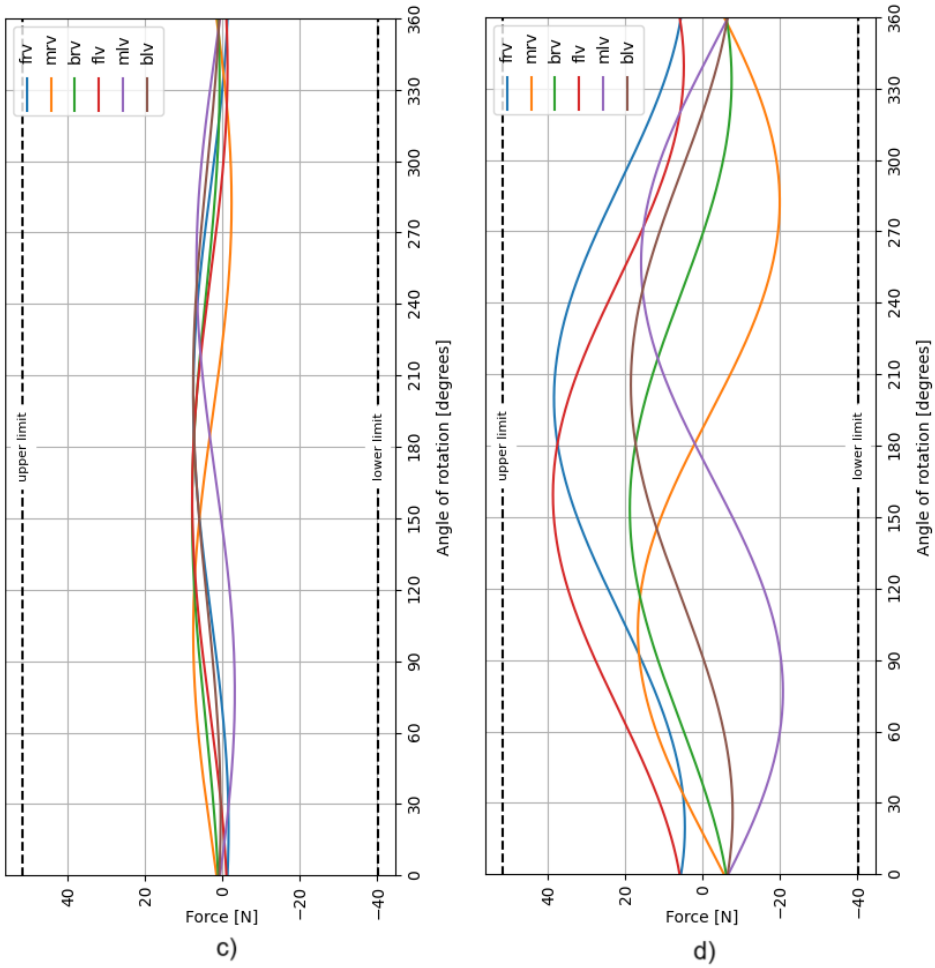

Figure 3.10: Figures (b) and (c) show the forces exerted by the thrusters for a full rotation of the manipulator, in the $x_B y_B$ plane, without and with a 5Kg payload.

with the front thrusters being the most overworked, reaching 19 N when the vehicle is at a pitch of 90 degrees. Scenarios 3 and 4 are similar, except that, due to the payload, the magnitudes of the forces are much larger in scenario 4. In scenario 3, the thrusters all reach similar maximums at different points in the manipulator's rotation. However, the maximum value registered is 7.7 N at 154 degrees for the back thrusters. In scenario 4, the front thrusters exert more effort than the others, with a maximum value of 38.5 N at 159 degrees. In its travelling state, the maximum effort is 1.4 N for the front thrusters. Overall, this analysis shows that the thruster positioning is capable of performing these 4 critical scenarios. Even if some of these positions are not achievable, since the manipulator cannot perform a full rotation in the $x_B y_B$ plane due to collisions with the body, the fact that the thrusters have sufficient force to complete the critical scenarios, they are capable of achieving any maneuver and perform intervention missions while hovering.

3.3 Hardware Architecture and System Functionalities

This section presents the overall architecture of the vehicle is described, and the composition of each cylinder previously presented. RAYA has a modular architecture, with five modules. This structure allows the division of the components based on the different aspects of the vehicle. Four distinct main aspects of the vehicle were considered: navigation, perception, propulsion and system power. Figure 3.11 presents the overall architecture of RAYA, with its five modules. The proposed architecture focuses the computation units and power related systems inside each unit. The sensors and actuators relevant to each module are placed outside, but directly connected to each unit. All the modules in the vehicle are connected through ethernet and use the robot operating system (ROS) framework to create the data bridges between them, allowing communication and data sharing between all modules.

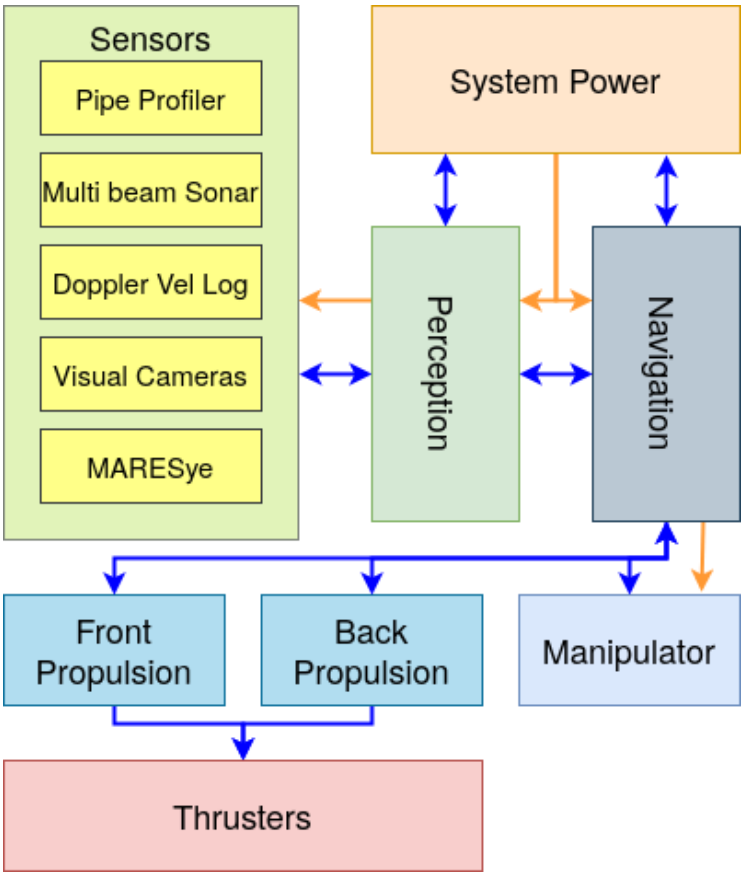

Figure 3.11: High-level architecture of the electronic systems that compose the vehicle RAYA. The system is composed by five modules, representing the four main aspects of the vehicle: Navigation, perception, propulsion and power. The sensor and actuators external to these elements are also represented. Blue lines represent Ethernet connections between modules and components, and orange lines represent the power connections.

3.3.1 Mission Control and Navigation Module

High-level mission control and vehicle navigation are handled by the navigation module (represented in figure 3.12). The high-level mission control is responsible for all decisions related to planning and scheduling of all actions of the vehicle, and is performed by a dedicated computing unit commanding the remaining units, based on the task being performed. Additionally, the control of the manipulator for intervention tasks is also performed by this computing unit, using the data collected by the perception module to ensure the safety of the manipulation operation. Navigation is also handled by a dedicated unit, which receives commands regarding target positions and trajectories from the high-level mission control. For navigation, both inertial measurements and DVL are used, providing two sources of data pertaining to the navigation and position of the vehicle, increasing its precision and reliability. When navigating at the surface, GPS localization is available and complements the navigational system. From this data and the kinematics of the vehicle, the calculation of the thruster firing configuration to reach the objective destination is performed. Power for all components involved, as well as sensors, is provided externally by the power module, and converted internally, based on the need of each component or sensor. Thus, this module is responsible for both underwater manipulation and navigation functionalities.

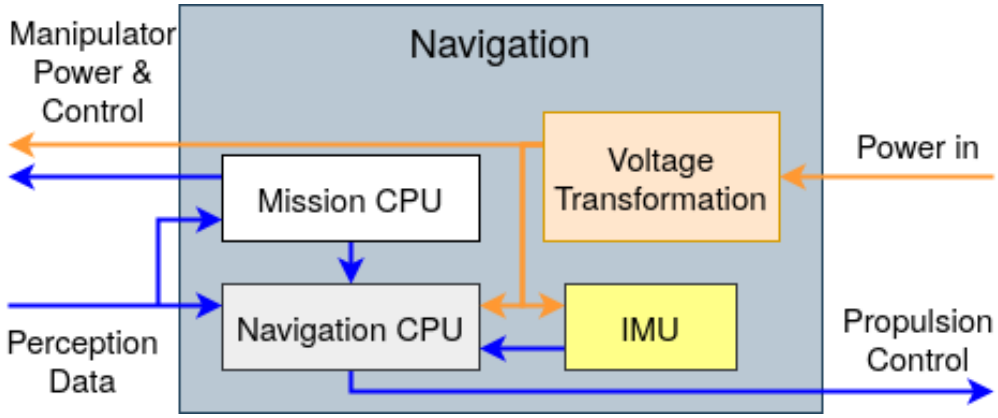

Figure 3.12: Internal structure of the navigation unit, containing its components, as well as the connection to external sensors and other units. The orange lines correspond to power connections, while the blue arrows represent network connections between internal components, external sensors and other modules.

Underwater manipulation

As an intervention vehicle, RAYA is prepared to be integrated with a 6 DoF robotic manipulator (Bravo7 manipulator from Reach Robotics[1]), which is positioned at the front of the vehicle. While moving, and when not in use, the manipulator is safely positioned under the vehicle. For intervention and manipulation operations, the manipulator is extended beyond the front of the vehicle, as represented in figure 3.13. This manipulator can operate at a depth of up to 300 meters. With

[1] *REACH Bravo* URL: `https://reachrobotics.com/products/manipulators/reach-bravo/`, accessed at December 2024

Bravo 7 equipped, RAYA is capable of manipulating objects of up to 5 kg apparent weight with a high accuracy joint positioning of 0.1°.

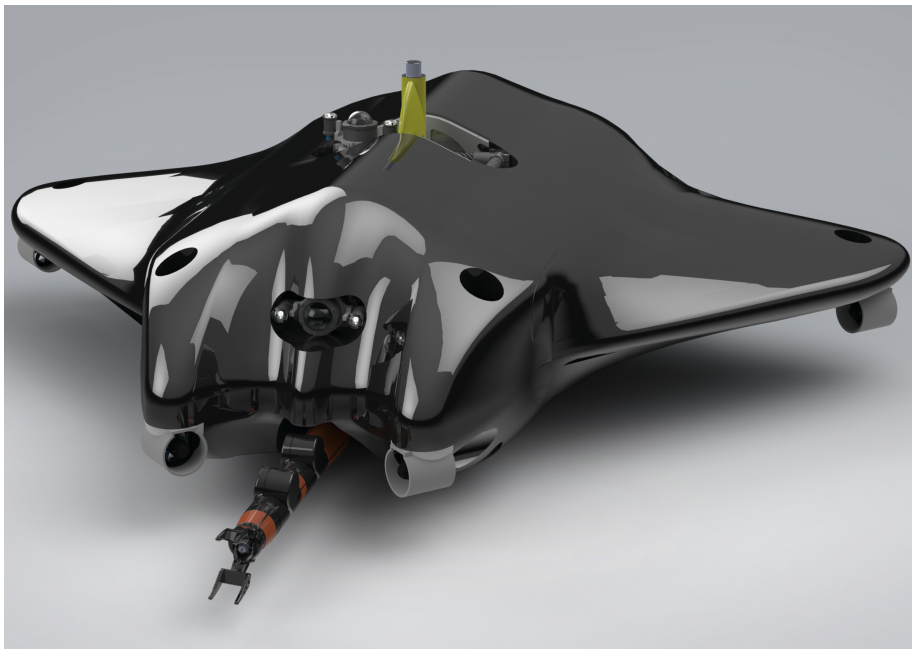

Figure 3.13: RAYA with the underwater manipulator fully extended.

Localization

One important component for correct movement and operation control is reliable knowledge of the vehicle's position. For this purpose, RAYA is equipped with multiple sensors to calculate and correct the vehicle's localization during operation. When operating at surface level, the vehicle uses an real time kinematic (RTK) GPS Holybro F9P[2], to provide accurate positioning data. However, since no GPS data is available when submerged, the vehicle uses a Nortek DVL 300[3] that provides accurate velocity data relative to the seabed and a KVH 1750 IMU[4] fiber optic gyro (FOG) IMU for real-time acceleration and angular velocity data, allowing the vehicle to track its orientation and compensate for drift during maneuvers. The GPS antenna is placed next to the pipe profiling sonar and cameras, at the center of the vehicle. The DVL is housed at the rear of the vehicle behind the multi-beam sonar, to allow for an unobstructed measuring of the velocity of the vehicle. The IMU is positioned inside the navigation module.

The vehicle's 6 DoF localization is estimated through the fusion of both the DVL and IMU, using an Extended Kalman Filter (EKF) and a similar methodology to that described by Campos et al. [173]. Since the sensors are asynchronous and do not measure all state vector variables

[2] *Holybro Docs* URL: https://docs.holybro.com/gps-and-rtk-system/f9p-h-rtk-series/standard-f9p-uart/download, accessed at December 2024

[3] *DVL 1000 - 300 m* URL: https://www.nortekgroup.com/products/dvl-1000-300m/pdf, accessed at December 2024

[4] *KVH 1750 IMU* URL: https://www.ion.org/jnc/upload/files/1450_1750%20IMU%20Comm%20Datasheet%200715%20(2).pdf, accessed at December 2024

independently, the EKF is responsible for predicting RAYA's pose throughout time when no sensor measurement exists by using an omnidirectional motion model. When a new sensor reading is received, the estimate is corrected. The EKF inputs consist of the IMU angular velocity and the DVL linear velocity data. In the future, the linear acceleration data from the IMU will be added to the EKF using absolute attitude data (roll, pitch and yaw) from a Xsens MTi-630 IMU[5]. This sensor will allow for gravity vector subtraction, as the FOG IMU only provides values relative to its initialization state. Finally, the positional information of retrieved from the GPS will be added to the filter as well, to estimate RAYA's position globally, while at the surface.

3.3.2 Perception Module

The perception module of RAYA (figure 3.14) contains a processing unit responsible for the collection and computation of all perception data in real-time, as well as running all processes required for the acquisition, filtering and visualization of the data. The sensor payload for this module includes visual cameras and sonars. Additionally, RAYA is required to both perceive and interact with the environment. Therefore, the perception module is prepared to accommodate the MARESye perception system [106, 105] fixed to the manipulator (eye-in-hand configuration), which can be used for close range inspection tasks and allows for the reconstruction of the working environment during intervention tasks. All sensors are connected to the vehicle's network, for easy data transfer between modules. Similarly to the Navigation module, power for each component and sensors is provided externally from the power module, and converted internally based on the needs of each component and/or sensor. Thus, this module is responsible for visual inspection and guidance, 3D structures detection and seabed mapping functionalities.

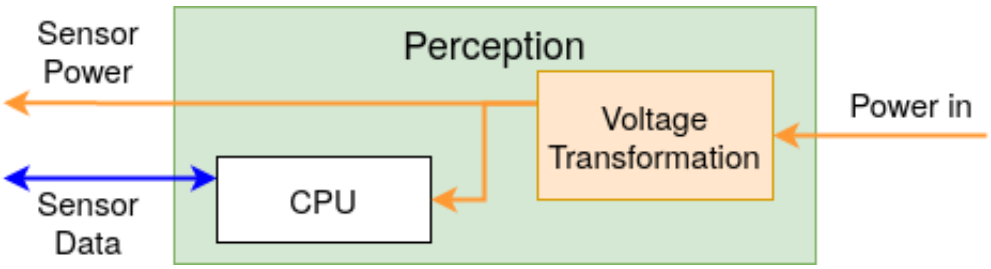

Figure 3.14: Internal structure of the perception unit, containing its components, as well as the connection to external sensors and other units. The orange lines correspond to power connections, while the blue arrows represent network connections between internal components, external sensors, and other modules.

Visual inspection and guidance

As an inspection vehicle, the ability of providing a detailed visual information to an operator (or for *post-hoc* analysis) is extremely relevant. Additionally, this visual information can be crucial

[5] *MTi-630* URL: `https://www.xsens.com/hubfs/Downloads/Leaflets/MTi-630.pdf`, accessed at December 2024

for guiding the vehicle's movements during remote navigation. Thus, RAYA is equipped with three visual cameras (two TIS-DFK-33GX273 and one TIS-DFK-33GX265, from The Imaging Source), which provide visual feedback of the surroundings of the vehicle. These cameras, with a maximum resolution of 1440x1080 (1.6 MP) with up to 75 fps, and 2048x1536 (3.1 MP) with up to 36 fps, respectively, are able to provide clear and detailed images of the surroundings, while possessing a small footprint and being lightweight. In terms of positioning, two of the three cameras are positioned at the centre of the vehicle to provide both an upward and downward view of the environment, with the third camera positioned at the front of the vehicle for forward-facing navigation and obstacle detection. The cameras are each accompanied by a set of two lights with 15000 lumens each to improve visibility at higher depths.

Obstacle avoidance

Safe navigation near underwater structures requires reliable obstacle detection and avoidance capabilities. For this purpose, RAYA is equipped with an Imagenex 831l[6] digital pipe profiling sonar, located at the center of the vehicle, and is capable of scanning 360° up to a distance of 6 m from the center of the sensor. The sensor's angle resolution and range allow the proper detection and mapping of structures surrounding the vehicle, which can be targeted for closer inspection.

Seabed mapping

Inspection of the seabed is a common task performed during O&M operations, as it allows not only the assessment of problems such as scour, but also to identify the position and state of underwater elements, such as anchors and cables. For this reason, RAYA is equipped with a M3 multibeam sonar[7], which has a range between 0.2 and 150 m and can operate up to 500 m depth. The M3 multibeam sonar is placed at the rear end of the vehicle, aiming downwards at an angle of 45°.

3.3.3 Propulsion modules

The internal architecture of RAYA's propulsion modules is represented in figure 3.15. These modules are responsible for powering and controlling the thrusters for the movement and stabilization of the vehicle. RAYA contains two of these modules, each responsible for controlling half of the thrusters of the vehicle. The two modules are symmetrical, with one controlling the front and right wing thrusters and the other the rear and left wing thrusters. Each of the modules is fully powered by internal batteries, which also power the thrusters. Each module also contains a processing unit, which interprets the velocity commands for each thruster, provided by the navigation module, using a set of drivers that are connected to each of the thrusters.

[6] *IMAGENEX MODEL 831L* URL: https://imagenex.com/assets/images/downloads/831L_Manual.pdf, accessed at December 2024

[7] *M3 SONAR - 500M* URL: https://www.graftek.com.tr/dosya/922-20017901-12-500m-1-pdf/356/, accessed at December 2024

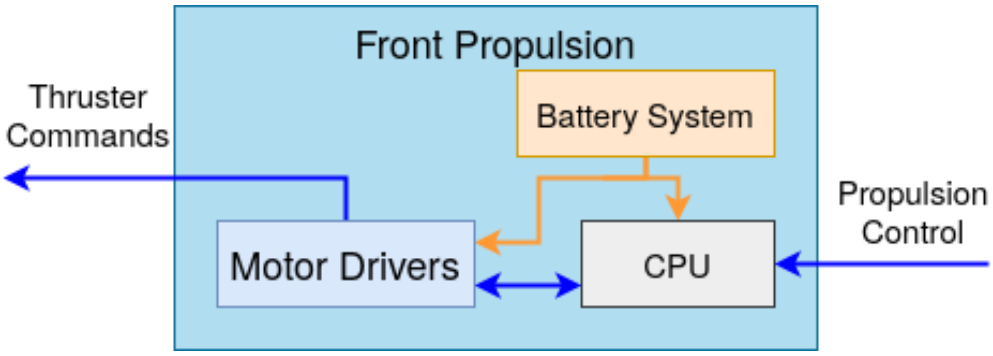

Figure 3.15: Internal structure of the propulsion module responsible for powering and controlling the thrusters in the front of the vehicle. It contains a computing unit, motor drivers to drive each thruster, and a battery system that powers the module and motors. The blue arrow represents the network connection with the other modules.

A significant feature of RAYA's propulsion system is the inclusion of two independent power cylinders, which serve as a robust failsafe mechanism. Each power cylinder is capable of independently providing the AUV with sufficient locomotor capability. This redundancy is a critical safety feature, ensuring that in the event of a failure in one propulsion module, the other module can take over and maintain the vehicle's operational capabilities. The redundancy offered by the two power cylinders enhances the reliability of the AUV, particularly in challenging and hazardous underwater environments for which failure is not an option. By having a redundant system that can independently manage the vehicle's movement, the proposed solution ensures that RAYA can continue its mission or return to a safe location even if one propulsion module encounters an issue.

3.3.4 System power module

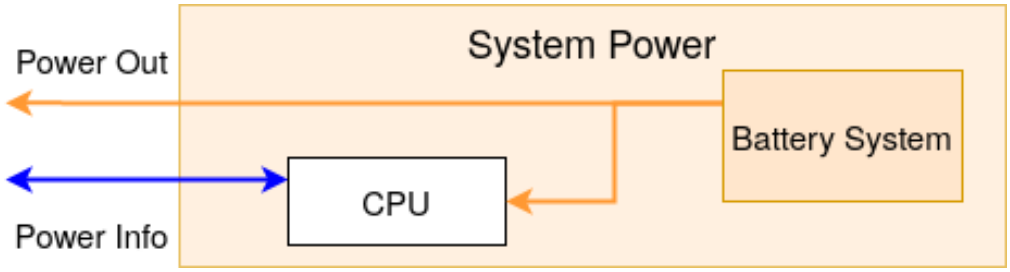

Figure 3.16: Internal structure of the System Power module, responsible for powering the perception and navigation units, as well as the manipulator. It contains its components, as well as the connection to external sensors and other units. The orange lines correspond to power connections, while the blue arrows represent network connections between internal components, external sensors and other modules.

The System Power module, represented as figure 3.16, is responsible for providing power to the Perception and Navigation modules, and respective sensors, as well as the manipulator. Similarly to the propulsion module, it contains a battery system and a computing unit. This processing

unit provides information on the state of the batteries, such as remaining charge, and allows an operator to disable the power to the other modules.

3.4 Experimental validation

To validate the operational capabilities of the AUV, a comprehensive testing methodology was developed and executed through a series of increasingly complex trials. The testing strategy progressed from fundamental system validation to full operational capability assessment through three distinct phases:

1. Laboratory and controlled environment tests were conducted at the ATLANTIS test centre to validate basic vehicle functionality. These tests focused on two critical aspects: validating the structural integrity of the vehicle design and verifying the kinematic control system's performance. The buoyancy tests ensured proper weight distribution and center of mass alignment, while kinematic trials verified the accuracy of the thruster configuration and control algorithms;

2. The vehicle's perception systems were evaluated through reconstruction tasks in a controlled indoor pool environment at CRAS laboratory. This environment provided controlled conditions to assess the accuracy of the sonar and vision systems, enabling precise measurement of reconstruction errors and validation of sensor integration. The structured environment of the pool, with known dimensions and clear features, served as a calibrated reference for evaluating the perception system's performance.

3. Real environment missions were conducted at Porto de Leixões to validate the vehicle's capabilities in operational conditions. These tests included visual inspection tasks of underwater structures and autonomous navigation missions with seabed mapping, demonstrating the vehicle's ability to perform its intended inspection and mapping tasks in real-world conditions.

This progression from controlled to operational environments enabled systematic validation of all vehicle subsystems while ensuring safe and reliable testing procedures. A video presenting the vehicle capabilities while performing these tests can be found in the following link: https://www.youtube.com/watch?v=SzGtbimGajI.

3.4.1 Buoyancy and kinematics validation

The first set of aquatic tests were conducted at the ATLANTIS test centre in Viana do Castelo [174]. These tests were designed to determine the amount and placement of lead sinkers needed to achieve a slightly positive buoyancy and alignment of the CoM and CoB. As well as test the structural soundness of the AUV and its kinematic control. Figure 3.17 shows an image of Raya being lowered onto the water.

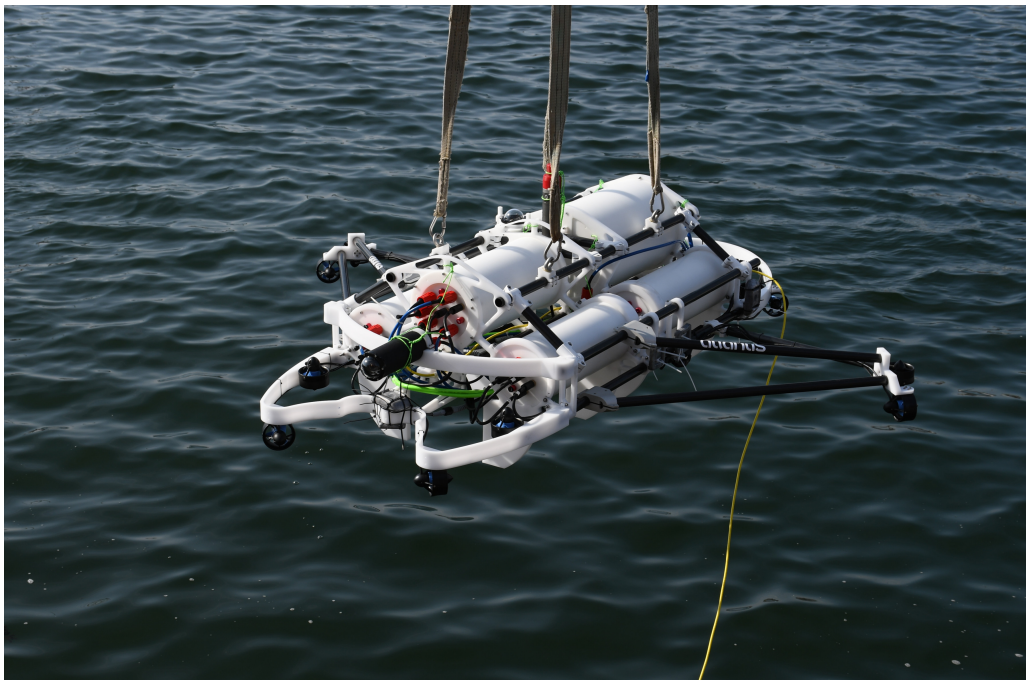

Figure 3.17: RAYA AUV open frame design during system trials.

During this test, the vehicle was suspended for an extended duration using its four lifting eye bolts, and throughout this period, the structure remained structurally sound, exhibiting no significant displacements. To optimize weight distribution, lead sinkers were strategically positioned in various locations on the vehicle. This arrangement ensured that the vehicle maintained a horizontal orientation in the absence of thrust and remained positively buoyant while minimizing the upward force. In total, 10 kg of lead sinkers were distributed across different areas of the vehicle.

To determine the actual weight of the vehicle, a lifting crane and a dynamometer were utilized, connected to the four lifting eye bolts (refer to figure 3.17). This test revealed a weight of 162.75 kg, excluding the manipulator, which weighed 9.5 kg. Consequently, the weight attributed to the cables and fasteners can be calculated as follows:

- Experimental weight (excluding lead sinkers and manipulator): 162.75 kg;
- Theoretical weight (excluding lead sinkers and manipulator): 144.53 kg;
- Weight of cables and fasteners: 18.22 kg.

Due to these anticipated variations and uncertainties regarding the actual CoM and CoB, the process of balancing the vehicle was achieved through a trial-and-error approach.

Next, the RAYA AUV was subjected to kinematic validation tests at the Atlantis test center. These tests, conducted without the manipulator, allowed to verify the correctness of the thruster configuration and to validate the accuracy of the kinematic expressions used in the vehicle's control algorithms. The thrusters' power was deliberately reduced to 20% to conserve battery power and ensure the safety of the vehicle during testing. Controlled inputs were applied to the AUV using

a remote controller. These inputs, represented on a scale from 0 to 1, were then converted to control forces ($\boldsymbol{\tau}$). This control force vector is used through equation 3.8 to calculate the force of each thruster. The distance of each thruster to the center of mass is presented in table 3.4. This approach facilitated the assessment of the vehicle's response to known commands and provided a direct comparison between the commanded inputs and the measured velocities.

Table 3.4: Distance in x, y and z of each thruster to the center of mass.

Thruster ID	**Name**	l_x	l_y	l_z
1	**FRV**	0.859	-0.32	-0.11
2	**FRH**	1.103	-0.293	-0.209
3	**FLH**	1.103	0.297	-0.209
4	**FLV**	0.859	0.324	-0.11
5	**MLV**	-0.311	1.108	-0.11
6	**MLH**	-0.151	1.101	-0.209
7	**BLV**	-0.724	0.323	-0.096
8	**BLH**	-0.864	0.382	-0.209
9	**BRH**	-0.864	-0.378	-0.209
10	**BRV**	-0.724	-0.319	-0.096
11	**MRV**	-0.311	-1.104	-0.11
12	**MRH**	-0.151	-1.097	-0.209

The validation process involved three standing start to constant speed experiments, comparing the input commands against the linear and angular velocities measured by the DVL and the IMU. The first experiment aimed to evaluate the movement of the vehicle when actuated with a linear command in the x_B axis. Figure 3.18 illustrates the relationship between the input commands and the linear velocities recorded by the DVL. Figure 3.18a shows the linear commands along the x_B, y_B and z_B axes, while figure 3.18b presents the measured velocities in meters per second. As shown, the linear command in the x_B direction (blue line) demonstrates a significant step input, which is accurately tracked by the measured velocity. The y_B and z_B components remain close to zero, indicating minimal lateral and vertical movements, consistent with the input commands.

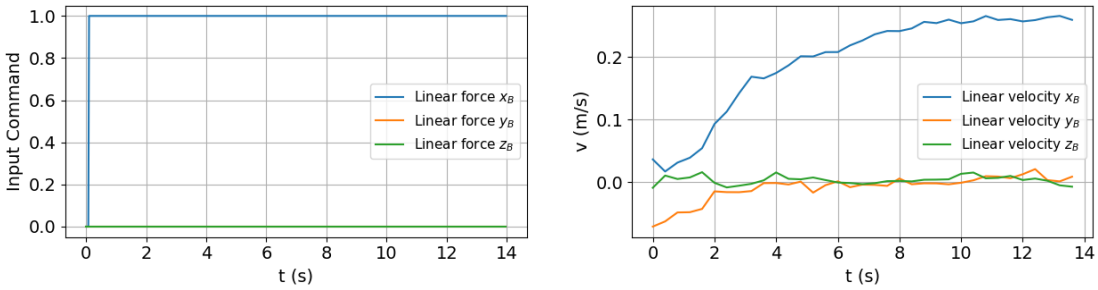

(a) Input commands from the remote controller.

(b) Linear velocities retrieved from the DVL sensor.

Figure 3.18: Standing start to constant speed using linear command. Blue, orange and green lines represent the velocities in x_B, y_B and z_B axes

.

The second test aimed to study the vehicle's response to an angular input around the z_B axis, figure 3.19a. The DVL and IMU were used to measure the linear and angular velocities, respectively. Figure 3.19b shows that the DVL accurately tracked the motion of the vehicle along the y_B axis. This occurs because the DVL is located near the back of the vehicle, closely aligned with the CoG x axis. Additionally, when an angular command was applied around the z_B axis, the IMU measurement indicated angular movement in the z_B direction, as depicted in figure 3.19c. As a result, angular rotation around the z_B axis translates into a linear velocity component in the y_B direction at the DVL's position.

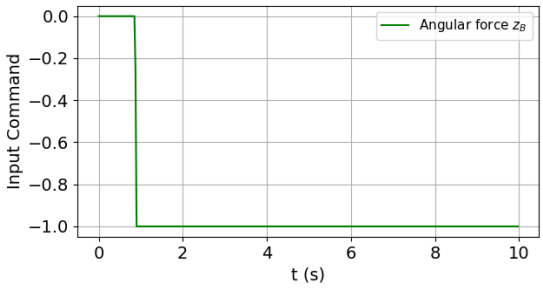

(a) Input command from the remote controller.

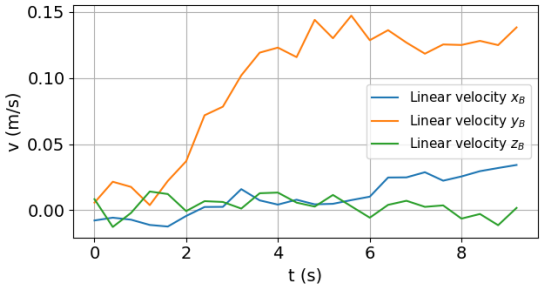

(b) Linear velocities retrieved from the DVL sensor.

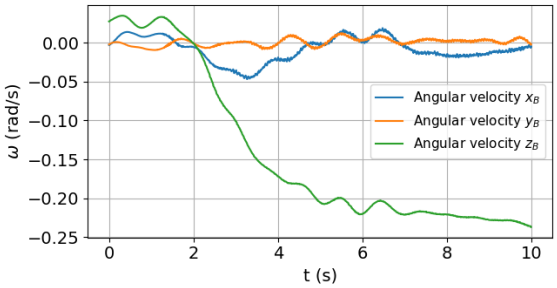

(c) Angular velocities retrieved from the IMU sensor.

Figure 3.19: Standing start to constant speed using angular command. Blue, orange and green lines depict the velocities in x_B, y_B and z_B axes, respectively.

The third and final experiment aimed to evaluate the vehicle's response to an angular input command in y_B axis, shown in Fig. 3.20a. As expected, since the thruster power was reduced to 20%, when an angular input command was applied along the y_B axis, the vehicle's motion was limited. Fig. 3.20b shows the measured angular velocity of the vehicle with the IMU. The results show that the angular velocity increased and then decreased to zero as equilibrium was reached. The vehicle could only move until the force generated by the thrusters equaled the moment caused by the misalignment between the CoM and CoB. Additionally, it is possible to observe that the decay to zero angular speed is slower (close to 5 seconds) than the initial acceleration (3 seconds) due to the large drag of the vehicle.

The results from these tests confirm that the thruster configuration of the RAYA AUV is correctly implemented and that the kinematic expressions used in the vehicle's control algorithms are accurate. The close alignment between measured velocities, both linear and angular, and the

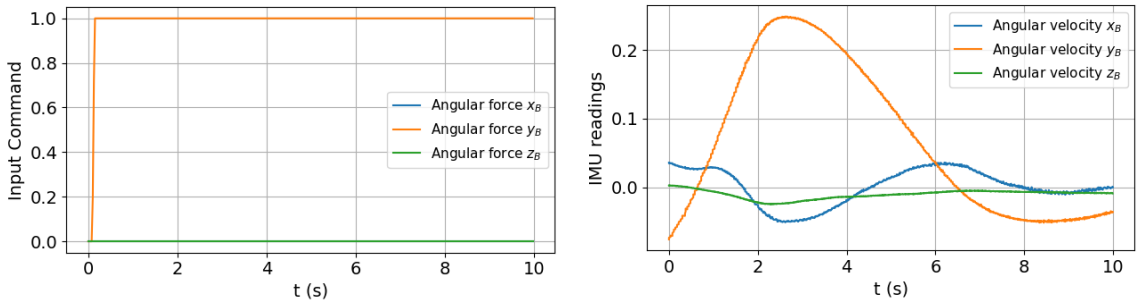

(a) Input commands from the remote controller.

(b) Angular velocities retrieved from IMU sensor.

Figure 3.20: Standing start to constant speed using angular command in y_B axis. Blue, orange and green lines represent the velocities in x_B, y_B and z_B axes.

expected results using the parameters estimated by Leitão [167], demonstrates the reliability of the AUV's kinematic model. These findings are crucial to ensure the precise control of the AUV during autonomous missions, which is essential for accurate navigation and maneuvering. The successful validation of the kinematics in a controlled test environment lays the groundwork for further testing and deployment in more complex and dynamic underwater settings.

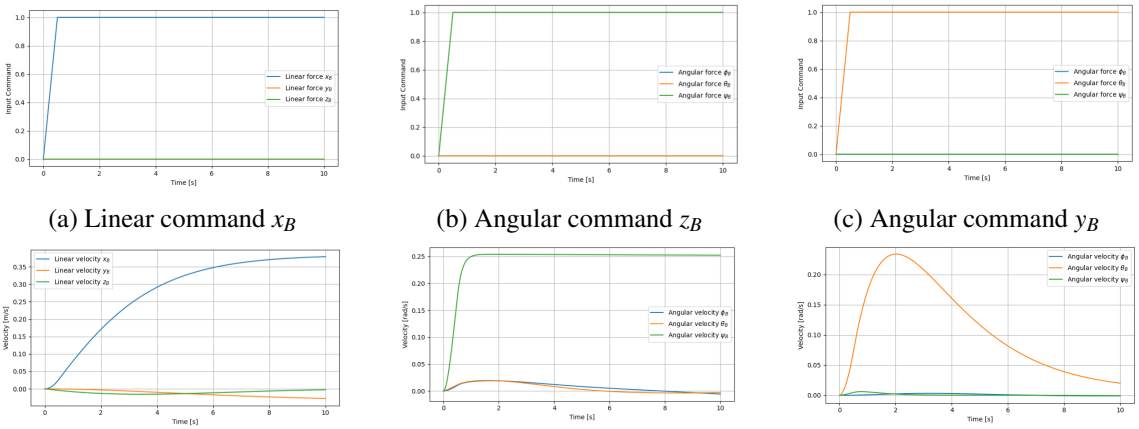

(a) Linear command x_B

(b) Angular command z_B

(c) Angular command y_B

(d) Linear velocity x_B

(e) Angular velocity z_B

(f) Angular velocity y_B

Figure 3.21: AUV simulation results: Input commands (top row) and corresponding output velocities (bottom row) for linear and angular motions along x_B, y_B, and z_B axes.

3.4.2 Perception module accuracy assessment

The second set of tests were conducted at the Centre of Robotics and Autonomous Systems (CRAS) laboratory's indoor pool, by performing a reconstruction task of the pool's walls and floor to validate the perception system and its capabilities. The pool has a depth of 1.70 m, and it measures 4.573 m and 4.397 m in length and width, respectively. A teleoperated mission was performed to gather data by several sensors, allowing the acquisition of navigation information through the Nortek DVL 300 and KVH 1750 IMU from the localization module. The vehicle's

6 DoF localization was estimated by fusing linear velocity data from the DVL and angular velocity from the IMU using an EKF, as explained in section 3.3.1. This fusion process enabled the concatenation of data from both the Imagenex 831l sonar and the M3 multibeam sonar over time. Due to their specific positioning in the vehicle, the Imagenex 831l sonar was used to gather high-resolution 3D information about the walls of the pool, while the M3 sonar was employed to obtain 3D data of the pool's floor.

Post-processing involved segmenting each wall and the floor individually. To validate data quality, a RANSAC robust estimator was iteratively applied to segment each wall and floor. The plane coefficients obtained for each wall were used to calculate the average distance and standard deviation. Figure 3.22 depicts the resultant 3D reconstruction. From the representation, all four segmented walls (red, blue, green, and pink) and the bottom of the pool (yellow) are clearly visible. Table 3.5 presents the average distance and standard deviation from each wall to their respective parallel coordinate plane with the coordinate system origin initialized at 1.19 m depth from the water surface. The red and green walls' distances are measured from the vertical center plane aligned with the x_N axis, while the blue and pink walls' distances are measured from the vertical center plane aligned with the y_N axis. The yellow floor's distance is measured downwards from the xy-plane to the pool bottom.

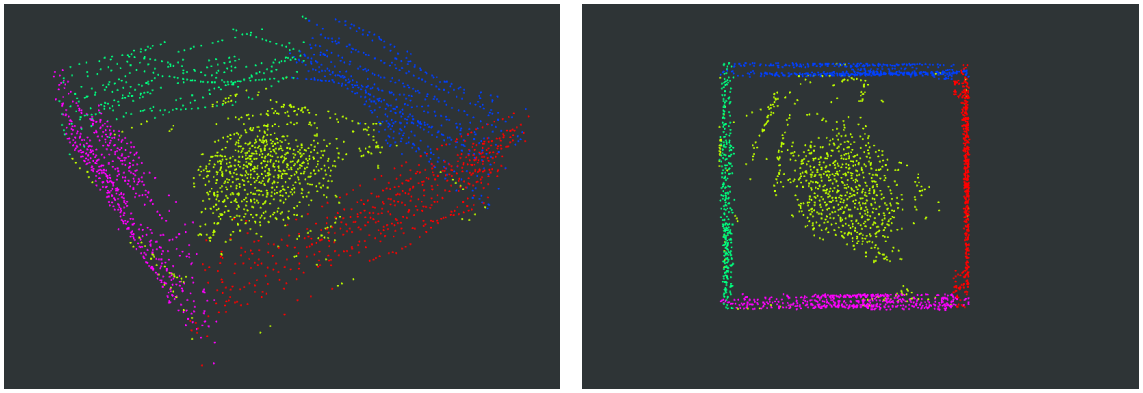

(a) Perspective view. (b) Top-down view.

Figure 3.22: 3D reconstruction of CRAS' indoor pool: all four segmented walls (red, blue, green and pink) and the bottom of the pool (yellow).

Table 3.5: Pool reconstruction data.

	Distance to parallel coordinate plane	
Wall	**Average (m)**	**Standard deviation (m)**
Red	2.381	0.067
Green	-2.154	0.060
Blue	2.130	0.081
Pink	-2.260	0.087
Yellow	0.533	0.063

The estimated length, width, and depth of the pool have errors of 0.81%, 0.18% and 1.36%,

respectively. The perception system shows good results, and the observed inaccuracies can be attributed to the noise from each sonar sensor, combined with drift in the localization algorithm.

3.4.3 Real environment missions

A third set of tests was conducted at Porto de Leixões during a real scenario application. First, RAYA was first remotely operated to approach and visually inspect a buoy at different depths, while also obtaining 2D information of the structure. Next, an autonomous mission was executed with the vehicle closer to the shore with the objective of testing the autonomous capability of the AUV. These two field tests were performed on the biggest port for yachting on the North of Portugal, namely the Marina de Leça harbor. It has multiple mooring places available on site and has a depth of 4 m at the entry basin and 1.5-3.5 m at the yacht basin.

The first test allowed for the validation of the close-range visual inspection capacities in the field. This mission was executed in the maneuverable zone of the harbour with Douglas Sea State 1 and maximum underwater currents of 0.1 m/s. The goal was to retrieve 2D information with the frontal RGB camera along the height of the structure. Figure 3.23 shows three images obtained

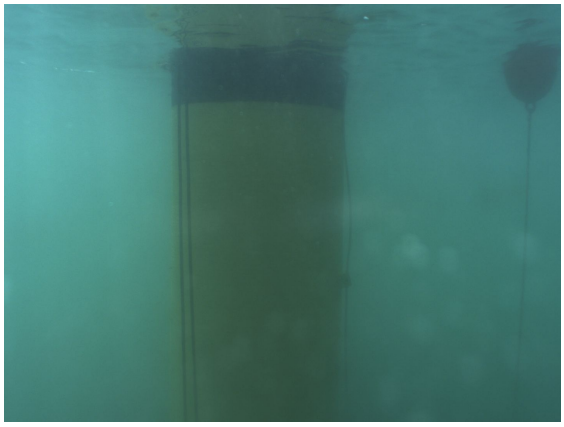

(a) Buoy at the surface.

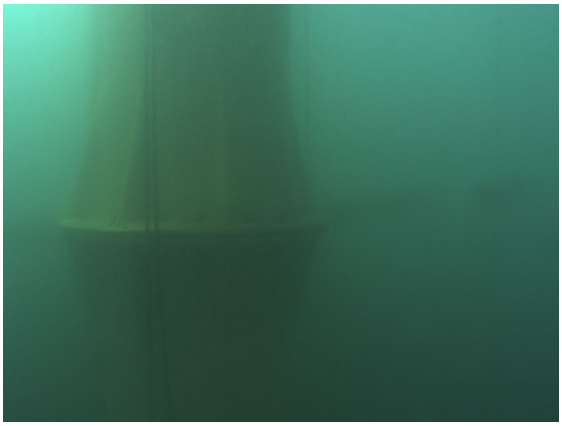

(b) Buoy at 2 meters depth.

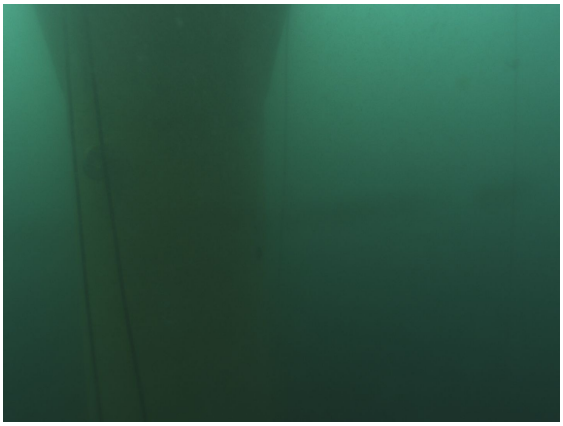

(c) Buoy at 5 meters depth.

Figure 3.23: Visual camera positioned at the front of the vehicle inspecting a buoy at different depths in Porto de Leixões.

from the front camera at different depths while inspecting a buoy at Porto de Leixões. For this mission, the vehicle was remotely operated and kept at a distance of approximately 2 meters from the buoy.

Next, an autonomous mission was executed with RAYA at the yacht basin with Douglas Sea State 0 and underwater currents close to 0 m/s. Three coordinates were user specified at the surface of the water. This second mission was performed to test the autonomous capability of the AUV. To achieve this goal, the vehicle started at an initial position (0,0) m and navigated to (3,0) m and finally (0,3) m, returning to the initial point as final destination (all coordinates relative to the local frame positioned at the initial point). The navigation algorithm, presented in algorithm 1, follows a state machine approach [175]. At the initial state, the AUV checks if its distance to the goal is within a user-defined maximum Euclidean distance ($\|\Delta(x,y)\|_2$). If the distance exceeds this limit, the AUV enters a rotation stage, aligning itself towards the goal. The rotation stops when the orientation error $|\Delta\psi|$ is below a user-defined threshold. The AUV then waits for a specified time or until the orientation error is half of the user-defined threshold before starting to move. In the next state, the AUV moves at maximum linear velocity, with angular velocity controlled proportionally to the orientation error. Finally, as the AUV approaches the goal, it reduces its linear velocity and adjusts angular velocity proportionally to $|\Delta\psi|$, ensuring precise positioning.

Algorithm 1 Pseudo code of the continuous execution routine used for the autonomous mission.

```
state = Init
t = 0s
while true do
    switch state do
        case Init
            if ||Δ(x,y)||_2 < D_finish then
                state = MoveEnd
            else
                state = Rotate
            end if
        case Rotate
            v = 0
            w = sgn(Δψ) · max(w_min, |Δψ| · w_max/π)
            if |Δψ| < EPS_yaw then
                state = RotateEnd
            end if
        case RotateEnd
            v = 0
            w = 0
            if t > 3s OR |Δψ| < EPS_yaw/2 then
                state = MoveCruise
            end if
        case MoveCruse
            v = v_max
            w = k1 · Δψ · w_max/π
            if ||Δ(x,y)||_2 < D_finish then
                state = MoveEnd
            end if
        case MoveEnd
            v = v_min
            w = k2 · Δψ · w_min/π
            if t > 30s OR ||Δ(x,y)||_2 > D_finish + 1.5 m then
                state = Rotate
            else if ||Δ(x,y)||_2 < EPS_position then
                state = End
            end if
end while
```

Seabed 3D information was retrieved from the multibeam sonar while performing the navigation task. Figure 3.24 shows two images (top-down and perspective views) representing the autonomous trajectory executed (in red) and the seabed reconstruction task that took place at Porto de Leixões. Results show that the performed trajectory, presented in figure 3.24b, was similar to the expected triangular shape, while showing some deviation in depth (see figure 3.24a) meaning that a fine-tuning is still needed for the navigation algorithm. This figure also shows a depth map, result of the concatenated sonar point cloud data gathered with M3 sonar. The depth varies between 1.71 and 2.58 meters, and it is consistent with the depth information of the local test site.

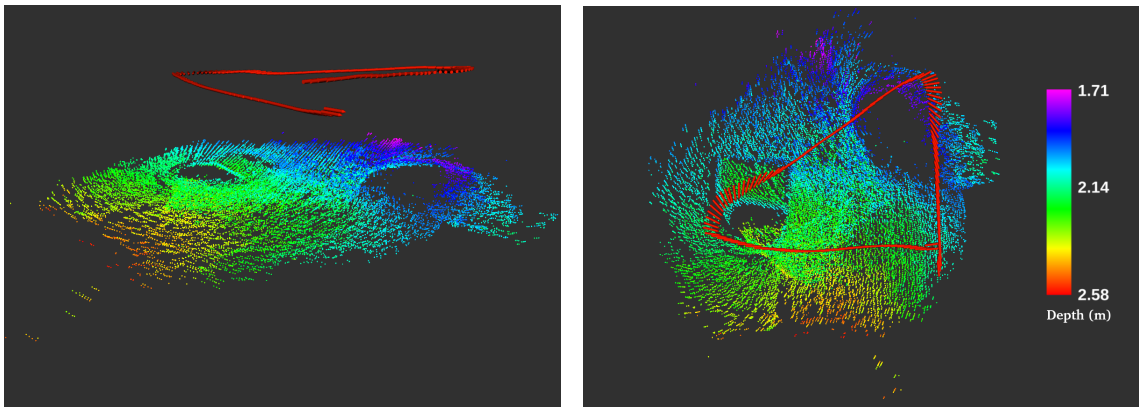

(a) Perspective view. (b) Top-down view.

Figure 3.24: Seabed reconstruction task conducted at Porto de Leixões. The vehicle preformed an autonomous trajectory in the shape of a triangle, given by three points. The red arrows represent the odometry and the point cloud represents the results of the seabed mapping. The depth map is identified by the colour bar, with red being the lowest registered depth at 1.71 m and purple the highest at 2.58 m.

3.5 Final Considerations

This chapter deals with the system and structural development of the RAYA AUV for offshore inspection and maintenance missions. The structural performance was experimentally validated at the ATLANTIS test centre. The vehicle was also optimized with lead sinkers to adjust the CoM and CoB, achieving the alignment of the centres, and a slightly positive buoyancy. By analyzing the necessary forces for each thruster across four different scenarios, including operational conditions with and without a 5 kg payload, the suitability of the thruster's placement has been verified. The resulting forces for each thruster were calculated for various vehicle and manipulator configurations to validate all possible motion ranges. The overall hardware architecture of RAYA consists of five different modules, with four main functions: navigation, perception, propulsion and power system. By making use of the modular implementation of this architecture, all of RAYA's systems were independently tested: the kinematic control system demonstrated accurate 6 DoF actuation necessary for intervention tasks; the perception system achieved high accuracy with reconstruction errors below 1.5% in controlled environments; and real-world trials confirmed autonomous navigation capabilities including seabed mapping and visual inspection of underwater structures. A summary of the specifications of the final RAYA is presented in table 3.6.

Overall, this work details the development phase of the RAYA AUV, showcasing the decision making process behind the sensor and actuator selection, as well as the techniques used during the design phase, which allowed to achieve all the previously set requirements. The conducted experiments validated the vehicle's structural integrity, kinematic control, perception accuracy, and autonomous navigation capabilities. Through its bio-inspired design, modular architecture, and comprehensive sensor integration, RAYA represents a significant step toward enabling persistent autonomous operations in offshore environments.

Table 3.6: RAYA specifications.

Configuration	Hybrid (AUV & ROV)
Length [m]	2.3
Width [m]	2.25
Height [m]	0.79
Weight [kg]	162.75
Apparent weight [kg]	4
Max operating depth [m]	150
Energy [kWh]	3.4 kWh Li-Ion battery
Autonomy [h]	5
Operating temperature [°C]	0 - 30
Tether size [m]	300
Tether bandwidth [Mbps]	100
Degrees of freedom	6
Number of thrusters	12
Max linear velocity [m.s^{-1}]	Surge: 1.3 Sway: 0.7 Heave: 0.7
Max angular velocity [rad.s^{-1}]	Roll: 0.087 Pitch: 0.087 Yaw: 0.175
Navigation system	IMU DVL GPS
Perception system	Multibeam sonar Pipe profiler sonar Visual cameras + LED lightning
Launch and recovery	Crane

Chapter 4

3D Exploration of Underwater Structures using a Multibeam Sonar

The ability to create accurate three-dimensional representations of underwater structures represents a critical capability for enabling persistent autonomous operations. In offshore environments, where high-value infrastructure operates continuously underwater, these models serve as the foundation for autonomous navigation, inspection, and intervention tasks. Accurate representations of underwater structures, such as docking stations and their supporting infrastructure, are especially crucial for enabling long-term autonomous operations through manipulation-based docking capabilities. While current AUVs can execute pre-planned survey missions effectively, they struggle with tasks requiring adaptive exploration and precise environmental understanding. A particular challenge lies in close-range operations where vehicles must maintain optimal sensing distances while ensuring safe navigation near structures. Traditional approaches often rely on maintaining fixed standoff distances or following predefined patterns, which can result in incomplete coverage, suboptimal data quality, or potentially unsafe vehicle positions. Moreover, the quality of sonar data varies significantly with acquisition angle and distance. Addressing these challenges requires new methodologies that can explore unknown environments while optimizing both data quality and vehicle safety.

This chapter is organized as follows: Section 4.2 presents each C2FARUS stage, offering insights into the underlying principles and computational techniques. Section 4.3 discuss an extensive analysis of the C2FARUS' performance detailing experiments in both simulation and real scenarios. Finally, section 4.4 clarifies the most important conclusions of this research, providing a critical view of the obtained results.

4.1 Introduction

Despite recent advances in autonomous underwater vehicles that have enhanced our ability to navigate and interact with subsea environments, close-range operations near structures remain challenging due to sensing limitations. While optical systems can provide high-resolution data

for monitoring and inspection tasks [106, 176], their effectiveness is constrained by water clarity and limited range due to light attenuation [177, 105]. Acoustic sensing through sonars offers a more robust solution for underwater perception [178, 179], yet there remains a significant gap in navigation techniques that can ensure both performance and safety during close-range operations and maintenance tasks [134].

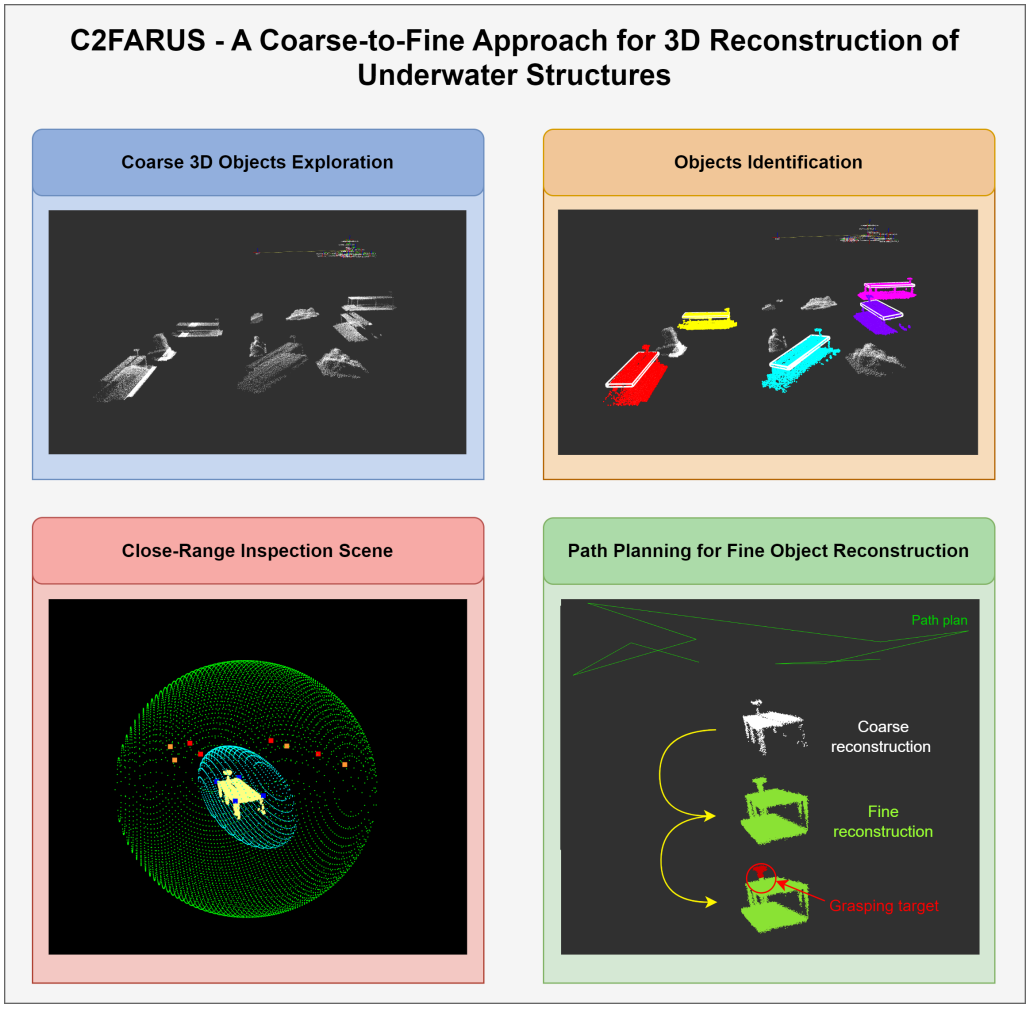

Figure 4.1: C2FARUS - a coarse-to-fine approach for 3D reconstruction of underwater structures.

The research presented along this chapter aims to enable autonomous underwater vehicles to explore the underwater environment and capture a fine 3D reconstruction of underwater structures using 3D sonar information. A novel coarse-to-fine approach designed for underwater exploration, detection, recognition, and 3D reconstruction of submerged structures, provides the environmental understanding necessary for manipulation-based docking maneuvers [155, 180]. The proposed method, shown in figure 4.1, encompasses a series of interconnected stages designed to address the challenges inherent in underwater exploration and inspection tasks. Starting with no prior knowledge of the environment, it enables the AUV to autonomously explore and detect objects of interest using sonar sensors. By leveraging a multibeam sonar, the system performs an initial

coarse scan to identify key features and approximate the target object's location. The method emphasizes close-range inspection navigation, which is critical for acquiring high-resolution data. Once detected, the vehicle transitions into a fine inspection phase, where it navigates within a safe inspection scene representation around the object. This proximity ensures the sonar captures detailed, high-resolution information from multiple perspectives, minimizing blind spots and enhancing 3D reconstruction accuracy. The final output is a fine and comprehensive 3D model of the underwater structure, generated by combining the data from multiple close-range views.

4.2 C2FARUS - A Coarse-to-Fine Approach for 3D Reconstruction of Underwater Structures

C2FARUS introduces a coarse-to-fine approach designed to tackle the challenges of underwater exploration and object reconstruction in unknown environments. Beginning with no prior information about the surroundings, the method gradually refines its understanding of the environment through a series of stages, depicted in figure 4.2. This structured approach ensures that initial uncertainties are systematically reduced, allowing for precise and comprehensive perception of underwater structures even in complex and uncharted settings. It employs close-range navigation in a new inspection scene representation, to overcome the limitations of sonar resolution at greater distances, ensuring high-quality data acquisition. By navigating in proximity to the target, the system captures detailed, high-resolution data using a multibeam sonar. This data is then utilized for a final fine 3D reconstruction, allowing for a comprehensive and accurate understanding of underwater structures.

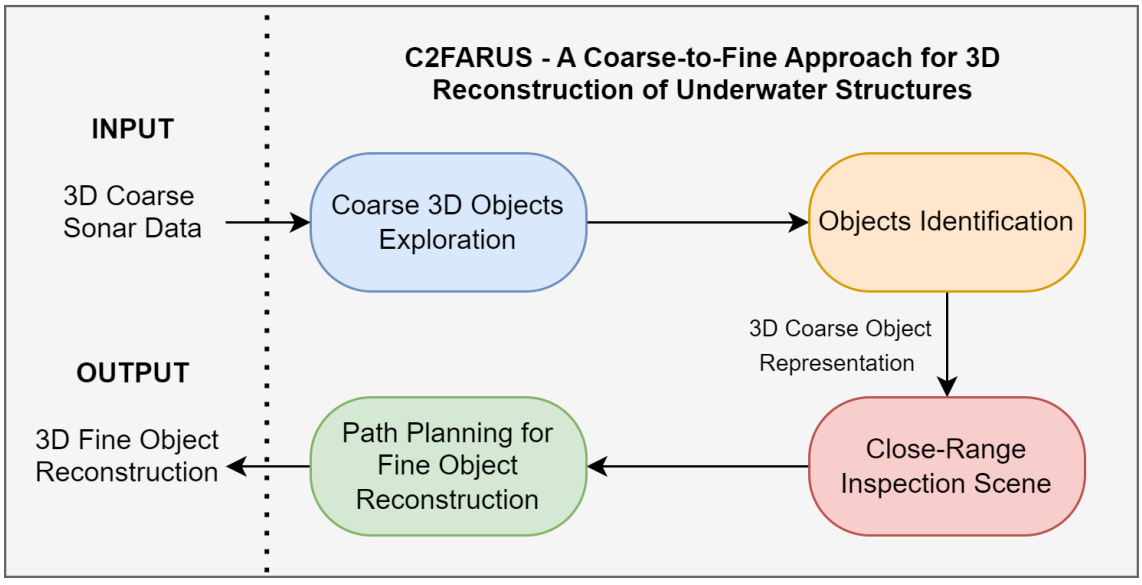

Figure 4.2: Visual representation of C2FARUS methodology, a coarse-to-fine approach for 3D reconstruction of underwater structures.

4.2.1 Coarse 3D Objects Exploration

C2FARUS initial stage, depicted in figure 4.3, focuses on exploring an unknown space of the seabed to obtain a coarse location of points of interest. This could include rocks, debris, wreckage, docks or other objects that may pose potential exploratory interest.

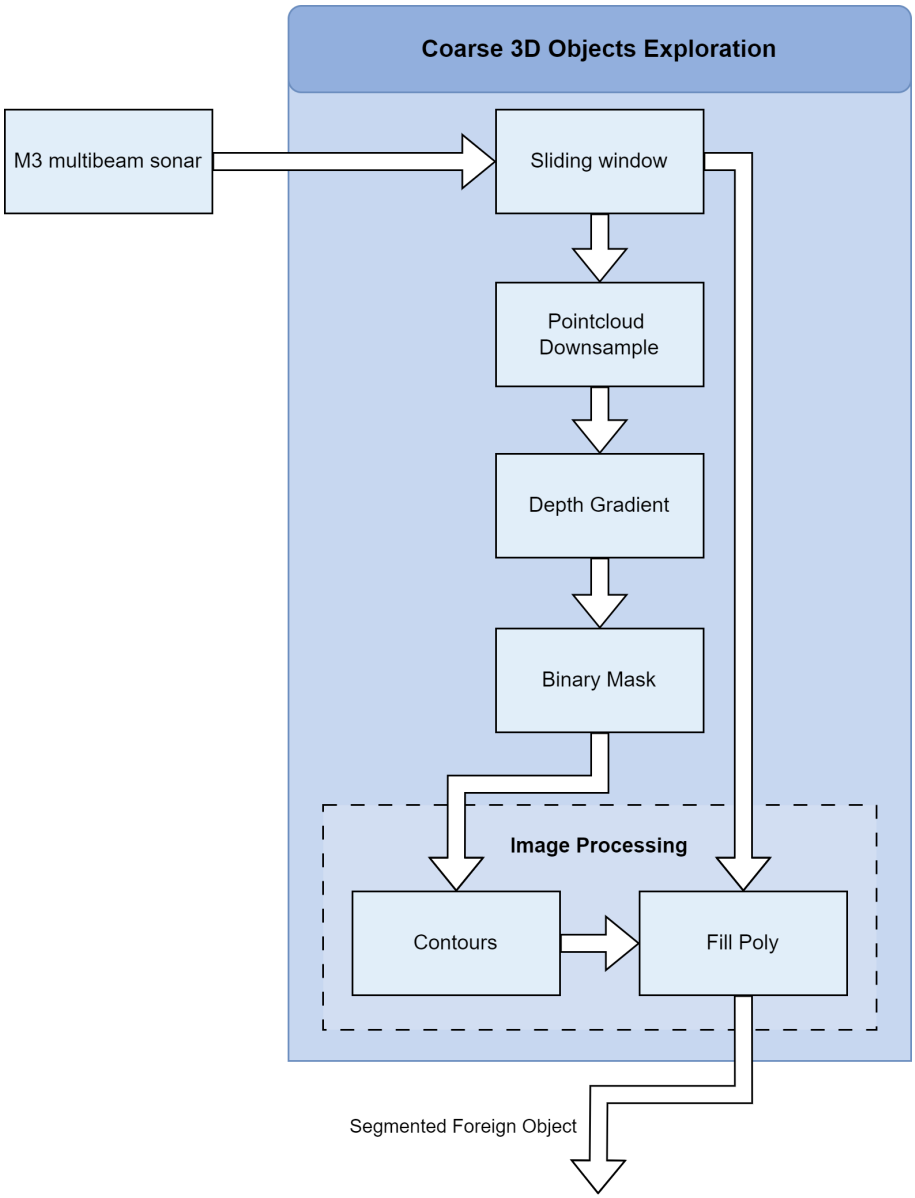

Figure 4.3: Coarse 3D objects exploration stage.

Multibeam sonar technology is used to capture detailed 3D data of the seabed terrain. The collected data is organized into a sliding window data structure, enabling efficient processing and analysis of localized regions within the sonar data. To facilitate efficient processing, the point cloud data is transformed from its native 3D representation into a 2D grid structure by projecting points onto the XY-plane, where each cell contains the mean depth value of its corresponding region. This averaging process inherently acts as a low-pass filter, reducing high-frequency noise

from the multibeam sonar while preserving essential terrain characteristics. The resulting grid-based representation provides a structured format for gradient analysis.

To detect potential points of interest and differentiate their boundaries from the seabed, depth gradient analyses are performed on the grid-based representation. The depth gradient represents the first order derivative of depth values between neighboring cells in the grid. Areas with high depth gradient values indicate significant changes in depth that therefore suggest boundary points of interest. This crucial step is pivotal in identifying regions of significant depth variation which indicate potential object boundaries or features of interest. To enhance the accuracy and effectiveness of the analysis, derivatives are calculated in two orthogonal directions. To capture the nuanced variations in depth along orthogonal axes, two distinct kernels serve as localized convolution filters, tailored for analysis along the xx and yy axes. The use of dual kernels for depth gradient analysis offers several advantages. By considering depth variations along orthogonal axes, a broader spectrum of spatial information is captured, enabling the detection of objects with diverse geometric characteristics. The grid space representation enhances the resilience of the analysis to object spatial orientation variations within the seabed environment.

A binary image is generated with all the cells exhibiting high depth gradient values being highlighted. To achieve a complete segmentation mask, each object contour is detected and filled in the image. A 3D coarse representation of each object can be obtained using the final segmentation mask and the original multibeam collected data.

4.2.2 Objects Identification

The goal of this second stage, illustrated in figure 4.4, is to identify and classify previously known models within the segmented 3D coarse points of interest from the previous stage, while estimating their positioning and orientation. This will allow to filter undesired segmented objects, such as rocks, from the previous stage and proceed with the fine reconstruction task under objects of interest.

Initially, the segmented points of interest obtained from the previous stage are filtered to remove points that belong to the seabed plane. A RANSAC algorithm is used to estimate the seabed plane that is parallel to the xy-plane. Removing these points isolates the object's structural components, enhancing the accuracy of subsequent analyses.

A bounding box encapsulating the segmented points of interest is computed, applying Principal Component Analysis (PCA) to the point cloud and estimating the eigen values, providing a spatial framework for subsequent feature extraction and recognition processes. The bounding box serves as a reference for delineating the extent of the object within the scene, facilitating geometric feature analysis. Given a point cloud with N points, where each point is defined as $\mathbf{p}_i = [x_i, y_i, z_i]^T$, the covariance matrix $\mathbf{C} \in \mathbb{R}^{3\times3}$ is computed as shown in equation 4.1:

$$\mathbf{C} = \frac{1}{N}\sum_{i=1}^{N}(\mathbf{p}_i - \bar{\mathbf{p}})(\mathbf{p}_i - \bar{\mathbf{p}})^T \tag{4.1}$$

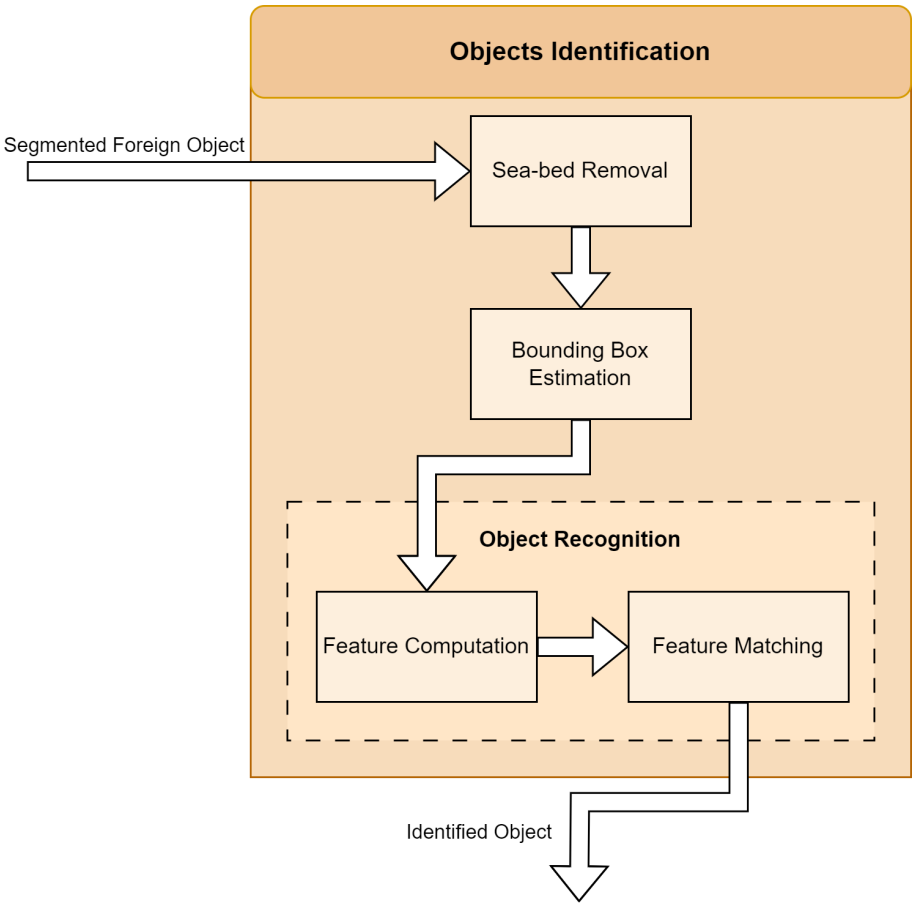

Figure 4.4: Objects identification stage.

where $\bar{\mathbf{p}}$ represents the centroid of the point cloud. Principal Component Analysis decomposes this covariance matrix into eigenvectors $\mathbf{V} = [\mathbf{v}_1, \mathbf{v}_2, \mathbf{v}_3]$ and corresponding eigenvalues $\lambda_1 \geq \lambda_2 \geq \lambda_3$, where the eigenvectors represent the principal axes of the bounding box. These eigenvectors form an orthogonal basis that defines the orientation of the object-aligned coordinate system.

The bounding box dimensions are then determined by projecting all points onto each principal axis and finding the minimum and maximum extents, as shown in equation 4.2:

$$d_j = \max_{i=1,\ldots,N} (\mathbf{v}_j^T \mathbf{p}_i) - \min_{i=1,\ldots,N} (\mathbf{v}_j^T \mathbf{p}_i), \quad j = 1,2,3 \tag{4.2}$$

where d_j represents the extent of the bounding box along the j-th principal axis. The resulting oriented bounding box is defined by its center position $\bar{\mathbf{p}}$, orientation matrix $\mathbf{V}$, and dimensions $[d_1, d_2, d_3]$.

Geometric features pertinent to the object's structural characteristics are extracted from the bounding box and the segmented object. These features encompass properties such as shape, dimensions, curvature, and spatial relationships among constituent points. For docking station identification, a Plane RANSAC algorithm detects the planar surface within the segmented object. Corner points belonging to the detected plane are then extracted as key features. These points,

combined with structural measurements such as the length-to-width ratio, form the geometric signature used for object recognition.

The geometric method approach to object detection and recognition leverages inherent structural properties to infer object identity and spatial orientation. This approach offers computational efficiency, robustness to environmental variability, and interpretability of results [181].

4.2.3 Close-Range Inspection Scene Representation

The quality of sonar data is fundamentally tied to the acquisition distance - operating too far from structures results in poor resolution while moving too close introduces collision risks. This stage of C2FARUS addresses this challenge by defining optimal inspection zones that balance data quality with vehicle safety. The approach creates a structured representation of the inspection scene where the vehicle can navigate safely while maintaining the sonar resolution required for detailed reconstruction.

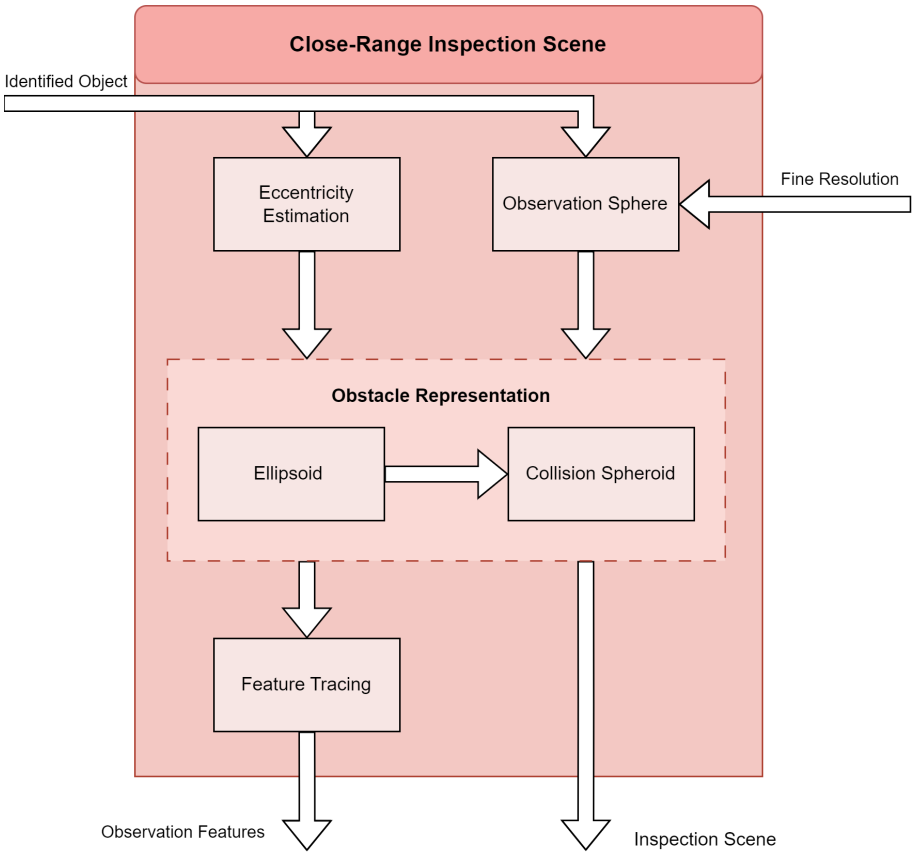

Figure 4.5: Close-range inspection scene stage.

The inspection scene representation, illustrated in figure 4.5, consists of three key elements: a maximum observation boundary, a collision-free zone, and a set of observation points. The maximum observation boundary ensures adequate sonar resolution by limiting the acquisition distance based on sensor specifications. The collision-free zone accounts for the object's geometry

and the vehicle's dimensions to prevent unsafe approaches. The observation points are positioned to capture all critical object regions while maintaining the required resolution and safety margins.

To construct this representation, the process follows several steps. First, a spherical boundary is computed using the multibeam sonar specifications. The radius of this sphere (r) is determined by equation 4.3,

$$r = \frac{R_f}{2 \cdot tan(\frac{b_{fov}}{2})}, \tag{4.3}$$

where r is the radius of the sphere that guarantees adequate coverage and resolution, R_f is the minimum resolution expected fot the fine 3D reconstruction task and b_{fov} is the multibeam's field of view (FOV).

The collision-free zone is defined by transforming the initial spherical boundary into an ellipsoid that respects the object's proportions. Given a sphere of radius r and an object with dimensions length l, width w, and depth d, the ellipsoid's semi-axes are computed (equation 4.4) based on the object's relative proportions:

$$a = \frac{l}{s_{max}} r, \quad b = \frac{w}{s_{max}} r, \quad c = \frac{d}{s_{max}} r \tag{4.4}$$

where $s_{max} = \max(l, w, d)$ is the object's largest dimension. The resulting ellipsoid can be represented in quadratic form as shown in equation 4.5 and 4.6:

$$\mathbf{x}^T \mathbf{A} \mathbf{x} = 1, \tag{4.5}$$

$$\mathbf{A} = \begin{bmatrix} \frac{1}{a^2} & 0 & 0 \\ 0 & \frac{1}{b^2} & 0 \\ 0 & 0 & \frac{1}{c^2} \end{bmatrix}, \tag{4.6}$$

where $\mathbf{x} = [x, y, z]^T$ and $\mathbf{A}$ is a symmetric positive definite matrix:

To align the ellipsoid with the object's orientation, a rotation transformation is applied. Given a rotation matrix $\mathbf{R}$, calculated from the previous PCA, the rotated ellipsoid is described by equation 4.7:

$$\mathbf{x}^T \mathbf{R}^T \mathbf{A} \mathbf{R} \mathbf{x} = 1 \tag{4.7}$$

The resulting ellipsoid provides a collision-free zone that adapts to the object's geometry while maintaining the minimum required distance for sonar data acquisition.

Finally, observation points (p_o) are determined for each object point identified in the previous stage through a two-step projection process. First, each object point is projected onto the closest ellipsoid point using the line passing both points. This ensures the selection of observation points outside the high-risk collision zone while maintaining minimal distance to optimize sonar data resolution. The second step involves offsetting these initial projections outward by the vehicle's size

(v_s) along the same projection line, resulting in the final observation points (p_o) that lie between the ellipsoid and spherical boundary. This dual-projection approach guarantees both collision-free positioning and high resolution sonar data acquisition conditions, as the final observation points maintain safe distances from the object while remaining within the maximum observation boundary defined by the sonar's specifications.

4.2.4 Path Planning for Fine Object Reconstruction

The final stage of C2FARUS focuses on generating an efficient inspection path for fine object reconstruction using the observable points and the inspection scene calculated in the previous stage. As illustrated in figure 4.6, the path planning process takes the observable points as input and produces a complete inspection trajectory through a series of optimization steps. The inspection path comprises two distinct components: precise inspection scans and transitional paths. A precise inspection scan involves the vehicle traversing a line between an anchor point and its corresponding observable point while executing a controlled pitch rotation. The transitional path connects an observation point to the subsequent anchor point in the sequence. Anchor points, which serve as the starting positions for precise inspection scans, are determined by calculating the intersection between the boundary sphere and the projection line established in the previous stage (the line that crosses an observable point and its closest point on the ellipsoid).

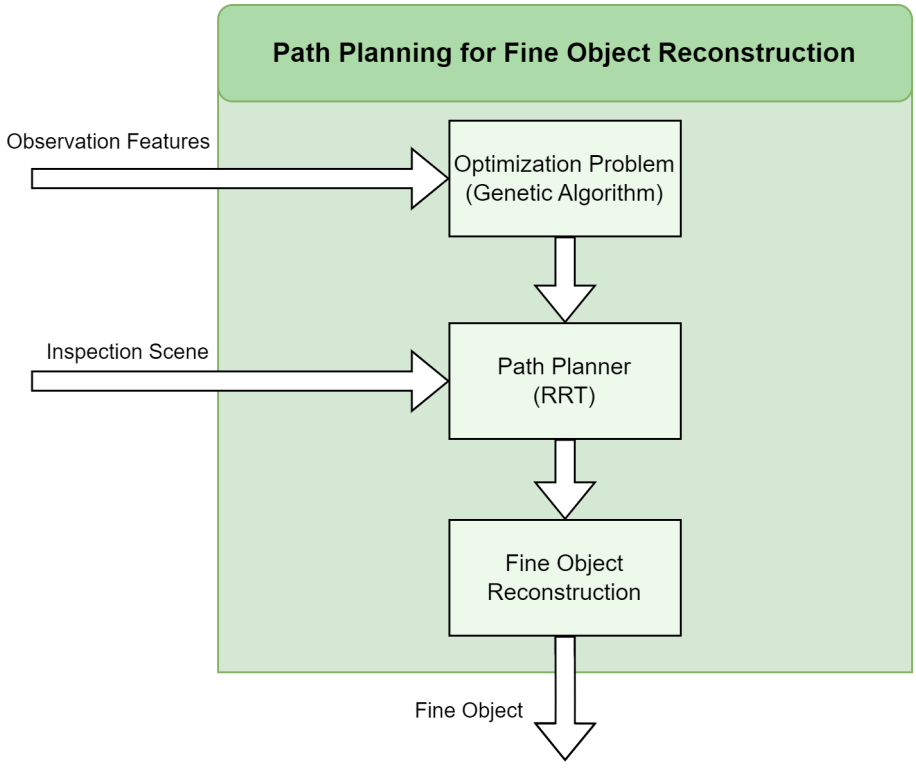

Figure 4.6: Path planning for fine object reconstruction stage.

The path planning optimization process follows a two-step approach. First, it determines the optimal sequence of anchor points to minimize total travel distance. Second, it computes the

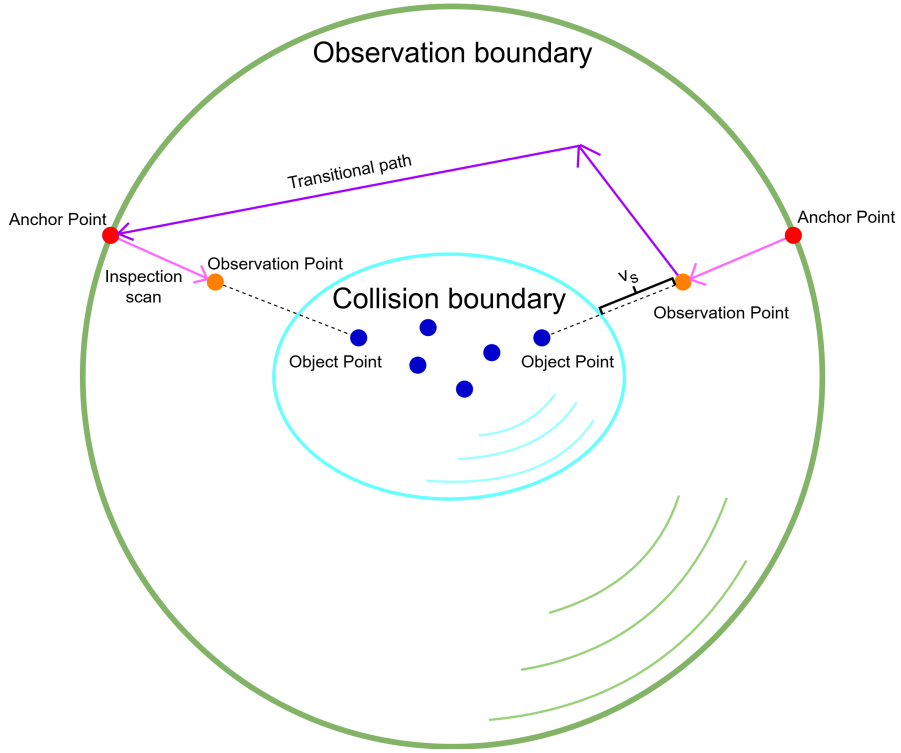

Figure 4.7: Inspection scene and inspection path comprising the collision boundary (cyan), observation boundary (green), object points (blue), observation points (orange), anchor points (red), inspection scans (pink) and the transitional paths (purple).

optimal path between consecutive observation-anchor point pairs while respecting the defined constraints of the inspection scene.

Genetic algorithms are optimization techniques inspired by the principles of natural selection and genetics. By iteratively evaluating and evolving a population of candidate solutions, genetic algorithms efficiently search the solution space to identify the optimal sequence of points that minimizes the total travel distance. To optimize the sequence of anchor points, the algorithm employs a Genetic Algorithm (GA) that minimizes the total path length based on Euclidean distances.

Once the optimal sequence is established, the Rapidly-exploring Random Tree algorithm is employed to plan the transitional paths between observation points and their subsequent anchor points. The RRT algorithm operates within the constraints of the previously defined inspection scene, treating both the volume inside the ellipsoid and the region outside the sphere as obstacle spaces. To mitigate the inherent randomness of RRT, the algorithm generates 20 candidate paths for each transition, selecting the shortest valid path. The path planning process incorporates several additional constraints to ensure safe and effective vehicle operation:

- A vertical boundary constraint accounting for seabed proximity;
- Roll angle limitations constrained to $[-10°, 10°]$;
- Extended pitch angle range of $[-80°, 80°]$ to accommodate inspection scan maneuvers;

- Normalized yaw angle bounds of $[-180°, 180°]$.

The resulting inspection path guides the vehicle through a systematic data acquisition process, enabling comprehensive coverage of the target object while maintaining optimal sonar resolution and vehicle safety. The collected high-resolution multibeam data undergoes processing and analysis to generate a detailed 3D reconstruction of the object. This fine reconstruction provides precise geometric information about the object's structure and characteristics, facilitating the planning and execution of complex underwater tasks such as manipulation, intervention operations, or autonomous docking maneuvers.

4.3 Experimental Validation

The following section presents all the results obtained from the implementation and testing of C2FARUS. To thoroughly assess its performance, several tests and validations were conducted across simulated and controlled environments. C2FARUS's first and second stages were validated in three different realistic 3D environments in Gazebo [182] and through real controlled underwater experiments. The third and final stage was validated in a simulated environment to evaluate the method's effectiveness in achieving efficient and safe fine 3D reconstructions.

To fully evaluate C2FARUS initial stages described in sections 4.2.1 and 4.2.2 three different simulation scenarios were created with different depthmaps and structures along with two real controlled experiments:

1. Scenario 1 (figure 4.8a) - evaluates the ability of C2FARUS's initial stage to independently segment each object from the sea floor. This scene comprised five docks and four obstacles positioned in close proximity with different poses, placed in a 6-meter cube centered at the origin. Each dock was placed at different depths, ensuring a maximum rotation of 0.2 rad in roll and pitch. Objects were positioned in close proximity to each other with several different poses in an environment with small depth variations (see figure 4.8c). Table 4.1 provide a comprehensive breakdown of the position and orientation of each object within the Gazebo environment;

Table 4.1: Position and orientation of each object in the underwater gazebo scenario 1.

Object	**x (m)**	**y (m)**	**z (m)**	**roll (rad)**	**pitch (rad)**	**yaw (rad)**
Dock 1	-5.78	-4.00	-3.75	0.00	0.0297	0.00
Dock 2	-5.00	1.25	-4.00	0.1765	0.00	1.547
Dock 3	-0.0176	3.989	-4.95	0.1565	0.1423	0.7875
Dock 4	5.00	4.00	-5.40	0.00	0.00	1.547
Dock 5	5.00	-4.00	-5.40	0.00	0.00	0.00
Obstacle 1	-3.00	-4.00	-5.00	0.00	0.00	-1.62
Obstacle 2	-4.00	5.50	-4.80	0.00	0.00	0.50
Obstacle 3	0.00	0.00	-5.6	0.00	0.00	0.00
Obstacle 4	5.00	-0.50	-6.00	0.00	0.00	0.00

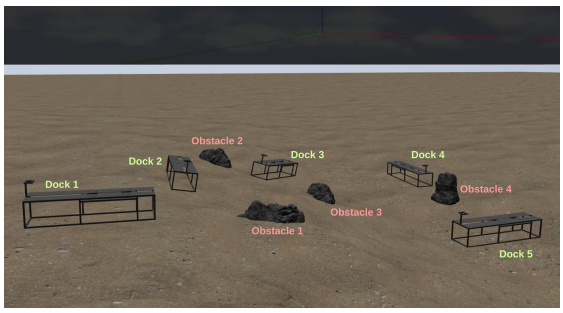

(a) Scenario 1 - Underwater environment in gazebo simulator.

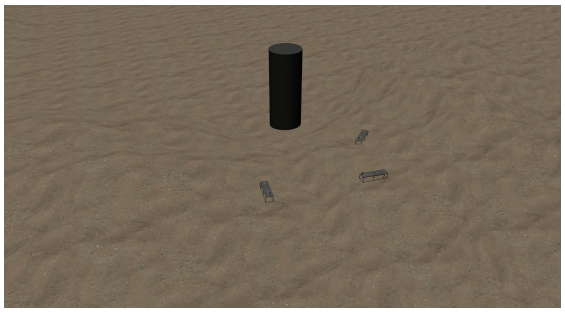

(b) Scenario 2 - Underwater environment in gazebo simulator.

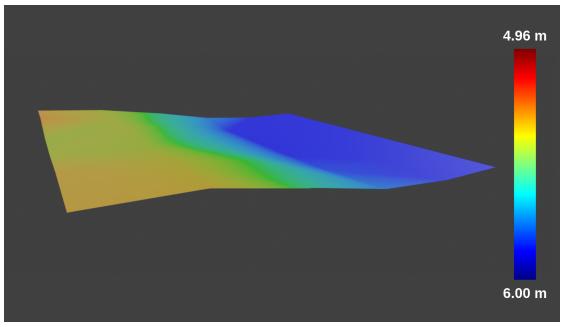

(c) Scenario 1 - Depthmap used in gazebo simulator.

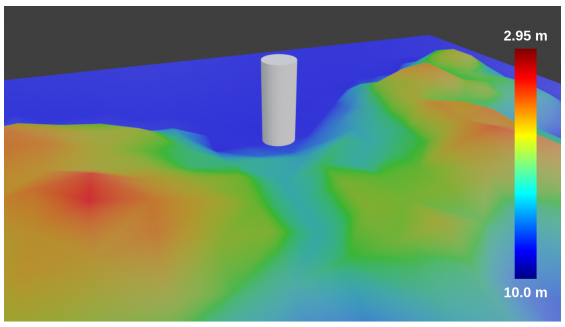

(d) Scenario 2 - Depthmap used in gazebo simulator.

Figure 4.8: Description and depthmap of scenarios 1 and 2. The red and blue colors represents the minimum and maximum depths of the seabed, respectively.

2. Scenario 2 (figure 4.8b) - designed to test the robustness of the method to high depth variations and the ability to segment a realistic cylinder structure (monopile), a typical foundation type adopted in offshore wind farms. The environment featured harsh depth variations (ranging from 2.95m to 10m), as shown in figure 4.8d, with a cylinder-shaped object with a 2-meter radius representing a monopile, and three docks placed at different depths, ensuring a maximum rotation of 0.2 rad in roll and pitch;

3. Scenario 3 (figure 4.9) - developed to access the results of the method in a realistic scenario, similar to the one present at the ATLANTIS Coastal Testbed [183]: equipped with a floating structure, a decommissioned Catenary Anchor Leg Mooring (CALM) buoy named DURIUS. The floating structure has a diameter of 16 meters and a height of 6 meters, anchored using four mooring chains. The seabed configuration from the first scenario was utilized in this test, with small varying depths along the XY-plane;

4. Experiment 1 - aimed to evaluate C2FARUS capability in exploring and segmenting submerged objects with complex geometries, conducted at CRAS's indoor pool using a small sunk boat;

5. Experiment 2 - aimed to assess the method's effectiveness in segmenting smaller, yet significant, underwater components such as anodes, tested at CRAS's indoor pool with an anode typical of structures like the DURIUS buoy.

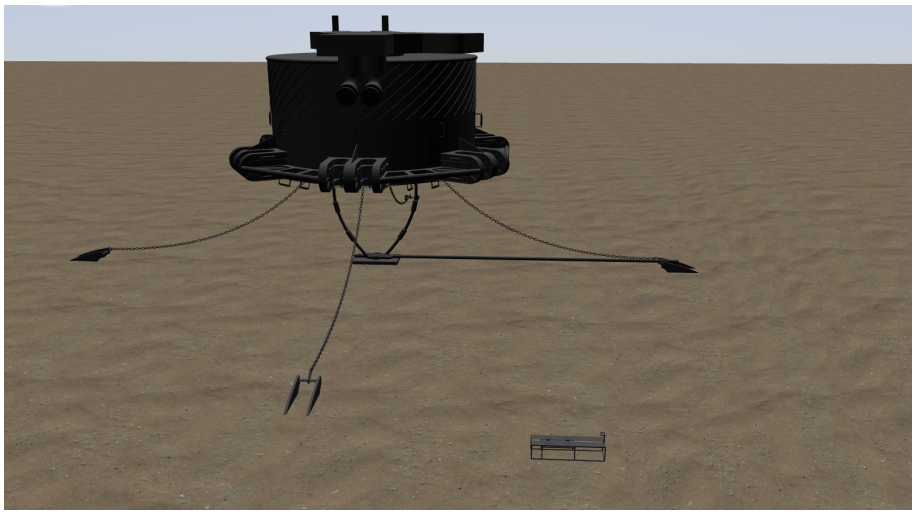

Figure 4.9: Scenario 3 - Underwater environment in gazebo simulator.

All three different realistic 3D environments were created in Gazebo [182] taking into account both realistic structures as well as real environment constrains such as, currents and noisy sensory information, to be inspected using with a model of the RAYA AUV, shown in figure 4.10, including all the onboard sensors. All sensors are affected by Gaussian noise, parameterized according to the specifications of each sensor datasheet.

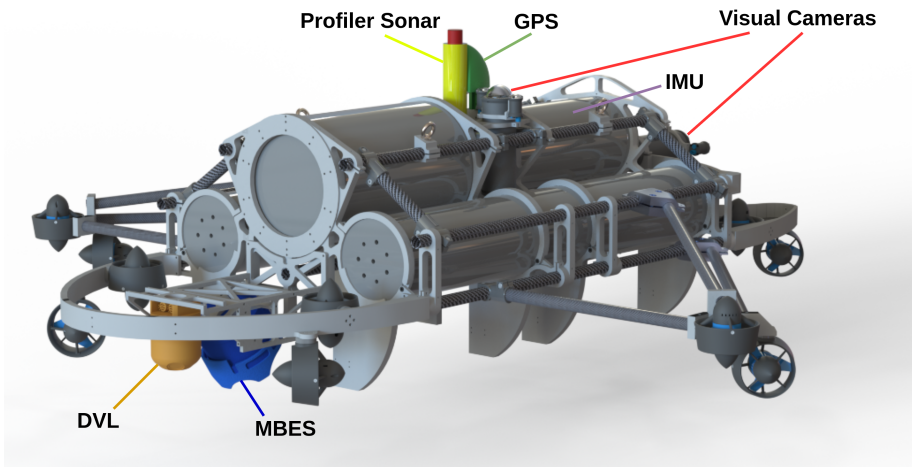

Figure 4.10: RAYA CAD with the sensor payload attached. The blue and yellow lines are distance sensors, red is imaging sensors, and purple and orange lines are navigation sensors, respectively. CAD, computer-aided design; GPS, Global Positioning System; IMU, Inertial Measurement Unit; MBES, Multibeam Echosounder.

To ease visualization, each test was conducted using a compact scenario similar to the one presented in figure 4.13a. All tests were performed on a ASUS TUF DASH F15 laptop with an Intel Core i5-11300H @ 3.10GHz × 8 CPU and 8GB DDR4 RAM.

4.3.1 Validation in Realistic 3D Simulation Scenarios

One sample mission for evaluating C2FARUS' initial stages in scenario 1 and 2, uses the inspection trajectory depicted in figure 4.11 defined for the vehicle to maneuver at 1 meter depth of the surface of the water. Since RAYA lacks information about the seabed environment, a grid coverage trajectory is outlined, with cells measuring 2 meters in size and covering a total area of 8x8 meters. This trajectory performs the following steps:

1. AUV starts at the center of the grid.
2. RAYA moves to lowest left point of the grid map;
3. A lawnmower path is executed to ensure complete coverage of the area.

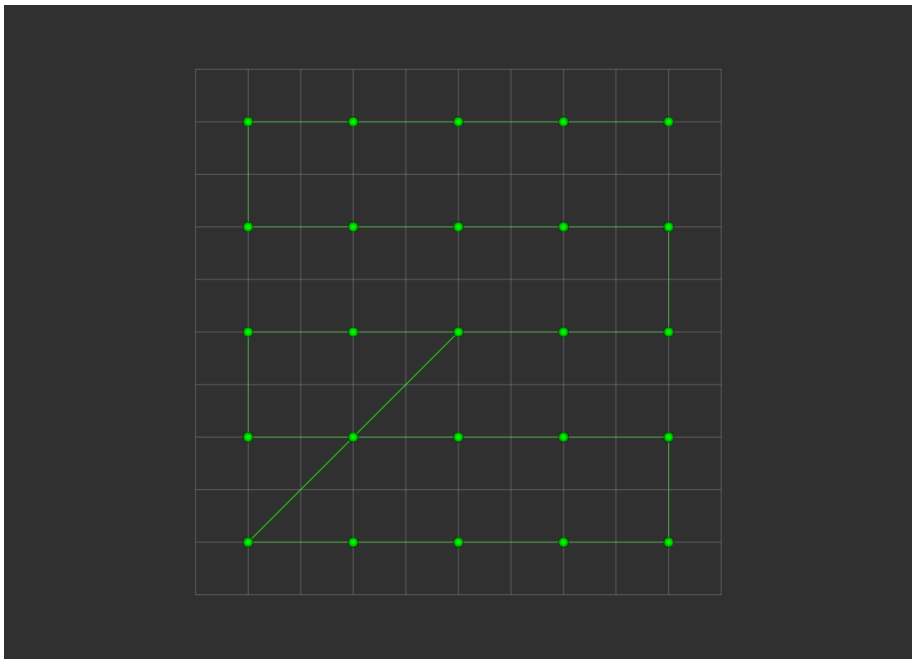

Figure 4.11: Coverage path defined at the surface of the water.

Table 4.2: The underwater currents in the Gazebo simulator are described as follows: the terms *Mean*, *Min*, and *Max* denote the average, minimum, and maximum acceptable currents, respectively. Additionally, noise amplitude (*noiseAmp*) and μ represent the variation in noise amplitude over time.

	mean	**min**	**max**	μ	**noiseAmp**
velocity ($\mathrm{m\,s^{-1}}$)	0.0	-0.3	0.3	0.0	0.01
horizontal angle (rad)	0.0	$-\pi$	π	0.0	0.1

The trajectory was carried out under two distinct environmental conditions: with and without underwater currents. Underwater currents were expressed as a function of magnitude and horizontal angle and vertical angle modelled using a first-order Gauss-Markov process [184]. Table

4.2 illustrates the average, minimum, and maximum acceptable currents, alongside the mean and maximum amplitude noise produced for both velocity and horizontal angle. It's important to note that the analysis solely accounts for underwater currents within the XY-plane, hence the vertical angle is presumed to be 0 $\mathrm{m\,s^{-1}}$.

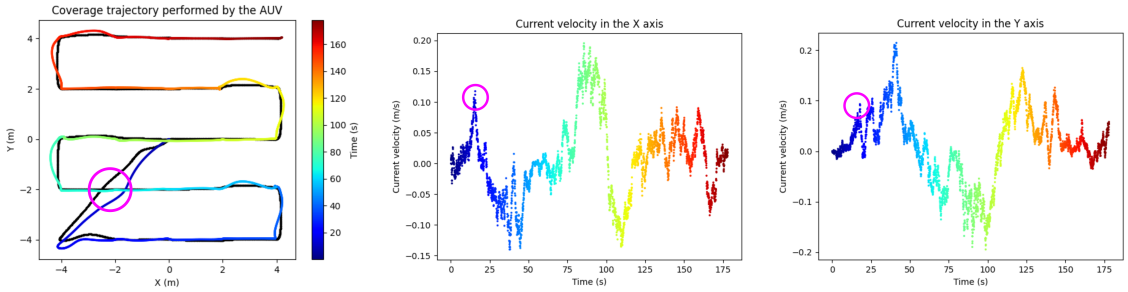

(a) (b) (c)

Figure 4.12: Trajectories performed by the AUV (a) with (colored) and without (black) the influence of underwater currents. Current velocity throughout the trajectory along the xx (b) and yy (c) axis, respectively. Pink circle represents the time at which the most significant deviation occurred.

During the execution of the trajectory, a PID positional control method was added and, thereby, drift in the XY-Plane due to the underwater currents was reduced. Figure 4.12 illustrates two distinct trajectories executed by the RAYA AUV during a single mission: one in the presence of underwater currents (colored) and the other without (black). The most significant deviation occurs around 20 seconds (indicated by the pink circle), where the vehicle experiences X and Y currents of approximately 0.1 meters per second each. Given that the AUV starts at the map's origin with zero angle, this slight deviation can be attributed to the challenge of compensating for underwater currents while simultaneously turning and moving along the XY-plane.

The objective of the back-and-forth strategy is to acquire multiple multibeam sonar rays, and subsequently organize them into a sliding window data structure. To achieve this objective with minimal errors, the vehicle should maintain stability along the trajectory. Consequently, the vehicle should only rotate upon reaching the final point of each segment. At this juncture, the vehicle executes simultaneous angular and linear movements until it reaches the subsequent segment, resulting in the remaining minor deviations observed in figure 4.12a.

While executing the path at a nominal linear velocity of 0.5 $\mathrm{m\,s^{-1}}$, multiple 3D scans are retrieved from the multibeam sonar and concatenated. For this simulation, 100 sonar rays were concatenated in a sliding window (SW) data structure (figure 4.13b), changing the data modality to a 3D point cloud. Like explained in subsection 4.2.1 the depth gradient of the point cloud that composed the sliding window is analysed to allow for the segmentation of foreign objects present on the sea floor. A grid size of 0.2 meters was used, in this particular case, to downsample the initial point cloud. Figure 4.14 depict the depth gradient across the sliding window shown in figure 4.13. As its demonstrated, the depth gradient is higher in cell grids that have points belonging to an object (colored bars) than in cell grids that only have points belonging to the seabed (blue bars). Coarse object segmentation is finally obtained taking into account the difference in gradient

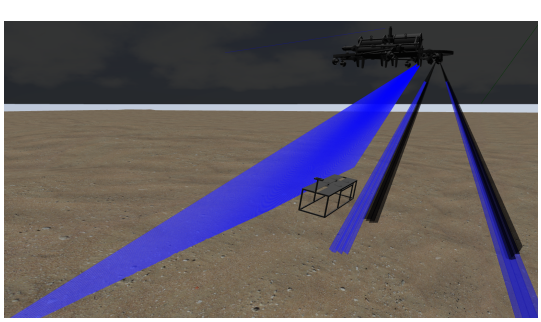

(a) Underwater multibeam 3D scan of the environment in gazebo simulator.

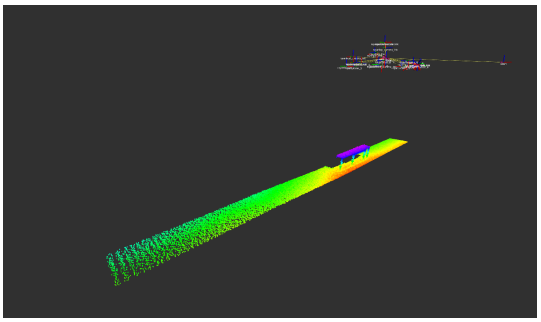

(b) Concatenation of multiple 3D scan rays from the m3 multibeam sonar.

Figure 4.13: Example of the Sliding Window (SW) data structure obtain in the gazebo simulator.

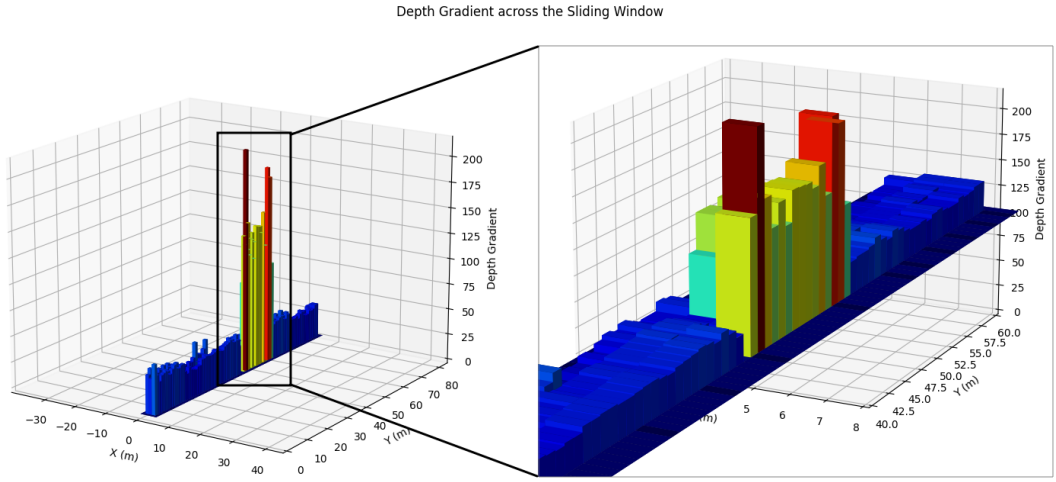

Figure 4.14: Depth gradient across the sliding window data structure.

intensity, that allow for the segmentation of the 3D points that are contained by the cells that have the highest depth gradients.

The results when applying the method described above to Scenario 1, illustrated in figure 4.8, can be observed in figure 4.15. The method was able to individually segment each of the objects present in the scene. It's also noticeable that the point density for each object varies. That happens due to the performed inspection trajectory. For objects positioned further from the center, the point density is lower, as seen with Dock 1 (pink). Similarly, the same occurs for objects positioned at the center of the trajectory, like Obstacle 3 (green). In these cases, the number of times the objects are inspected by the multibeam sonar is lower, resulting in reduced point density. Despite these variations in density, the algorithm effectively segmented each object, regardless of their position and orientation.

Table 4.3 shows the distance between the centroids of the object model's and the centroids of the segmented objects in Scenario 1. The average error in this scenario was approximately 0.33 meters. This error is primarily due to the asymmetry in the points obtained for each model. This

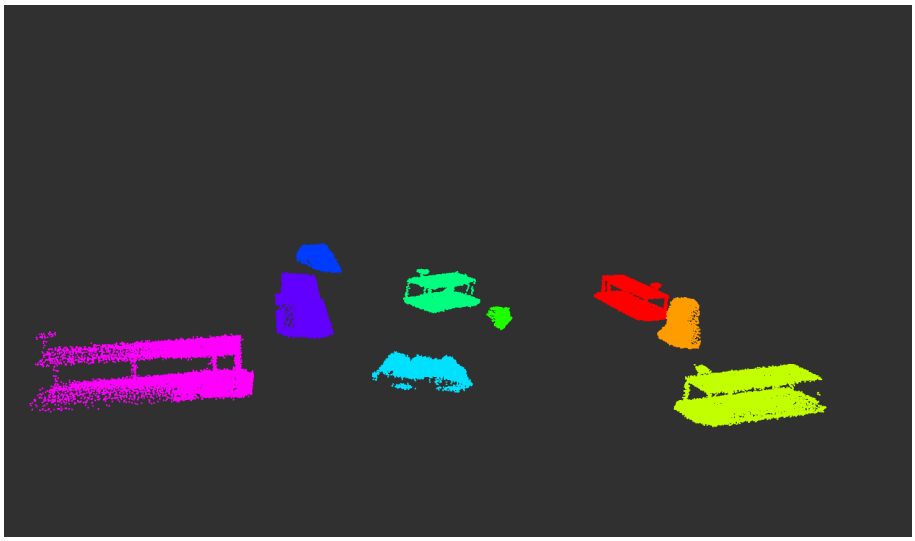

Figure 4.15: Scenario 1 - Objects segmented using the C2FARUS. Each color represents a unique object.

Table 4.3: Error distance between the centroid of the model to the centroid of each segmented object in scenario 1.

	$error_x$ (m)	$error_y$ (m)	$error_z$ (m)	error distance (m)
Dock 1	-0.573	-0.083	-0.091	0.586
Dock 2	-0.192	-0.012	-0.130	0.232
Dock 3	0.058	0.202	-0.270	0.342
Dock 4	0.104	0.143	-0.123	0.215
Dock 5	0.188	-0.073	-0.140	0.245
Obstacle 1	-0.246	-0.126	-0.048	0.280
Obstacle 2	-0.248	0.261	0.018	0.360
Obstacle 3	-0.259	-0.497	0.018	0.561
Obstacle 4	0.319	-0.068	-0.048	0.330

discrepancy is further illustrated by examining the Dock 1 object (pink) and Obstacle 3 (green), which exhibited the highest centroid distance errors. Additionally, the algorithm segments a region around each object, which may include sections of the seabed, thus contributing to the centroid error. Nevertheless, the average Chamfer distance between the models and their respective reconstruction was approximately 0.0238 m. This value indicates that the reconstructed point clouds are accurate and faithfully represent the original shape of the objects.

Scenario 2 depicts an environment that is more similar to real-world conditions. This scene features three docks located on a highly irregular seabed and a monopile positioned on a flatter terrain. In this scenario, the maximum depth variation was approximately 7 meters, significantly greater than the 1 meter variation used in scenario 1. When applying the depth gradient method to scenario 2, the developed approach successfully segmented each dock in the environment, despite the seabed exhibiting more extreme depth gradients, as seen in figure 4.16a. The average centroid position error in this case is similar to the one presented in scenario 1, at 0.32 meters. To validate

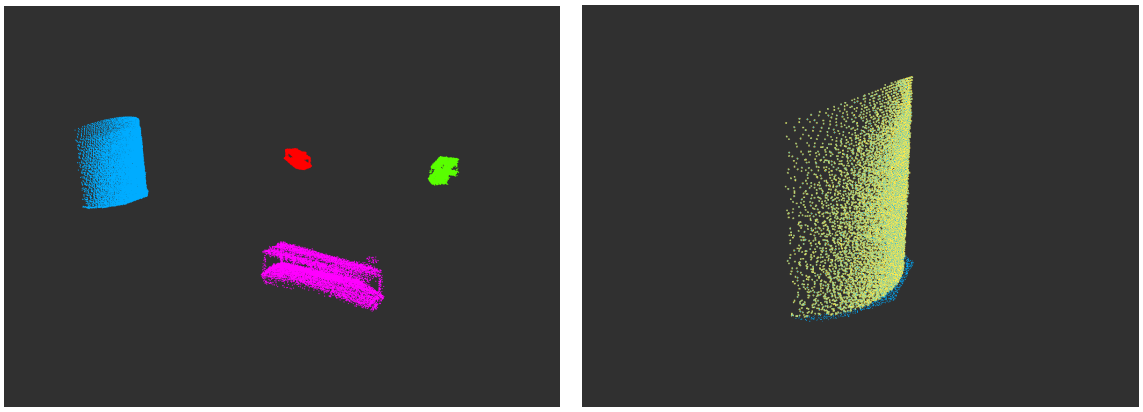

(a) (b)

Figure 4.16: The objects segmented from scenario 2 using C2FARUS are illustrated in figure (a). Each color represents a unique object. The cylinder model estimated using RANSAC iterative method is depicted in figure (b). Blue and yellow points depict the segmented cylinder, result from C2FARUS, and the fitted cylinder from the RANSAC estimator, respectively.

the quality of the segmented data, a RANSAC robust estimator was used to obtain the cylinder coefficients from the segmented cylinder (blue). RANSAC fits a cylinder with a radius of 2.054 meters, centered at coordinates (0.009, 15.069), as shown in figure 4.16b. This shows a radius error of 2.7% in radius and a positional error of approximately 0.07 meters for the center.

The third and final scenario aims to validate the developed method for environments similar to the ATLANTIS Coastal Testbed. To conduct a search for underwater objects around the DURIUS buoy, a new trajectory was defined, consisting of four points. This trajectory was designed to move around the floating structure with a distance of less than 6 meters, enabling the use of the profiling

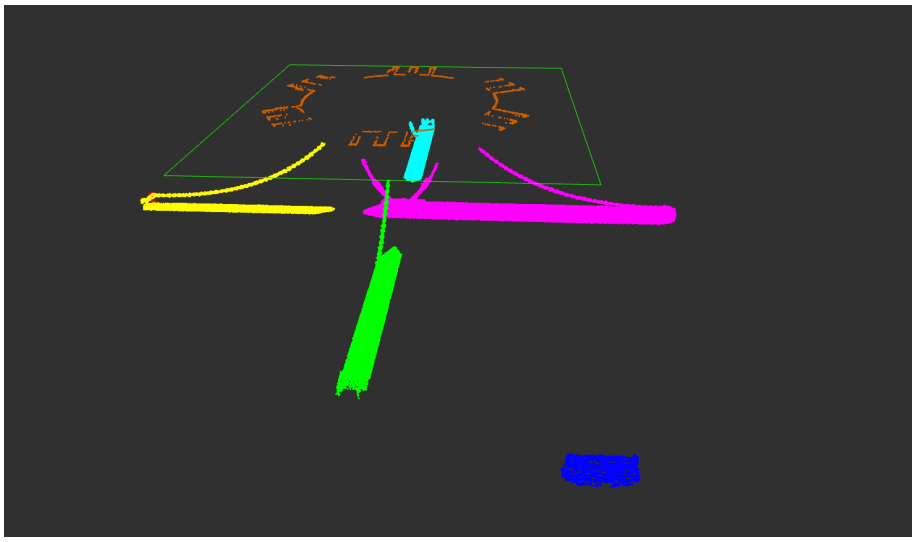

Figure 4.17: Scenario 3 - Objects segmented using C2FARUS. Orange points represent the concatenation of the points obtain by the pencilbeam sonar. Each remaining color represents a unique object.

sonar. As shown in figure 4.17, by following the green-marked path, the algorithm was able to segment each of the mooring chains individually. The pink-marked chain is segmented along with the central submarine hose due to the pipeline connecting them (see figure 4.9). Regarding the yellow-marked points, a small portion of the anchor was segmented separately from the chain. This happened due to the low density of points obtained in this specific region. The use of the profiling sonar provided complementary data, allowing for a sparse reconstruction (orange) of the skirt of the DURIUS structure. Moreover, this approach enhanced safety during navigation in close proximity, offering real-time feedback on the distance to potential collisions.

4.3.2 Controlled Underwater Experiments

To fully validate C2FARUS two initial stages, a series of controlled underwater experiments were conducted at CRAS's indoor pool. These experiments aimed to demonstrate the method's effectiveness in real-world conditions. Two distinct tests were performed: one involving a small sunk boat and the other using an anode, a common component in underwater structures such as the DURIUS buoy. The experiments employed an Imagenex 837b multibeam sonar and a Qualisys underwater motion tracking system, which estimated the sonar's odometry throughout the tests. The results of each segmented object are shown in figure 4.18. The sonar's odometry is represented in each image, with red arrows showing the sonar head's orientation

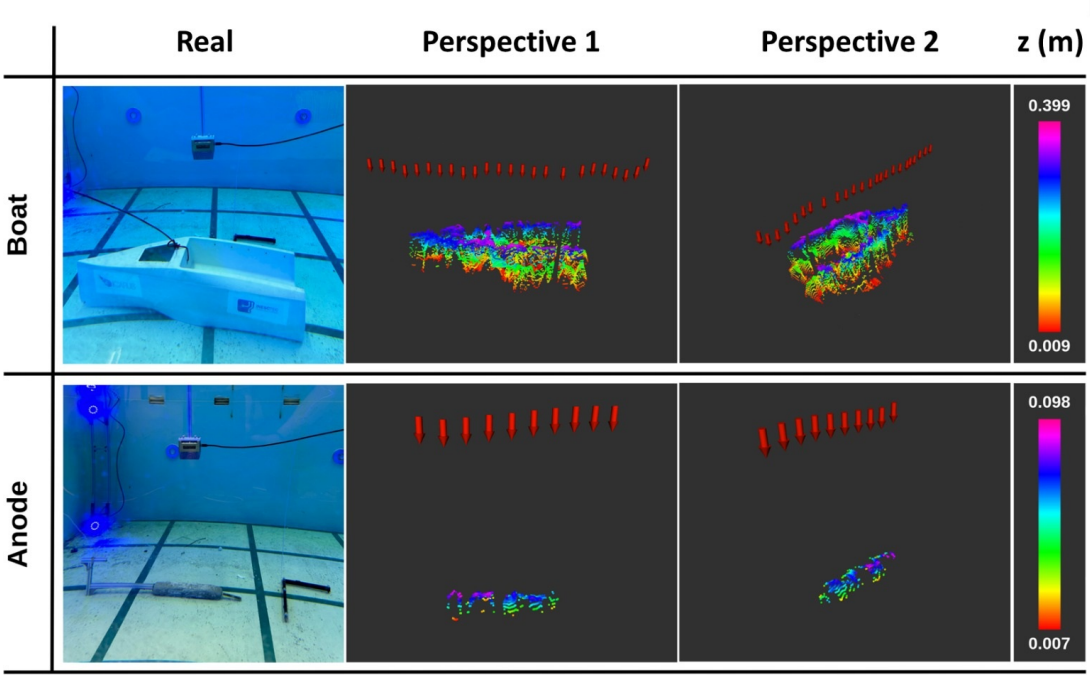

Figure 4.18: Segmented point clouds using C2FARUS methodology in a real underwater environment, for two different objects (Boat and Anode). Red arrows depict the odometry of the sonar sensor throughout each experiment.

The first experiment aimed to evaluate the C2FARUS' capability in detecting and analyzing submerged objects with complex geometries. C2FARUS was applied to scan and segment the

submerged boat, using the Imagenex 837b multibeam sonar and the Qualisys system to capture the depth profile and structural details of the boat. The data obtained were analyzed to determine the accuracy of the method in identifying and characterizing the boat's structure. Comparisons were made between the actual dimensions of the boat and the measurements obtained through the method. C2FARUS successfully detected the small sunk boat, accurately mapping its contours and structural features.

The second experiment aimed to assess the C2FARUS' effectiveness in detecting smaller, yet significant, underwater components such as anodes. An anode, similar to those used in the DURIUS buoy, was placed at the bottom of the pool. For this experiment, the anode was considered a cylinder due to its severely worn-out condition. The radius of the anode was measured along its length, and the mean value was used for the analysis. The effectiveness of the method was evaluated based on its ability to detect the anode and measure its dimensions accurately. The collected data were compared to the known specifications of the anode. C2FARUS proved effective in detecting the anode, accurately pinpointing its location and dimensions.

Table 4.4: Performance of the proposed methodology in a real underwater environment, using two different objects (Boat and Anode).

Dimensions		Measured (m)	Estimated (m)	Absolute Error (m)	Relative Error (%)
Boat	Length	1.520	1.543	0.023	2.829
	Width	0.520	0,533	0,133	2.500
	Height	0.390	0.399	0.009	2.308
Anode	Length	0.590	0.609	0.019	3.220
	Radius	0.0826	0.0849	0.0023	2.785

The quantitative results of these tests are detailed in table 4.4, which compares the measured dimensions of the objects with the dimensions extracted from C2FARUS's 3D representation. For the small boat, the measured length, width and height were 1.520, 0.520 and 0.390 meters, respectively, representing a maximum relative error of 2.829% across these dimensions. These results demonstrate the method's ability to segment objects/structures from the seabed. For the anode, the measured length was 0.590 meters, and the estimated length was 0.609 meters. This yielded absolute and relative errors of 0.019 meters and 3.220%, respectively. The slightly higher relative error compared to the boat measurements reflects the challenges posed by the smaller and more worn-out structure of the anode. Nevertheless, considering the anode's condition and small size, the proposed method showed commendable accuracy in estimating the radius with a relative error of 2.785%.

4.3.3 Fine 3D Object Reconstruction

This subsection 4.3.3 evaluates the effectiveness of the proposed method in achieving fine 3D object reconstructions. The evaluation focuses on metrics such as inspection duration and path

distance, as well as the accuracy and completeness of the three-dimensional output within a simulated environment. For the purpose of this demonstration, the selected structure to be inspected consists of the dock specifically designed to interface with the RAYA vehicle, whose model is depicted in figure 4.13a. This model has a length of 2.56 m, a width of 0.7 m and a height of 0.89 m.

To identify the docking station and given that it primarily consists of a planar surface, a Plane RANSAC estimator was employed to verify if the object indeed contained any planar features. Subsequently, object points were extracted, with particular attention given to the corner points that belonged to the detected plane. From these points, structural characteristics such as the length-to-width ratio were derived.

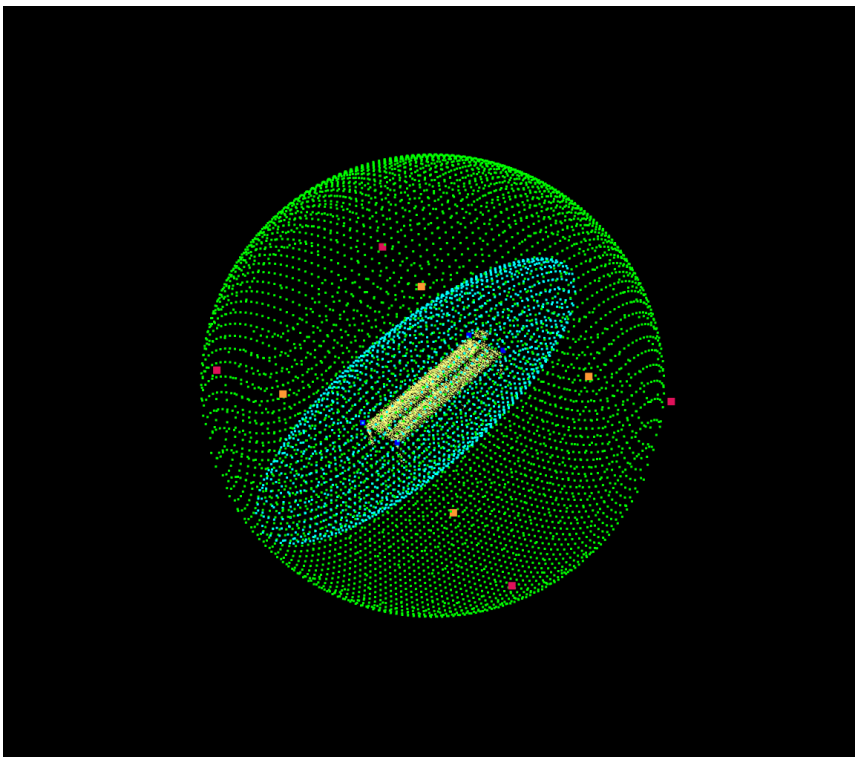

Figure 4.19: Feature tracing and inspection scene for a 0.03 meters resolution.

As described in section 4.2.3, the inspection trajectory is obtained through a multi-step process. First, the inspection scene is defined, for a custom resolution, composed of two different volumes: a sphere and an ellipsoid. Figure 4.19 depicts the inspection scene obtained for the intended structure with a resolution of 0.03 meters. Green points show the sphere that is computed around the detected object, ensuring a fine resolution for subsequent reconstruction tasks, while in light blue is the collision ellipsoid, ensuring that potential obstacles are accounted for in navigation planning. With the inspection scene defined, it is then possible to project the object points (dark blue) into the navigable space, resulting in the anchor points (red) and the observation points (orange). The final trajectory (shown in figure 4.20c) consists of two components: inspection scans that traverse between anchor and observable points with slight pitch rotation, and optimized

paths connecting consecutive observation points.

For these experiment, the Genetic Algorithm was configured with the following parameters shown in equation 4.8:

$$\begin{aligned} \text{Population size} &= 24 \\ \text{Number of generations} &= 200 \\ \text{Crossover probability} &= 0.8 \\ \text{Mutation probability} &= 0.2 \end{aligned} \tag{4.8}$$

These parameters were selected to balance computational efficiency with solution quality for the given inspection scenario. The population size and number of generations provide sufficient exploration of possible path combinations while maintaining reasonable computation time (average of 0.111 seconds).

The proposed coarse-to-fine approach (C2FARUS) was compared against two state-of-the-art methods adapted for autonomous underwater vehicles: the Energy-Efficient Path Planning Algorithm (EEPPA) [90] and Bircher's Structural Inspection Path Planning Algorithm [89]. EEPPA focuses on energy efficiency, a critical consideration for AUVs operating in energy-constrained underwater environments. On the other hand, Bircher's algorithm [89] emphasizes structural inspection, aligning closely with the goals of detailed 3D reconstructions. By comparing against these two methods, we can demonstrate the comprehensive advantages of our method across multiple performance dimensions. While initially designed for unmanned aerial vehicles, these methods possess core principles that allow there adaptation to AUVs.

Overall, the quantitative discussions are guided by the following metrics, used to evaluate the fine reconstruction:

- d_p: Distance of the close-range inspection path (in meters);
- t_p: Elapsed time of the inspection path (in seconds);
- acc: Accuracy of the 3D fine reconstruction (in meters);
- cmp: Completeness of the 3D fine reconstruction (in percentage);

To assess accuracy, the 3D Chamfer distance metric is used evaluating the similarity between the reconstruction and its original model. This distance is defined as the sum of the distances from each point in point cloud A to its nearest neighbor in point cloud B, plus the sum of the distances from each point in B to its nearest neighbor in A. Regarding the completeness metric, the point cloud of the model is first converted into a voxel grid with a voxel size equal to 0.03 meters, matching the desired resolution of the fine reconstruction. Subsequently, the percentage of voxels occupied by points from the reconstruction is determined. These four metrics will allow us to infer the quality of the reconstruction as well as the effort required to achieve it.

Table 4.5 and figure 4.20 summarizes the quantitative results obtained from the experiments. Each metric is averaged over 10 test runs to ensure robustness and reliability of the results. The

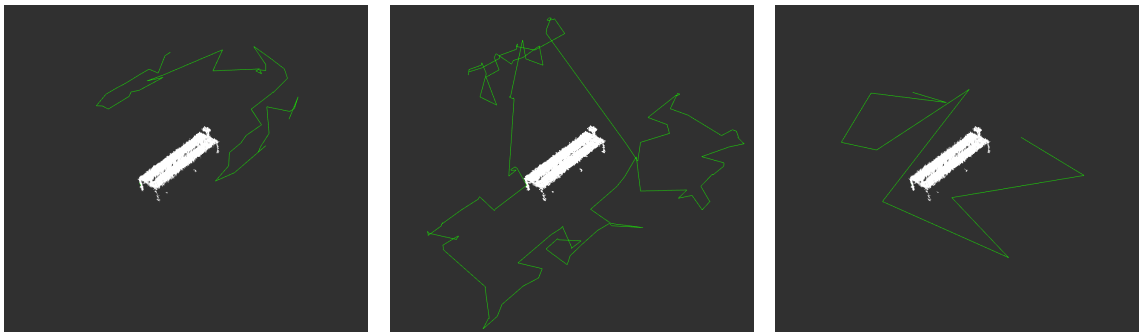

(a) EEPPA [90]. (b) Bicher [89]. (c) C2FARUS.

Figure 4.20: Paths obtained for the inspection of the underwater dock (white). Paths are represented by the green line.

Table 4.5: Quantitative comparison of the different 3D underwater reconstruction methods.

Method	d_p (m)	t_p (s)	*acc* (m)	*cmp* (%)
Coarse	-	-	0.0243	43.49
C2FARUS	28.48	**130**	**0.0076**	**87.04**
EEPPA [90]	**18.7**	210	0.0252	63.11
A. Bircher et. al [89]	62.40	519	0.0167	81.78

proposed method achieved a distance of 28.48 meters, which, while not the shortest, allowed for the quickest execution, providing a balance between path length and comprehensive coverage. The inspection time for the proposed method recorded the shortest elapsed time of 130 seconds, significantly less than EEPPA's 210 seconds and Bircher's 519 seconds. This demonstrates the proposed method's time efficiency, making it highly suitable for time-sensitive operations. EEPPA achieved the shortest distance of 18.7 meters, indicating high efficiency in terms of path length, but the final reconstruction showed lower accuracy and completeness. In terms of accuracy, C2FARUS

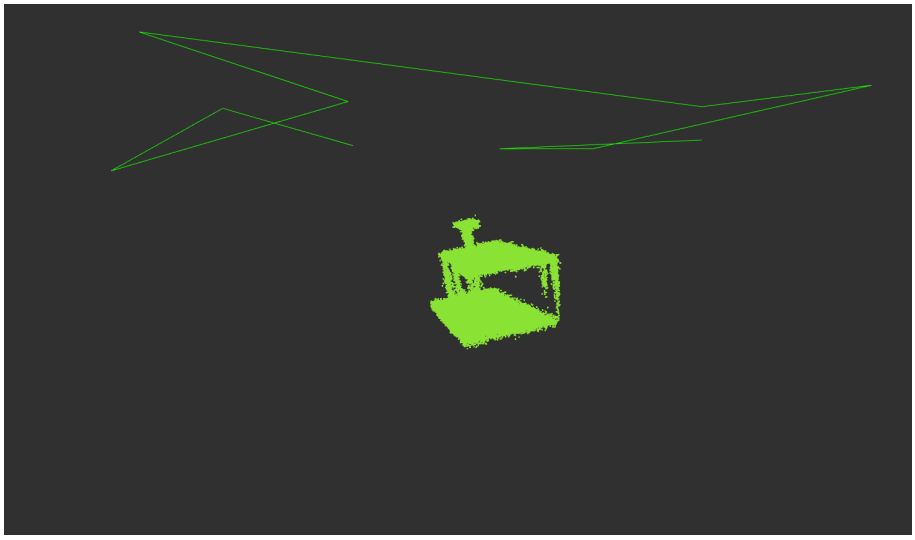

Figure 4.21: Fine reconstruction of the scene using C2FARUS.

resulted in a highest accuracy of 0.0076 meters, indicating superior capability in capturing fine details of underwater structures, as shown in figure 4.21. This is a substantial improvement over EEPPA (0.0252 meters) and Bircher's method (0.0167 meters). Furthermore, the proposed method also achieved the highest completeness at 87.04%, outperforming EEPPA's 63.11% and Bircher's 81.78%. This high completeness indicates that the proposed method provides a more thorough and comprehensive 3D reconstruction.

The improvements in inspection path distance, time, accuracy, and completeness highlight the effectiveness of C2FARUS in the context of underwater environments. The balance in inspection path length and reduced elapsed time indicates that the proposed method is highly efficient, which is crucial for AUV operations where energy and time resources are limited. The high accuracy and completeness levels suggest that the presented method is able to achieve detailed and thorough underwater reconstructions, making it a valuable tool for applications requiring precise 3D models, such as infrastructure inspection and intervention.

4.4 Final Considerations

This chapter introduces a new coarse-to-fine approach for 3D reconstruction of underwater structures (C2FARUS) using multibeam sonar. The method gradually refines its understanding of the environment through a series of stages aimed at enhancing AUV capabilities for exploration, detection, and recognition of underwater structures. By employing close-range inspection navigation in a novel scene representation, it overcomes the challenges posed by sonar resolution at longer distances, ensuring high-quality data acquisition.

Extensive experiments validate the proposed method in simulation and controlled environments. C2FARUS was able to accurately segment and identify objects even under significant depth variations and realistic seabed conditions. Obtained results under controlled experiments reveal a maximum relative error of 3.22% for the estimated object dimensions. C2FARUS segments submerged objects with complex geometries and detects smaller underwater structural components. C2FARUS' performance in fine 3D object reconstruction was evaluated against two state-of-the-art methods adapted for AUVs. The proposed method outperformed these methods in key metrics, including inspection path distance, elapsed time, accuracy, and completeness. Specifically, the method achieved the highest accuracy (0.0076 meters) and completeness (87.04%), while maintaining efficient inspection path distance and execution time.

In conclusion, C2FARUS offers a robust and efficient solution for underwater exploration and inspection tasks. It effectively balances the need for detailed 3D representations of the underwater environment with the practical constraints of AUV operations, such as time and energy limitations. The high accuracy and completeness of the reconstructions, coupled with the method's efficiency, make it a valuable tool for various underwater applications, including infrastructure detection and localization.

Chapter 5

Motion Planners Evaluation for Operations and Maintenance Tasks

Enabling manipulation-based docking represents a critical capability for achieving persistent autonomous underwater operations. The success of autonomous docking maneuvers depends heavily on the robotic system's ability to plan and execute precise manipulation trajectories while accounting for the unique challenges of the underwater environment. However, current motion planning approaches face significant limitations when applied to underwater manipulation tasks, particularly in the context of docking operations. Moreover, the field lacks standardized evaluation frameworks and performance metrics for underwater manipulation tasks. The existing motion planner evaluation approaches focus mainly on individual performance indicators such as planning time or path length, failing to capture the multiple requirements of underwater manipulation tasks where energy efficiency, safety margins, and execution accuracy must be considered simultaneously.

This chapter is organized as follows: Section 5.2 presents the new defined metric that takes into account multiple requirements of underwater robots for manipulation tasks. Section 5.3 describes the hardware used and the designed experience and fully analyzes the performance of the planners using the presented metric. At last, the most important conclusions of this chapter are presented in section 5.4.

5.1 Introduction

Underwater manipulation systems such as remotely operated vehicles and autonomous underwater vehicles already play an important role in several operations and maintenance activities. Nevertheless, many of these technologies have limited autonomy and range of exploration, and the ability to carry out autonomous intervention operations is still very limited [185]. There have been new imaging systems that provides dense and accurate 3D information from harsh underwater environments [106] but further automation of manipulation technologies can lead to greater cost savings and increased safety. Nowadays, these vehicles have been mainly used for survey missions, but

many existing applications require manipulation capabilities [153]. Over the past few years, several studies have been carried out to empower AUVs with these technologies and enable them to carry out operations, such as grasping objects [65, 66], valve-turning operations on panels [67, 68], force regulation tasks [69, 70] and cooperative manipulation [71].

Currently, there is a lack of planning and grasping techniques focused on increasing the performance and safety of current solutions for sophisticated O&M operations, such as maintenance and inspection operations of underwater structures. The high degree of complexity and the strictness of the requirements associated with the underwater environment are two factors that hinder progress in this area.

For O&M operations to be performed by AUVs, a set of requirements must be met by current motion planners, that were designed to perform well on land, so that they can be reused in this new application:

- For the safety of autonomous intervention, planners must return trajectories with the greatest possible minimum distance between the End-Efector (*Eff*) and the nearest collision point. In addition, safety is inversely proportional to uncertainty. In this way, long *Eff* movements cause greater uncertainty and, therefore, they are less safe.

- Motion planners must have high effectiveness, that is, restrict the joints movement to the minimum necessary and plan as fast as possible, reducing the energy use and minimizing the execution of long missions. Each joint has its own engine and needs more energy to move than to remain static, allowing the possibility to optimize the energy consumption throughout the entire mission and maintain the stability of the vehicle in environments where the associated inertia and currents are high.

- With the high complexity associated with the maritime environment, it must be ensured that all trajectories are executed as consistently as possible related to the planned ones. Each planner computes trajectories with unique characteristics, such as density of points and distance between them, that are performed differently by each specific manipulator.

Nowadays, it is difficult to choose a planner that fulfills all the requirements specified above as there are not yet metrics capable of characterizing them. Currently, the available analysis are performed between individual indicators and there is no metric available capable of taking into account several heterogeneous performance considerations. Based on the authors' current knowledge, there is no information about the execution of the available planners when applied to underwater operations.

This chapter presents a new metric that identifies the motion planner that best fits the set of requirements for underwater manipulation. This metric is called NEMU and evaluates the performance using several heterogeneous parameters, such as the total movement of each joint, the path length, the planning time, the minimum distance to the obstacle, the execution time, and the mean and standard deviation of the position error of the end effector, as well as the error of the trajectory. By error we mean the distance of the generated plan to its planner expected values. This metric

will allow to calculate the cost of each planner to plan and execute an underwater manipulation operation and thus, identifies the best collision-free path according to the requirements.

5.2 NEMU (plaNner Evaluation Metric for Underwater intervention)

The NEMU (plaNner Evaluation Metric for Underwater intervention) metric was defined by considering multiple variables according to the requirements of underwater robots for O&M tasks. The fastest planner may not be the planner that returns the shortest or safest solution and, this way, the metric combines different components and estimates a total cost for collision-free trajectories.

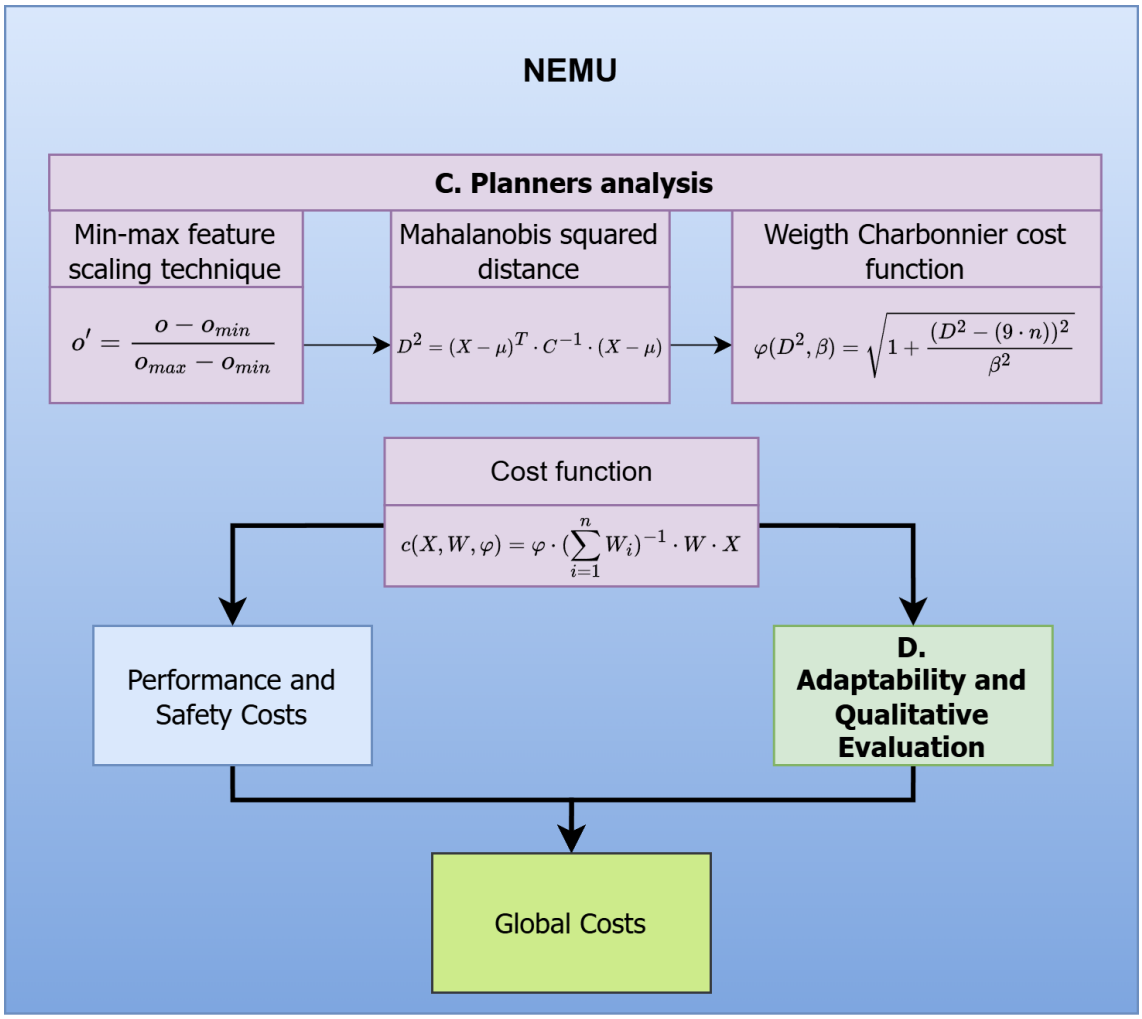

Figure 5.1: Representative diagram of NEMU.

NEMU considers that trajectory is calculated using planners that can have a random factor. Thus, it was defined to calculate the cost of planners using multiple heterogeneous data and to be robust when dealing with outliers. This metric is composed by three categories: effectiveness, safety and adaptability that are merged together with an influence cost related to the quality of the solution obtained (see figure 5.1). The influence cost is achieved by performing three different

techniques (Min-max feature scaling technique, Mahalanobis Distance and Charbonnier function) to the collected data and the total cost function can be defined as:

$$c(X,W,\varphi) = \varphi \cdot (\sum_{i=1}^{n} W_i)^{-1} \cdot W \cdot X \tag{5.1}$$

where c is the total cost, φ represents the influence cost function of the observation X and $W \in \mathbb{R}^{n\times 1}$, $n = 9$ is the vector composed by the cost of each feature.

Currently, planners have been studied above water and the performance evaluation through comparisons between singular indicators. With the transition to the underwater environment new metrics need to be defined to study, simultaneously, multiple indicators that must meet specific requirements of the underwater domain.

The metric that is proposed in this chapter takes into account several variables that are organized in three categories:

Definition 5.1. *Effectiveness* - the energy used by the manipulator throughout an entire mission. Composed by the total movement of each joint (J_i) and the planning time (t_p). Planning time represents the duration needed by planners to produce feasible paths. Planners with a low planning time are considered as high performance.

Definition 5.2. *Safety* - produce collision-free trajectories that protect the manipulator and all the surrounding structures. Formulated by the minimum distance to the obstacle (d_o) and the path length (d_{eff}). Long paths lead to a greater possibility of causing problems and/or collisions given the mobile platform.

Definition 5.3. *Adaptability* - the accuracy of the real hardware to executed the motion planned. Composed by the mean and standard deviation of the position error of the *Eff* related to its original plan (e_{eff}).

Kinematic redundancy is the capability of reconfigure the manipulator without affecting the position and orientation of the end-effector meaning that a small path length does not necessarily translates in a short movement of joints. Thus, planners with short path length are considered as high safety while short movement of joints are considered as high performance.

The adaptability of each planner to the manipulator will be analyzed, in order to understand which planner produces trajectories that, given the mechanical characteristics of the arm, are executed as similarly as the ones planned.

As previously said, the influence cost is achieved by performing three different techniques:

1. For sampling-based motion planners, all trajectories were computed multiple times because of the randomness of results. After that, all variables are normalized using the Min-Max feature scaling technique, presented in equation 5.2, to bring all values into the range $[0,1]$:

$$o' = \frac{o - o_{min}}{o_{max} - o_{min}} \tag{5.2}$$

where $o \in \mathbb{R}^n$, $n = 9$ since it considers multiple features such as planning time, movement of each joint, path length, etc. It is a vector composed of multiple absolute observation values and o_{max} and o_{min} are its maximum and minimum values, respectively.

2. The divergence is a measure of the representativeness of the trajectory in relation to its expected value. The higher this value, the more outlier the solution is considered and, therefore, the higher the cost that will be employed. The divergence criterion requires a distance measurement to evaluate the success of the planning operation. Assuming the obtained vector as being multivariate and normally distributed, then the X vector has n dimensions, $X \in \mathbb{R}^{1\times n}$, $n = 9$, and the difference between the planning operation and its distribution can be measured by the Mahalanobis squared distance:

$$D^2 = (X-\mu)^T \cdot C^{-1} \cdot (X-\mu) \tag{5.3}$$

where D^2 is the square of the Mahalanobis distance, X is the n-dimensional observation in range $[0,1]$, μ is the mean values of independent variables, and C^{-1} is the inverse covariance matrix of independent variables in this research. μ and C^{-1} are calculated by planning the same motion planning problem (MPP) 20 times.

3. Many problems in statistics and optimization require robustness: that a model to be insensitive to outliers. This means that an outlier cannot be worth the same as an inlier. To make NEMU more robust it needs to be able to identify solutions that are considered as outliers to reduce their input to the total cost computation. To do this, the inverse of the weight Charbonnier cost function, presented in the equation 5.4, was used:

$$\varphi(D^2,\beta) = \sqrt{1+\frac{(D^2-(9\cdot n))^2}{\beta^2}} \tag{5.4}$$

where φ is the influence cost, D^2 represents the square of the Mahalanobis distance of the observation values and β is a parameter that must be adjusted accordingly for each problem [1]. It was defined that a solution is inlier when each X, vector that composes all the observation values is within 99% of its distribution, that is, when $\mu_i - 3\sigma_i < x_i < \mu_i + 3\sigma_i$. The maximum Mahalanobis distance for a solution considered as an inlier is $9 \times n$ considering n variables .

[1] β values for MPP 1, MPP 2 and MPP 3 are 10000, 900 and 600, respectively.

5.3 Experimental Validation

This section presents three benchmarking analyses of 22 motion planners, assessed through the NEMU metric. Both simulation and real experiments were conducted during pick and place scenes. All simulations were designed to take into account the constrains of the real environment, so that the computed paths can be executed in the real arm without changes. Both non-optimizing and optimizing planners are considered for benchmarking.

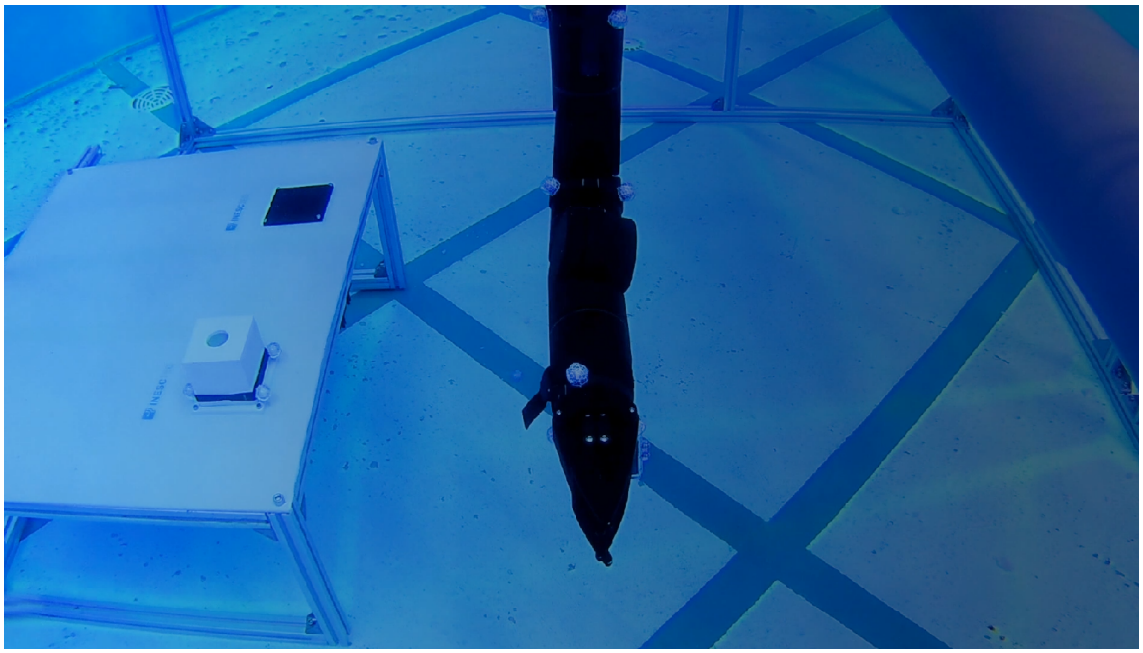

Figure 5.2: Experimental setup used during NEMU experimental validation. The figure depicts a cube and two poses placed on a table, the Bravo 7 manipulator on the center and a cylinder obstacle.

All selected planners address the same setup: the manipulator is attached to a metallic structure with dimensions 2x2x1 meters, as well as a cylindrical obstacle and a table. The aim of the manipulation task is to move the object from a defined initial pose on one side of the table (white base) to a final pose on the other side of the table (black base). The object is a cube with a size of 8 cm. The initial and final poses are located in the first and fourth quadrant, respectively. This way, due to the mechanical restrictions of joints: joint 0 (shown in figure 5.3) is not continuous and only moves from 0º to 359º; the manipulator will have to move between configuration extremes while avoiding a cylinder shape obstacle, like the one shown in figure 5.2.

Planners were tested using the Bravo 7 configuration, an advanced electric manipulator system designed for the harsh subsea environment, with a depth rate of 300 m. It has high accuracy joint positioning of 0.1º, grabber closing force greater than 1000 N and is a six degrees of freedom manipulator capable of lift a 10 kg object when fully reached. A model of the Bravo 7 with its gripper, the standard Denavit–Hartenberg (DH) parameters and its joint frames are presented in figure 5.3.

Link	d (m)	θ (rad)	a (m)	α (rad)
0	0.1074	$\theta_0 + \pi$	0.046	$\pi/2$
1	0.0	$\theta_1 - \pi/2 + \theta_a$	0.293	0.0
2	0.0	$\theta_2 - \pi/2 - \theta_a$	0.0408	$-\pi/2$
3	-0.160	θ_3	0.0408	$-\pi/2$
4	0.0	θ_4	0.0408	$-\pi/2$
5	-0.2235	θ_5	0.0	$\pi/2$
6	0.0	$-\pi/2$	0.120	0.0

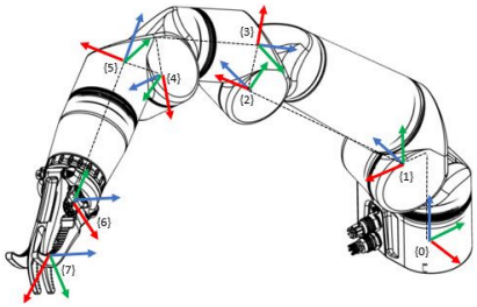

Figure 5.3: On the left - Standard Denavit–Hartenberg Parameters for Bravo 7 where $\theta_a = tan^{-1}(5.2/293.55)$. On the right - Bravo 7 joint frames. *xx*, *yy* and *zz* axis are presented in red, green and blue respectively.

Figure 5.4 presents simple examples for all motion planning problems that will be studied:

- MPP 1 - Simple motion scenario (point 1 to 2);
- MPP 2 - Obstacle avoidance while grasping scenario (point 2 to 3);
- MPP 3 - Obstacle avoidance scenario (point 3 to 1);

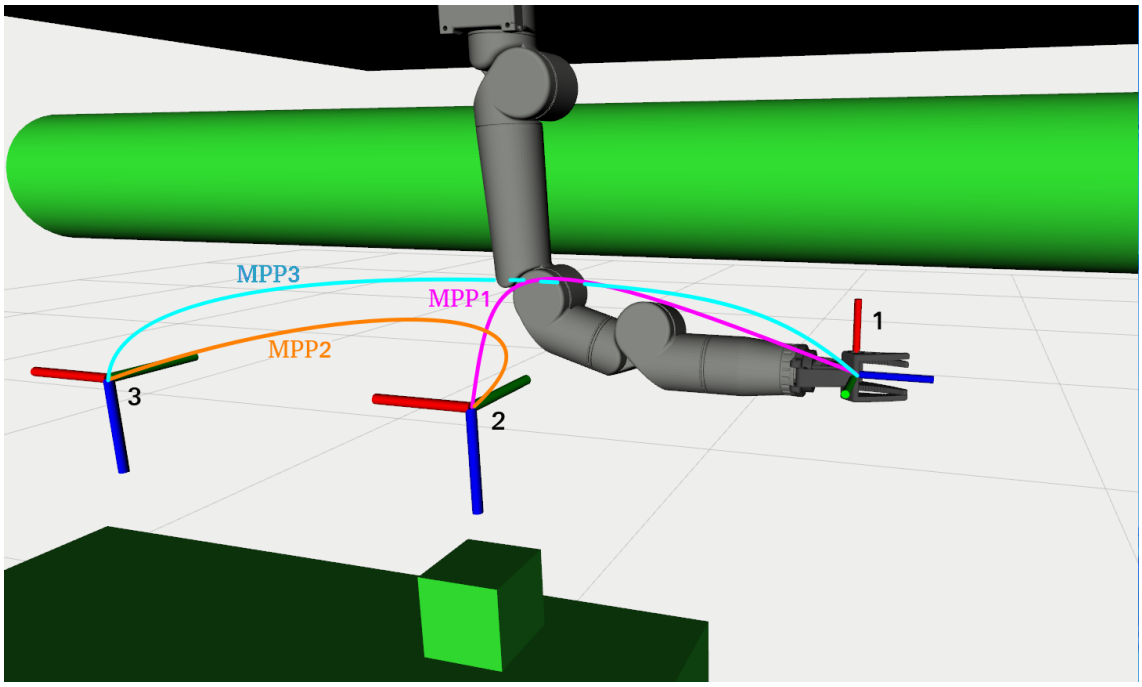

Figure 5.4: Bravo 7 in its initial position and the sequence of waypoints and example trajectories for each benchmark. In pink is an example trajectory for the first benchmark, in orange for the second and in light blue for the last motion planing problem.

In benchmark 1 the manipulator starts in a stretched arm configuration where the *Eff* is positioned at point 1 (-0.5,0,0.5) meters, as presented in figure 5.4. Then it will have to move to

point 2, close to the object of interest, at (-0.212,0.446,0.560) meters, oriented downward along the z-axis. Both positions are located between a low constrained space. The main objective will be to identify the best planner to produce a trajectory between two points where there's no obstacle in the middle and no object attached to the end-effector. Two trajectories were interpolated along the *zz* axis to lower the *Eff* to the cube pose, grab it, and than raise it to the original pose. In benchmark 2, after picking up the object, the manipulator executes a trajectory where it must move to point 3, close to the final black base at (0.195,0.459,0.560) meters, dodging the obstacle. Then two descending and ascending segments are carried out again to place the object in the final pose and return to the previous pose, respectively. Finally, in benchmark 3 the manipulator moves again to its initial pose. For this last motion planning problem, the manipulator stars and ends in low constrained spaces. However, it has to bypass the cylinder shape obstacle that is positioned in between.

For the total set of trajectories, only 3 of these effectively need to use the planners since the other 4 (2 ascending and 2 descending) can be obtained through spatial discretization. As these paths are straight along the *zz* axis, the space between the start point and the end point is discretized with a 0.5mm step.

The pick and place operation makes it possible to identify the best planner for three different situations with a different scenario, and therefore different degrees of complexity. Each benchmarking includes 22 different planners from OMPL whose performance was characterized according to the methodology presented in figure 5.5. The 22 OMPL planners are presented in table 2.3. The benchmarking experiments were performed on a system with an Intel i5-10400 2.90GHz processor and 8Gb of memory.

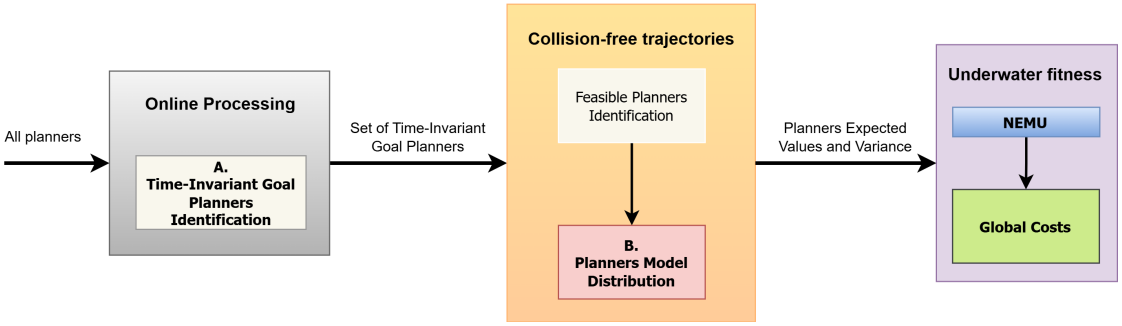

Figure 5.5: Representative diagram of the methodology.

1. Online processing:

Planners were tested above water and without cylinder obstacle to identify the sub-set of planners that are unable to return a solution within a considerable period of time due to the complexity of the problem. This is particularly relevant for planners that do not have a time-invariant goal, since they reach the end of the maximum planning time and they may have not calculated a feasible solution, and therefore they are not suitable for online robotic applications. A time of 120s

was specified to be large enough so that the majority of the non time-invariant goal planners could return a solution.

2. Collision-free trajectories:

After identifying the planners that calculated a solution in less than 120s, the obstacle was added to the environment. The increased complexity is caused by adding restrictions to the problem, making it possible to assess the planners that are unable to produce a collision-free solution in less than 120s. Subsection 5.3.1 presents the list of the planners that will be analyzed underwater.

3. Underwater fitness:

Finnaly, the planners are studied in underwater environment. Subsection 5.3.2 depicts a small study that tries to estimate the normal distribution model of each feature. Underwater tests were performed in a 5x5x1.8 meter indoor freshwater pool equipped with the Qualisys motion capture system [2]. This mocap system allows extracting the real trajectory executed with 2 millimeters accuracy. Using the defined metric, it is intended to demonstrate the costs of effectiveness, safety and adaptability. As described in section 5.2 referring to the characterization of the metric, adaptability is related to the variables responsible for the execution of the motion planning by the real hardware. They are directly correlated with the mechanical characteristics of the manipulator used, such as the accuracy of the joints (0.1°) and their velocity, as well as the control software that was used throughout the experiments. In this way, subsection 5.3.3 presents the cost of effectiveness and safety, while the results related to the last category are separated in subsection 5.3.4.

5.3.1 Time-invariant Goal Planners Identification

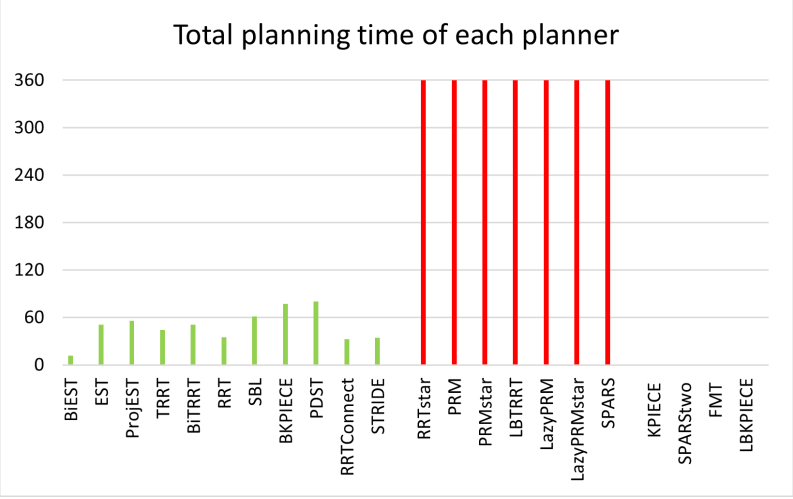

Figure 5.6: Total planning time of each planner for an experience above water and without obstacle.

[2] "Qualisys | MotionCaptureSystems." [Online]. Available: https://www.qualisys.com/

Figure 5.6 shows the total planning time for each planner above water and without obstacle. The figure is divided into 3 parts: The green columns show the times obtained from the time-invariant goal planners, that is, the planners that have not required all the time available to return a feasible trajectory; The red columns show the planners that used 120s in the three benchmarks; KPIECE, SPARStwo, FMT and LBKPIECE are the planners that were unable to return a solution for one of the benchmarks. This may have happened for two reasons: the lack of optimization of the planner parameters and the high complexity of the problem (figure 5.7).

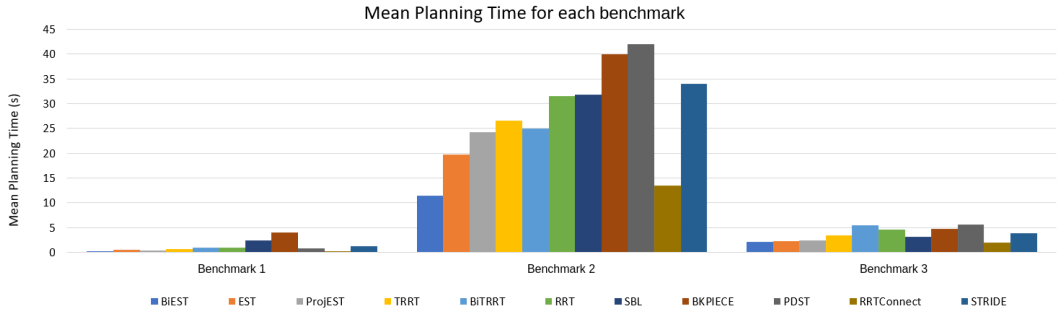

Figure 5.7: Mean planning time for each planner in the different benchmarks.

5.3.2 Planners Model Distribution

After all time-invariant goal planners were identified, its variability is studied. Due to randomization of sampling-based motion planners, all trajectories were computed 20 times to obtain normal distribution models statistically significant. As the objective is to carry out a study of the planners, all trajectories were only calculated in simulation. This study aims to collect information on the expected values and the respective variances of the features. Subsequently, it aims to analyze the confidence level of the solution obtained underwater assigning higher costs to solutions that are considered as outliers.

Through the data obtained, the variation in benchmark 1 is considerably lower than others benchmarks because there is no obstacle in the middle and no object attached to the end-effector. The solutions for benchmark 2 present the greater variance values, caused by the high degree of complexity of the problem. The increase in complexity is explained by not only having to plan a path between configuration extremes, caused by the mechanical characteristics of the manipulator, but also having to avoid an obstacle while having an object attached to the end-effector. The high complexity on benchmark 2 can also be evidenced by the increase of 53.5 times of the computational time planning. Finally, regarding benchmark 3, there was a decrease in the variances analyzed in relation to benchmark 2 and an approximate average increase of 8 times in relation to benchmark 1. The variability reduction of the solutions comes from the smaller complexity of the problem because there is no object attached to the *Eff*.

5.3.3 Planners Analysis in an Underwater Execution

The same experiment described above was carried out in underwater. This test aims to draw conclusions about the planners for trajectories with three levels of complexity. The results are described by benchmark.

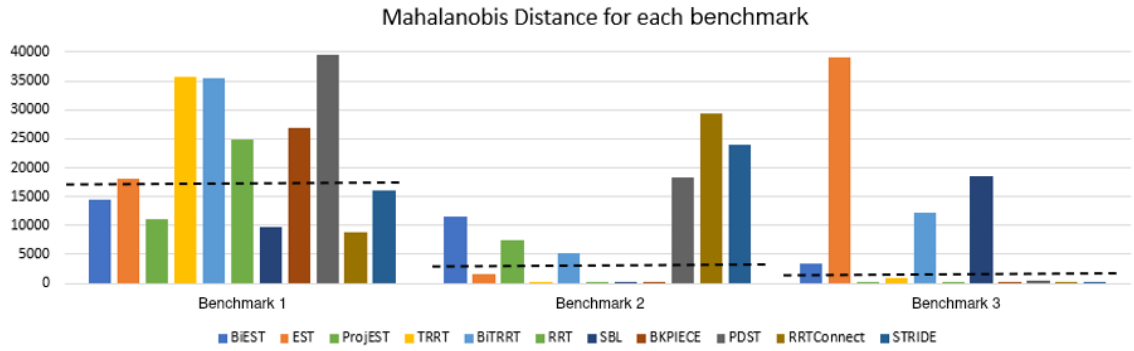

Figure 5.8: Mahalanobis Distance for each benchmark. Values below the dashed line represent inlier planners.

Figure 5.8 depicts the different Mahalanobis distances obtained for each planner in different benchmarks, and the threshold line that was used to define the set of observations that are considered outliers. As previously mentioned, each benchmark has a different level of complexity. In this way, the variance of the solution presented by planners is different due to random considerations that are contemplated while estimating solutions. In this way, the presented metric is able, for each problem, to rescale the error cost depending on the complexity of the problem. Therefore, taking into account that the variances presented by the planners have several orders of magnitude for each benchmark, the variable β was duly adjusted for each problem. The variable β has been defined so that the set of inliner observations of each problem has an influence maximum cost approximately equal to 2.

The Mahalanobis distances were much more uniform in benchmark 1 than in the others, proving the planners' stability in this problem. For the remaining cases, it turns out that 3 planners had a much greater distance than the others, PDST, STRIDE and RRTConnect in benchmark 2 and EST, BiTRRT and SBL in benchmark 3. This means that the experiment carried out with those planners resulted in features far from the expected values. For these cases, the influence cost (φ) will be much higher in order to represent the distrust of the obtained solution.

Benchmark 1

Figures 5.9a and 5.9b present the total cost obtained for each planner in benchmark 1, with and without influence cost. As it is possible to observe by comparing the graphs, the planner that presents the lowest effectiveness cost is the PDST. These graphs present two values for each planner: the costs related to effectiveness, safety and their sum being equivalent to the total cost.

Although the Mahalanobis distance from this planner is greater than the others, its influence cost its not sufficient to increase the planner's cost to values above the others (see figure 5.8).

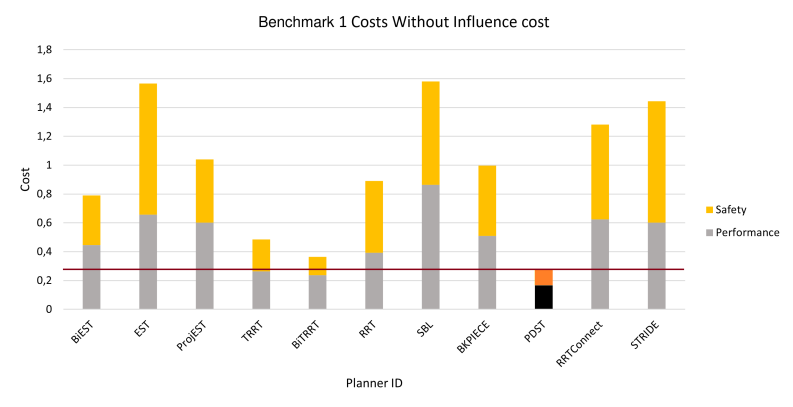

(a)

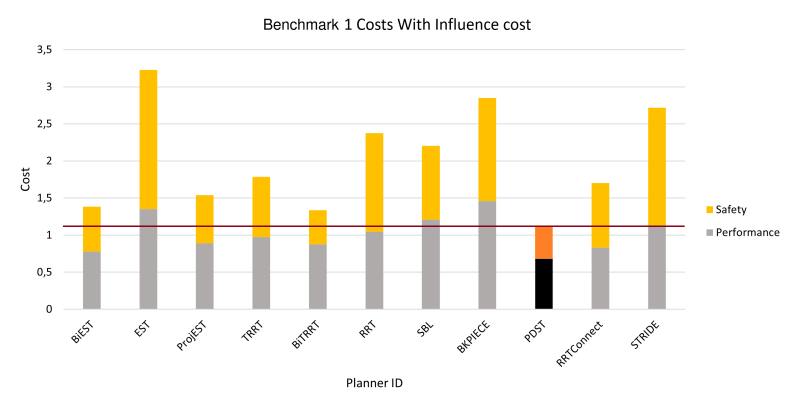

(b)

Figure 5.9: Costs without (a) and considering (b) the Mahalanobis distance in benchmark 1.

Regarding the safety cost of each planner, it was observed that the PDST planner is the safest planner, presenting a trajectory approximately 50% safer than RRTconnect (which was the planner with the lowest mahalanobis distance).

Finally, analyzing the total cost as the sum of the effectiveness and safety of each planner, the planner that presents the lowest cost is the PDST as a result of its good effectiveness and high safety. However, it should be noted that the BiTRRT and BiEST planners also present promising results with just 19% and 23% higher costs, respectively.

Benchmark 2

Figure 5.10 presents the effectiveness and safety costs, considering the influence factor, for planners who were considered as inliers (see figure 5.8). As the remaining of the planners showed higher distance values, the influence cost of these planners is so substantial that its total cost becomes enormously bigger than the others.

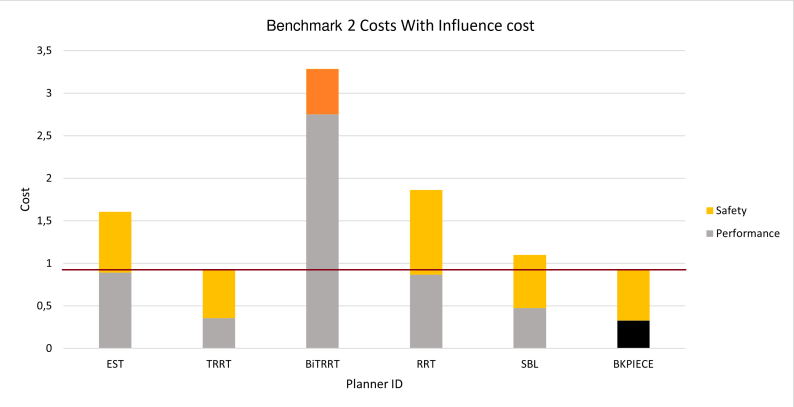

Figure 5.10: Costs considering the influence factor in benchmark 2.

Through the analysis of the graph it is possible to observe that the planner that presented the best cost related to safety was BiTRRT. However, the result obtained from its effectiveness was much higher. As explained, effectiveness is related to the energy used by the manipulator throughout an entire mission. With a high effectiveness cost BiTRRT proves to be much more inefficient than the others.

The planner with the best cost was TRRT, with results similar to BKPIECE. The difference presented by the two was only 0.18%. The SBL planner presents 19% higher costs than TRRT but it was approximately 34% slower to calculate a feasible trajectory and presented a 17% higher safety cost not making it a planner of interest.

Benchmark 3

Benchmark 3 depicts a scenario where an obstacle avoidance operation must be executed without any object attached to the end-effector.

Analysing figure 5.11a it can be observed that, without considering the influence cost, the planner that presented the lowest cost was BiTRRT. However, when considering this factor it makes it the worst of this set.

As explained for the benchmark 2, the graph shown in figure 5.11b only shows the cost of inliner planners obtained in the execution of benchmark 3. From this set it is easily identified that the RRT planner presented the lower cost of effectiveness. Its fast planning time and small movements of each joint allows to justify the choice of this planner by many users of MoveIt!. Its safety cost compared to the others is high. Thus, it is possible to conclude that the planner that presented the lowest cost, both in terms of safety and globally, was the planner STRIDE.

It should be noted that ProjEST, BKPIECE and RRTConnect presented 30% higher costs compared to STRIDE and maximum cost difference between them equal to 0.02. From these 30%, approximately 20% are related to effectiveness and only 10% is related with safety. In this way, these planners are also promising since no adjustment has been made to their parameters.

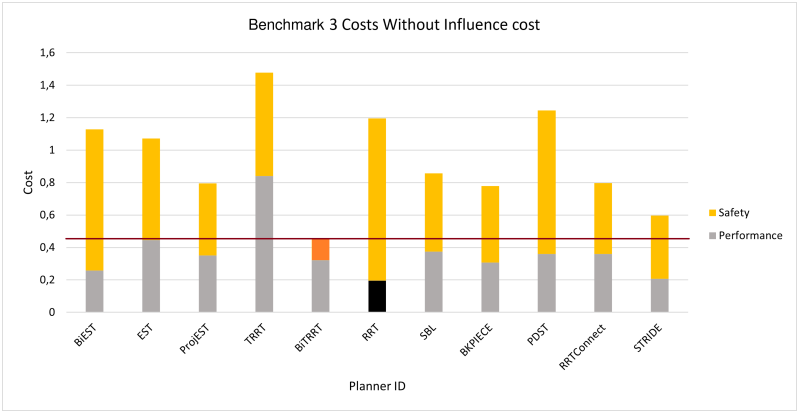

(a)

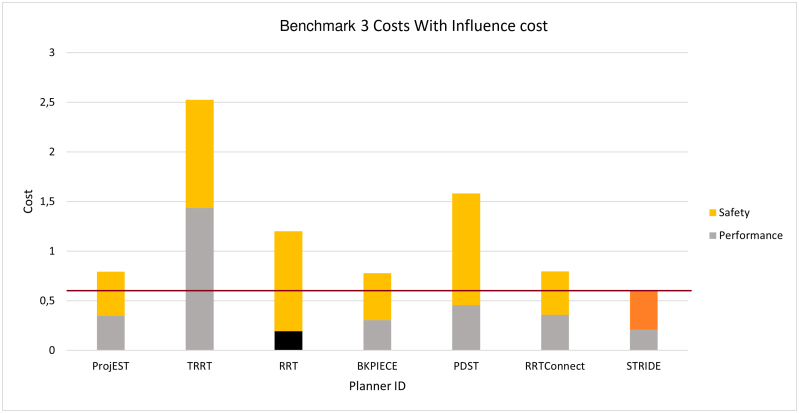

(b)

Figure 5.11: Costs without (a) and considering (b) the Mahalanobis distance in benchmark 3.

5.3.4 Adaptability and Qualitative evaluation

This subsection depicts the adaptability and the global costs of the planners who presented the best effectiveness and safety costs for each benchmark. Next, a qualitative evaluation is showed comparing the trajectories obtained by the motor encoders and those obtained with the Qualisys motion capture system. This comparison will demonstrate not only the high accuracy joint positioning of the manipulator used, but also the quality of the control software used.

Figure 5.12 shows the different adaptability costs of each planner. Features such as the density of points and the distance between them have a huge influence on the cost of this category. Thus, determining the cost of adaptability becomes essential to understand how the manipulator executes the trajectories computed by each planner. High executed position deviations from the *Eff* related to its original plan will result in high adaptability costs.

By looking at figure 5.12a, it is possible to verify that the planner that obtained the best effectiveness and safety cost in benchmark 1, PDST, does not present the best global cost. This is due to the fact that its cost of adaptability was the highest of all planners, almost 6 times higher than BiEST. It can then be concluded that although the cost of effectiveness and safety was higher, the BiEST planner presents the best global cost for the Bravo 7 manipulator, resulting in a trajectory

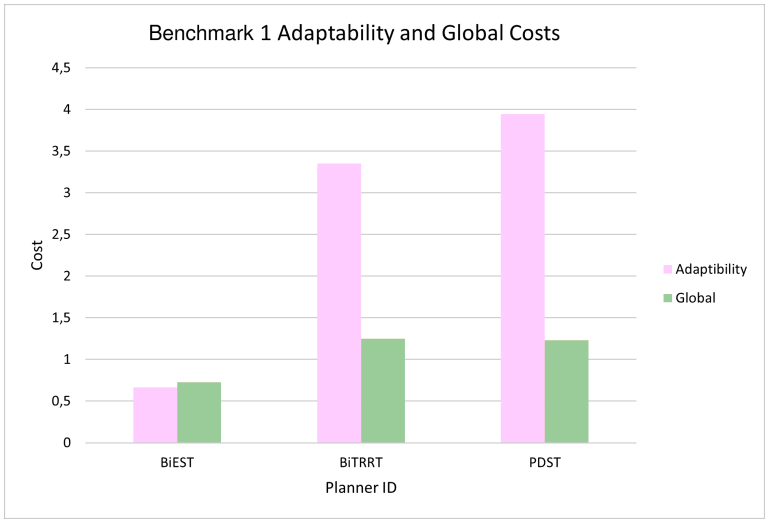

(a)

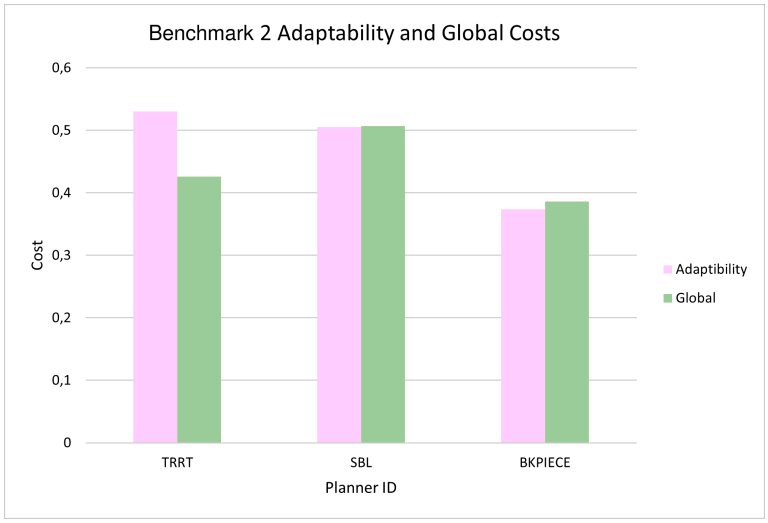

(b)

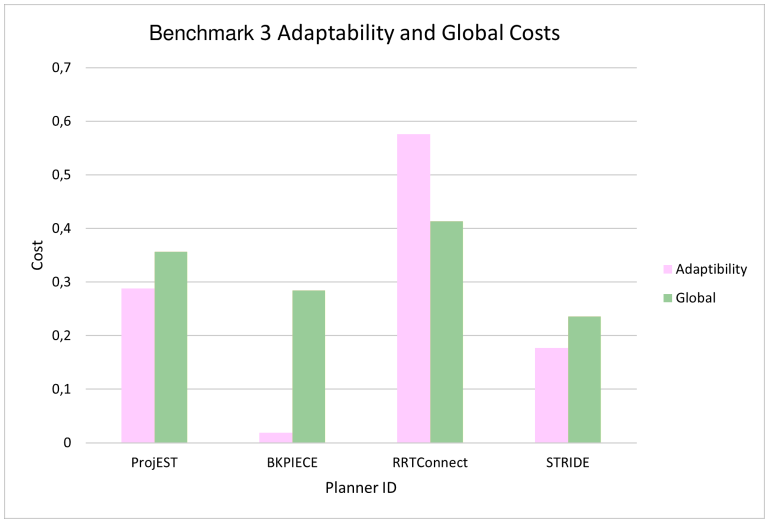

(c)

Figure 5.12: Adaptability and global costs for each benchmark.

executed much more similar to the planned one. As for benchmark 2, analyzing the central graph of figure 5.12b, it appears that this new category allows to differentiate TRRT and BKPIECE planners that previously had a similar cost. Since the TRRT's adaptability cost is 42% higher, this resulted in a 10% difference in the global cost of these planners. It can therefore be concluded that the best planner for the most complex case is BKPIECE according to the metric provided. In benchmark 3, although the BKPIECE planner proved to be the best in terms of adaptability, this was not enough to have the best global cost (see figure 5.12c). Due to the fact that STRIDE has a planning time 10 times faster and returned trajectories with one more centimeter on the minimum distance to the obstacle variable results in lower safety costs than the difference relating to the adaptability.

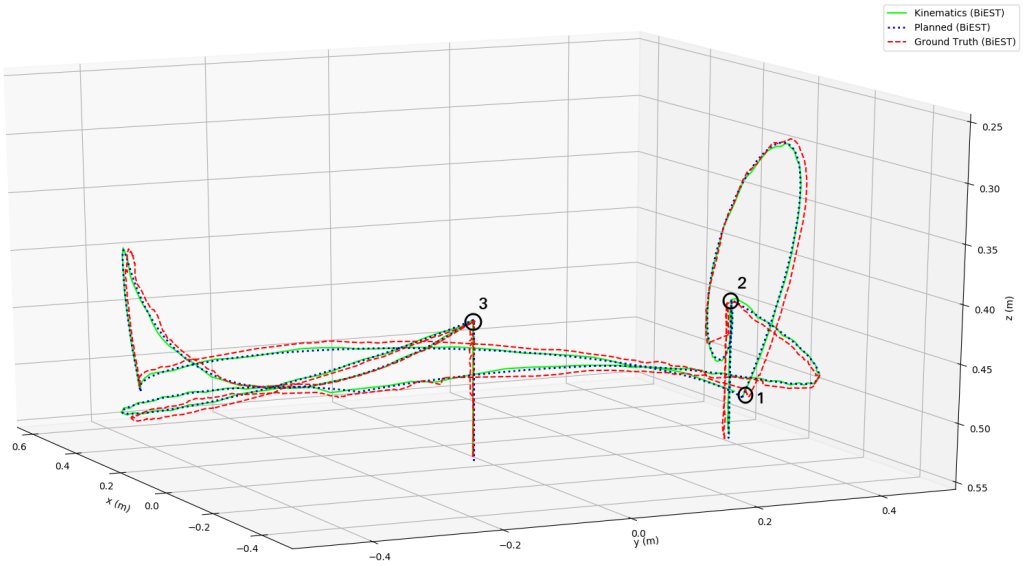

Figure 5.13: Example of a planned path and its executed trajectories. In blue is the planned trajectory, in green the trajectory executed and obtained by the kinematics and in red the Ground Truth obtained with Qualisys motion capture system.

Figure 5.13 presents an example of a planned path using the BiEST algorithm, its execution obtained by the motor encoders and the same path obtained with the Qualisys motion capture system. To obtain the ground truth of the trajectory using the Qualisys system, reflective markers were used. To define a frame, at least 3 markers are needed. During the underwater execution, 4 markers were used to define the frame relative to the metallic structure and 3 markers to define the *Eff* frame. This figure demonstrates not only the quality of the trajectory executed compared to the planned one, but also to prove that both trajectories are in accordance with the result obtained by the Qualisys system. The offset difference, presented by the green trajectory, is due to the imperfection in the transformation between references. The average error of the *Eff* position between the trajectory obtained through the kinematics and the ground truth was 0.0064 ± 0.0023 meters and the standard deviation was 5.43×10^{-5} meters. A video of a single execution can be found in: https://tinyurl.com/bravo7Stride.

5.4 Final Considerations

This chapter presented a new planner evaluation metric, NEMU, advancing the field toward reliable manipulation-based docking capabilities by providing a new approach to assess and select optimal motion planners for underwater operations. NEMU was defined to calculate the cost of planners using multiple heterogeneous data, presenting robustness when dealing with outlier solutions, and it combines three different performance indicators: effectiveness, safety and adaptability of the paths generated by each planner.

Moreover, this chapter presents a benchmark of multiple planners when applied to a 6 DoF configuration manipulator for three underwater scenarios. Extensive experiments have quantified the effectiveness, safety and adaptability costs of planners. These experiments depict a realistic underwater pick and place manipulation and prove that state-of-the-art planners designed to perform well on land can lead to different results when applied to underwater applications. In practice, the behaviour of planners are related to the complexity of the problem. Results show that the BiEST planner has the best global cost for the lowest complexity problem with 40 % less cost than the best effectiveness and safety planner, PDST. In addition, BKPIECE was identified as the best planner for all the designed experience due to its stability and adaptability.

The experiments demonstrated that the presented metric can distinguish the best planner for particular movement restrictions and has the ability to manage with heterogeneous data. Moreover, it identifies the most promising planner for collision-free motion planning, being a valuable contribution for the inspection of maritime structures, as well as for the manipulation procedures of autonomous underwater vehicles during close range operations. This advancement in motion planning evaluation represents a key step toward enabling docking maneuvers based on active manipulation - a fundamental capability for achieving persistent autonomous operations in offshore environments.

Chapter 6

Conclusion

This research presents a bio-inspired AUV design optimized for intervention tasks, created a systematic methodology for underwater structure exploration and reconstruction, and defined a new evaluation metric for underwater manipulation motion planners. Through the integration of these components, this work provides a foundation for more efficient, safer, and more reliable manipulation-based docking capabilities, a critical requirement for achieving long-term autonomous operations.

RAYA, the novel bio-inspired AUV developed in this research, represents a significant advancement in underwater vehicle design. RAYA's innovative approach achieves enhanced capabilities in a more compact and efficient platform. This innovative AUV enhances offshore inspections by overcoming traditional limitations through extended operational endurance, precise maneuverability in constrained spaces, advanced sensor integration for real-time data processing, and improved underwater 3D reconstructions. Its blended wing body morphology, inspired by manta rays enables complex maneuvers in all 6 degrees of freedom needed for close-range inspection and intervention missions. Unlike conventional designs that sacrifice hydrodynamic efficiency for payload capacity, RAYA's strategic thruster configuration and optimized morphology allow for stable hovering and precise manipulation. The vehicle's modular architecture enhances safety and maintainability through independent subsystems. Field trials demonstrated RAYA's capabilities across multiple domains. Perception system validation in reconstruction tasks showed high accuracy with errors below 1.5% in structural dimension estimation. Real-world testing in Porto de Leixões demonstrated autonomous trajectory execution and seabed mapping capabilities, with the vehicle successfully mapping depths between 1.71 and 2.58 meters while maintaining operational stability in varying environmental conditions.

C2FARUS, the coarse-to-fine approach for 3D reconstruction of underwater structures, addresses the challenge of systematically exploring unknown underwater environments to detect specific structures and perform close-range inspection, enabling the creation of high-coverage and accurate 3D representations necessary for manipulation-based autonomous docking. Starting with no prior knowledge of the environment, the methodology processes environmental data through a four-stage process to progressively achieve detailed 3D structural representations. Initially, it per-

forms a coarse exploration of the unknown environment using multibeam sonar to detect potential objects of interest. Following coarse exploration, geometric feature analysis identifies objects of interest, enabling the recognition of specific structures without requiring pre-existing models. Based on this acquired understanding, C2FARUS defines safe inspection zones considering sonar specifications and object dimensions, and finally executes optimized path planning for detailed reconstruction. This progressive refinement approach ensures efficient exploration while continuously improving data quality for subsequent intervention tasks. C2FARUS achieved an 87.04% completeness in the fine reconstruction task. The methodology overcomes the limitations of current exploration approaches, which often rely on ad-hoc solutions or require prior environmental knowledge. By defining navigational zones based on measured structure dimensions and sonar specifications, C2FARUS ensures high quality data acquisition while maintaining vehicle safety. Extensive validation in controlled underwater environments demonstrated the system's accuracy, with a maximum relative error of just 3.22% in object dimension measurements. When benchmarked against state-of-the-art methods, C2FARUS achieved the highest accuracy at 0.0076 meters and lowest time, completing inspection paths in 130 seconds. Furthermore, real-world trials validated the method's capability to segment complex geometries and detect fine-scale components such as anodes, with relative errors below 2.829% for structural dimensions.

Building on the capability to create accurate environmental models, the next challenge in enabling autonomous docking through manipulation lies in achieving reliable motion planning for underwater robotic arms. NEMU, a novel evaluation metric for underwater motion planning, introduces a framework for assessing and selecting optimal planning strategies for underwater intervention tasks. Current evaluation approaches typically analyze individual performance indicators separately, lacking a unified method to assess planners under the specific constraints of underwater operations. NEMU addresses this limitation by integrating three key performance categories: effectiveness (energy efficiency and planning time), safety (obstacle avoidance and path optimization), and adaptability (accuracy of real hardware execution). Through this multi-criteria approach, NEMU enables the quantitative comparison of motion planners while considering the unique challenges of underwater environments, such as manipulator stability and energy constraints. The metric was extensively validated using a 6-DoF manipulator capable of lifting 10kg with high-accuracy joint positioning of 0.1º, testing 22 different planners across varying complexity scenarios. Results revealed distinct optimal planners for different operational conditions: BiEST demonstrated superior performance in low-complexity tasks, achieving 40% lower global costs than the next best alternative (PDST), despite PDST showing better individual effectiveness and safety scores. For complex manipulation scenarios involving obstacle avoidance, BKPIECE emerged as the optimal choice, demonstrating 42% better adaptability than TRRT and achieving a 10% lower global cost. Real-world validation using an underwater motion capture system demonstrated the metric's reliability, with planned trajectories executed with average position errors of 0.0064 ± 0.0023 meters and a standard deviation of 5.43×10^{-5} meters. This thorough validation establishes NEMU as a reliable methodology for selecting motion planners specifically optimized for underwater intervention tasks, providing a foundation for improving the efficiency

and reliability of autonomous underwater operations.

In conclusion, this thesis addressed the challenges of autonomous underwater inspection in offshore structures by introducing innovative solutions across vehicle design, perception, and motion planning. The integration of bio-inspired design principles, systematic inspection methodologies, and robust evaluation frameworks has established a foundation for the next generation of autonomous underwater vehicles capable of performing complex intervention tasks. This research contributes to making offshore operations safer, more efficient, and more cost-effective, particularly in the growing offshore wind energy sector where reliable inspection and maintenance capabilities are crucial for sustainable operations.

6.1 Future Work

Building upon the contributions presented in this thesis, several key research directions have been identified for future development. The RAYA platform can be enhanced through the estimation of the full dynamic model and subsequent implementation of a more robust control algorithm to improve performance in varying underwater conditions. Future work should focus on implementing autonomous docking capabilities and developing compliant control strategies for manipulation tasks. The C2FARUS methodology can be extended by incorporating machine learning techniques, for improved object recognition, and developing methods for handling dynamic environments. From a system integration perspective, future research should address challenges in achieving long-term autonomy, including energy management strategies and fault recovery mechanisms. The development of industry-standard interfaces and safety protocols would facilitate integration with existing offshore infrastructure. Extended validation through comprehensive field trials and long-term deployment studies would further demonstrate the system's reliability in real-world conditions. These developments would collectively advance the capabilities of autonomous underwater vehicles in offshore inspection and maintenance tasks, contributing to more efficient and safer offshore operations.

Bibliography

[1] K. Friedrich and M. Lukas, "Wind energy statistics in europe: Onshore and offshore," in *Springer Proceedings in Energy*, pp. 339–347, Cham: Springer International Publishing, 2017.

[2] G. Costanzo and G. Brindley, "Wind energy in europe: 2023 statistics and the outlook for 2024-2030," tech. rep., WindEurope, 2024.

[3] T. Laskowicz, "Offshore wind energy potential in europe: a forecast of installed capacities and costs," *Eur. XXI*, pp. 129–148, 2022.

[4] M. Hafner and P. P. Raimondi, "Priorities and challenges of the EU energy transition: From the european green package to the new green deal," *Russ. J. Econ.*, vol. 6, pp. 374–389, Dec. 2020.

[5] C. Banet and B. Willems, "Scaling up offshore wind energy in europe," *SSRN Electronic Journal*, 2023.

[6] R. Martin, I. Lazakis, S. Barbouchi, and L. Johanning, "Sensitivity analysis of offshore wind farm operation and maintenance cost and availability," *Renewable Energy*, vol. 85, pp. 1226–1236, Jan. 2016.

[7] E. E. Ambarita, A. Karlsen, O. Osen, and A. Hasan, "Towards fully autonomous floating offshore wind farm operation & maintenance," *Energy Reports*, vol. 9, pp. 103–108, 2023. The 8th International Conference on Sustainable and Renewable Energy Engineering.

[8] F. Jovan and S. Bernardini, "Adaptive temporal planning for multi-robot systems in operations and maintenance of offshore wind farms," *Proceedings of the AAAI Conference on Artificial Intelligence*, vol. 37, p. 15782–15788, June 2023.

[9] T. F. J. Ap, "Robotics and Autonomous Systems in O&M Removing the Barriers to BVLOS Operations," no. January, pp. 1–11, 2019.

[10] M. Fun Sang Cepeda, M. d. S. Freitas Machado, F. H. Sousa Barbosa, D. Santana Souza Moreira, M. J. Legaz Almansa, M. I. Lourenço de Souza, and J.-D. Caprace, "Exploring autonomous and remotely operated vehicles in offshore structure inspections," *J. Mar. Sci. Eng.*, vol. 11, p. 2172, Nov. 2023.

[11] G. Ioannou, N. Forti, L. M. Millefiori, S. Carniel, A. Renga, G. Tomasicchio, S. Binda, and P. Braca, "Underwater inspection and monitoring: Technologies for autonomous operations," *IEEE Aerosp. Electron. Syst. Mag.*, vol. 39, pp. 4–16, May 2024.

[12] A. Hoggarth and J. Carballini, "The evolution of offshore survey technology for pipeline inspections," in *2013 IEEE/OES Acoustics in Underwater Geosciences Symposium*, IEEE, July 2013.

[13] A. G. Rumson, "The application of fully unmanned robotic systems for inspection of subsea pipelines," *Ocean Eng.*, vol. 235, p. 109214, Sept. 2021.

[14] T. Hiller, A. Steingrimsson, and R. Melvin, "Expanding the small AUV mission envelope; longer, deeper & more accurate," in *2012 IEEE/OES Autonomous Underwater Vehicles (AUV)*, IEEE, Sept. 2012.

[15] R. Pi, P. Cieślak, J. Esteba, N. Palomeras, and P. Ridao, "Compliant manipulation with quasi-rigid docking for underwater structure inspection," *IEEE Access*, vol. 11, pp. 128957–128969, 2023.

[16] F. Nauert and P. Kampmann, "Inspection and maintenance of industrial infrastructure with autonomous underwater robots," *Frontiers in Robotics and AI*, vol. 10, Aug. 2023.

[17] P. Ridao, M. Carreras, D. Ribas, P. J. Sanz, and G. Oliver, "Intervention auvs: The next challenge," *Annual Reviews in Control*, vol. 40, p. 227–241, 2015.

[18] K. Alam, T. Ray, and S. G. Anavatti, "Design and construction of an autonomous underwater vehicle," *Neurocomputing*, vol. 142, p. 16–29, Oct. 2014.

[19] P. Kodati and X. Deng, "Towards the body shape design of a hydrodynamically stable robotic boxfish," in *2006 IEEE/RSJ International Conference on Intelligent Robots and Systems*, p. 5412–5417, IEEE, Oct. 2006.

[20] J. E. Manley, S. Halpin, N. Radford, and M. Ondler, "Aquanaut: A new tool for subsea inspection and intervention," in *OCEANS 2018 MTS/IEEE Charleston*, pp. 1–4, 2018.

[21] S. Bauk, N. Kapidani, J.-P. Boisgard, and Ž. Lukšić, "Key features of the autonomous underwater vehicles for marine surveillance missions," in *The 1st International Conference on Maritime Education and Development* (S. Bauk and S. D. Ilčev, eds.), (Cham), pp. 69–82, Springer International Publishing, 2021.

[22] J. Evans, P. Redmond, C. Plakas, K. Hamilton, and D. Lane, "Autonomous docking for intervention-auvs using sonar and video-based real-time 3d pose estimation," in *Oceans 2003. Celebrating the Past ... Teaming Toward the Future (IEEE Cat. No.03CH37492)*, vol. 4, pp. 2201–2210 Vol.4, 2003.

[23] Y. Wang, W. Zhou, M. Fei, and H. Yan, "An unmanned surface vehicle for the launch and recovery of autonomous underwater vehicles: A novel design," *IEEE Robotics & Automation Magazine*, vol. 31, no. 1, pp. 53–61, 2024.

[24] J. Signor, F. Schoefs, N. Quillien, and G. Damblans, "Automatic classification of biofouling images from offshore renewable energy structures using deep learning," *Ocean Engineering*, vol. 288, p. 115928, 2023.

[25] M. Dziura, T. Wiese, and J. Harder, "3d reconstruction in orbital proximity operations," in *2017 IEEE Aerospace Conference*, p. 1–10, IEEE, Mar. 2017.

[26] A. Yazdani, K. Sammut, O. Yakimenko, and A. Lammas, "A survey of underwater docking guidance systems," *Robotics and Autonomous Systems*, vol. 124, p. 103382, 2020.

[27] A. Bucci, A. Ridolfi, and B. Allotta, "Pose-graph underwater simultaneous localization and mapping for autonomous monitoring and 3d reconstruction by means of optical and acoustic sensors," *Journal of Field Robotics*, June 2024.

[28] B. Kim, J. Kim, H. Cho, J. Kim, and S. Yu, "Auv-based multi-view scanning method for 3-d reconstruction of underwater object using forward scan sonar," *IEEE Sensors Journal*, vol. 20, no. 3, pp. 1592–1606, 2020.

[29] Y. Kim, H. Lee, C. Park, and S. Choi, "A study for optimum survey method of underwater structure using the dual sonar sensor," *Journal of Sensors*, vol. 2017, p. 1–10, 2017.

[30] ATLANTIS, "Survey on legal and regulatory specifications for imr robots operating in offshore wind farms," 2020.

[31] S. Sheng, J. Fields, A. Cooperman, and M. Shields, "Wind plant operations and maintenance challenges and research opportunities," 2022.

[32] Y. Wang and Q. Deng, "Optimization of maintenance scheme for offshore wind turbines considering time windows based on hybrid ant colony algorithm," *Ocean Engineering*, vol. 263, p. 112357, 2022.

[33] X. Wu, Y. Hu, Y. Li, J. Yang, L. Duan, T. Wang, T. Adcock, Z. Jiang, Z. Gao, Z. Lin, A. Borthwick, and S. Liao, "Foundations of offshore wind turbines: A review," *Renewable and Sustainable Energy Reviews*, vol. 104, pp. 379–393, 2019.

[34] S. J. Price and R. B. Figueira, "Corrosion protection systems and fatigue corrosion in offshore wind structures: Current status and future perspectives," *Coatings*, vol. 7, no. 2, 2017.

[35] H. Zhu, Z. Du, and Y. Tang, "Automatic free span assessment for subsea pipelines using static strain data," *Ocean Engineering*, vol. 263, p. 112413, 2022.

[36] J. Lux, M. Olschewski, P. Schäfer, and W. Hill, "Real-time determination of depth of burial profiles for submarine power cables," *IEEE Transactions on Power Delivery*, vol. 34, pp. 1079–1086, 2019.

[37] J. Chambel, T. Fazeres-Ferradosa, F. Miranda, A. Bento, F. Taveira-Pinto, and P. Lomonaco, "A comprehensive review on scour and scour protections for complex bottom-fixed offshore and marine renewable energy foundations," *Ocean Engineering*, vol. 304, p. 117829, 2024.

[38] D. Campos, *Multi-domain Contextual Awareness using Unmanned Surface Vehicles for Offshore Wind Farms Inspection*. Phd thesis, University of Porto, October 2024. Available at `https://hdl.handle.net/10216/161860`.

[39] D. F. Campos, A. Matos, and A. M. Pinto, "Multi-domain inspection of offshore wind farms using an autonomous surface vehicle," *SN Applied Sciences*, vol. 3, Mar. 2021.

[40] D. Curto, V. Franzitta, and A. Guercio, "Sea wave energy. a review of the current technologies and perspectives," *Energies*, vol. 14, p. 6604, Oct. 2021.

[41] M. Jacobi, "Autonomous inspection of underwater structures," *Robotics and Autonomous Systems*, vol. 67, pp. 80–86, 2015. Advances in Autonomous Underwater Robotics.

[42] M. Kokegei, F. He, and K. Sammut, "Fully coupled 6 degree-of-freedom control of an over-actuated autonomous underwater vehicle," in *Autonomous Underwater Vehicles* (N. A. Cruz, ed.), ch. 7, Rijeka: IntechOpen, 2011.

[43] T. Ma, Y. Li, R. Wang, Z. Cong, and Y. Gong, "Auv robust bathymetric simultaneous localization and mapping," *Ocean Engineering*, vol. 166, pp. 336–349, 2018.

[44] P. E. Hagen, N. Størkersen, K. Vestgård, P. Kartvedt, and G. Sten, "Operational military use of the hugin auv in norway," *Proc. UDT Europe*, vol. 2003, pp. 123–130, 2003.

[45] Y. Zhao, X. Shang, E. Zhao, X. Deng, Z. Wang, and J. He, "Automatic detection algorithm of mine detection based on improved yolov5 in complex underwater environment for auv," in *2022 5th International Symposium on Autonomous Systems (ISAS)*, pp. 1–6, 2022.

[46] P. Ramos, N. Cruz, A. Matos, M. Neves, and F. Pereira, "Monitoring an ocean outfall using an auv," in *MTS/IEEE Oceans 2001. An Ocean Odyssey. Conference Proceedings (IEEE Cat. No.01CH37295)*, vol. 3, pp. 2009–2014 vol.3, 2001.

[47] A. Inzartsev, G. Eliseenko, M. Panin, A. Pavin, V. Bobkov, and M. Morozov, "Underwater pipeline inspection method for auv based on laser line recognition: simulation results," in *2019 IEEE Underwater Technology (UT)*, pp. 1–8, 2019.

[48] C. Deutsch, A. Chiche, S. Bhat, C. Lagergren, G. Lindbergh, and J. Kuttenkeuler, "Evaluation of energy management strategies for fuel cell/battery-powered underwater vehicles against field trial data," *Energy Conversion and Management: X*, vol. 14, p. 100193, 2022.

[49] Huntington Ingalls Industries, *REMUS 100E - Unmanned Underwater Vehicle*, 11 2022. Available at `https://bluezonegroup.com.au/wp-content/uploads/2022/08/REMUS-100E-3-31-22_web.pdf`.

[50] A. J. Shafer, M. R. Benjamin, J. J. Leonard, and J. Curcio, "Autonomous cooperation of heterogeneous platforms for sea-based search tasks," in *OCEANS 2008*, pp. 1–10, 2008.

[51] L3Harris Technologies, Inc., *Iver4 900 UUV Spec Sheet*, 11 2022. Available at `https://www.l3harris.com/sites/default/files/2022-11/ims-maritime-asv-Iver4-900-Spec-Sheet-Nov-2022.pdf`.

[52] R. Marthiniussen, K. Vestgard, R. Klepaker, and N. Storkersen, "Hugin-auv concept and operational experiences to date," in *Oceans '04 MTS/IEEE Techno-Ocean '04 (IEEE Cat. No.04CH37600)*, vol. 2, pp. 846–850 Vol.2, 2004.

[53] Ø. Hegrenæs, K. Gade, O. K. Hagen, and P. E. Hagen, "Underwater transponder positioning and navigation of autonomous underwater vehicles," in *OCEANS 2009*, pp. 1–7, 2009.

[54] M. Ludvigsen, S. M. Albrektsen, K. Cisek, T. A. Johansen, P. Norgren, R. Skjetne, A. Zolich, P. Sousa Dias, S. Ferreira, J. B. de Sousa, T. O. Fossum, Ø. Sture, T. Røbekk Krogstad, Ø. Midtgaard, V. Hovstein, and E. Vågsholm, "Network of heterogeneous autonomous vehicles for marine research and management," in *OCEANS 2016 MTS/IEEE Monterey*, pp. 1–7, 2016.

[55] B. Jalving, K. Gade, O. K. Hagen, and K. Vestgård, "A toolbox of aiding techniques for the hugin auv integrated inertial navigation system," *Modeling, Identification and Control: A Norwegian Research Bulletin*, vol. 25, no. 3, p. 173–190, 2004.

[56] C. von Alt, "Remus 100 transportable mine countermeasure package," in *Oceans 2003. Celebrating the Past ... Teaming Toward the Future (IEEE Cat. No.03CH37492)*, vol. 4, pp. 1925–1930 Vol.4, 2003.

[57] E. Gallimore, E. Terrill, R. Hess, A. Nager, H. Bachelor, and A. Pietruszka, "Integration and evaluation of a next-generation chirp-style sidescan sonar on the remus 100," in *2018 IEEE/OES Autonomous Underwater Vehicle Workshop (AUV)*, pp. 1–6, 2018.

[58] A. J. Plueddemann, G. Packard, J. Lord, and S. Whelan, "Observing arctic coastal hydrography using the remus auv," in *2008 IEEE/OES Autonomous Underwater Vehicles*, pp. 1–4, 2008.

[59] E. I. Sarda and M. R. Dhanak, "A usv-based automated launch and recovery system for auvs," *IEEE Journal of Oceanic Engineering*, vol. 42, no. 1, pp. 37–55, 2017.

[60] P. K. LeHardy and C. Moore, "Deep ocean search for malaysia airlines flight 370," in *2014 Oceans - St. John's*, pp. 1–4, 2014.

[61] M. Pfingsthorn, R. Rathnam, T. Luczynski, and A. Birk, "Full 3d navigation correction using low frequency visual tracking with a stereo camera," in *OCEANS 2016 - Shanghai*, pp. 1–6, 2016.

[62] C. Eriksen, T. Osse, R. Light, T. Wen, T. Lehman, P. Sabin, J. Ballard, and A. Chiodi, "Seaglider: a long-range autonomous underwater vehicle for oceanographic research," *IEEE Journal of Oceanic Engineering*, vol. 26, no. 4, pp. 424–436, 2001.

[63] W. Snyder, L. V. Uffelen, and M. Renken, "Effects of incorporating inertial measurements on the localization accuracy of the seaglider auv," in *OCEANS 2019 - Marseille*, pp. 1–6, 2019.

[64] H. C. Brown and J. Rodocker, "Cooperative underwater survey with an l3harris iver uuv and strategic robotic systems fusion rov," in *OCEANS 2019 MTS/IEEE SEATTLE*, pp. 1–5, 2019.

[65] E. Simetti, G. Casalino, S. Torelli, A. Sperindé, and A. Turetta, "Floating underwater manipulation: Developed control methodology and experimental validation within the trident project," *Journal of Field Robotics*, vol. 31, no. 3, pp. 364–385, 2014.

[66] F. Bonin-Font, G. Oliver, S. Wirth, M. Massot, P. Lluis Negre, and J.-P. Beltran, "Visual sensing for autonomous underwater exploration and intervention tasks," *Ocean Engineering*, vol. 93, pp. 25–44, 2015.

[67] P. Cieslak, P. Ridao, and M. Giergiel, "Autonomous underwater panel operation by girona 500 uvms: A practical approach to autonomous underwater manipulation," in *2015 IEEE International Conference on Robotics and Automation (ICRA)*, pp. 529–536, 2015.

[68] P. Cieślak, R. Simoni, P. Ridao Rodríguez, and D. Youakim, "Practical formulation of obstacle avoidance in the task-priority framework for use in robotic inspection and intervention scenarios," *Robotics and Autonomous Systems*, vol. 124, p. 103396, 2020.

[69] S. Heshmati-Alamdari, C. P. Bechlioulis, G. C. Karras, A. Nikou, D. V. Dimarogonas, and K. J. Kyriakopoulos, "A robust interaction control approach for underwater vehicle manipulator systems," *Annual Reviews in Control*, vol. 46, pp. 315–325, 2018.

[70] C. Barbalata, M. W. Dunnigan, and Y. Petillot, "Position/force operational space control for underwater manipulation," *Robotics and Autonomous Systems*, vol. 100, pp. 150–159, 2018.

[71] S. Heshmati-Alamdari, G. C. Karras, and K. J. Kyriakopoulos, "A distributed predictive control approach for cooperative manipulation of multiple underwater vehicle manipulator systems," 2019.

[72] D. Mitchell, J. Blanche, S. Harper, T. Lim, R. Gupta, O. Zaki, W. Tang, V. Robu, S. Watson, and D. Flynn, "A review: Challenges and opportunities for artificial intelligence and robotics in the offshore wind sector," *Energy and AI*, p. 100146, 2022. doi: 10.1016/j.egyai.2022.100146.

[73] S. Choi, G. Takashige, and J. Yuh, "Experimental study on an underwater robotic vehicle: Odin," in *Proceedings of IEEE Symposium on Autonomous Underwater Vehicle Technology (AUV'94)*, AUV-94, p. 79–84, IEEE, 1994.

[74] D. M. Lane, J. B. C. Davies, G. Casalino, G. Bartolini, G. Cannata, G. Veruggio, M. Canals, C. Smith, D. J. O'Brien, M. Pickett, *et al.*, "Amadeus: advanced manipulation for deep underwater sampling," *IEEE Robotics & Automation Magazine*, vol. 4, no. 4, pp. 34–45, 1997. doi: 10.1109/100.637804.

[75] K. Hamilton and J. Evans, "Subsea pilotless inspection using an autonomous underwater vehicle (spinav): concepts and results," *Europe Oceans 2005*, vol. 2, pp. 775–781, 2005. doi: 10.1109/OCEANSE.2005.1513154.

[76] G. Marani and J. Yuh, *Introduction to Autonomous Manipulation: Case Study with an Underwater Robot, SAUVIM*. Springer Berlin Heidelberg, 2014.

[77] L. Lionel, "Underwater robots part I: Current systems and problem pose," in *Mobile Robots* (A. Lazinica, ed.), ch. 16, Rijeka: IntechOpen, 2006.

[78] O. Khatib, X. Yeh, G. Brantner, B. Soe, B. Kim, S. Ganguly, H. Stuart, S. Wang, M. Cutkosky, A. Edsinger, P. Mullins, M. Barham, C. R. Voolstra, K. N. Salama, M. L'Hour, and V. Creuze, "Ocean one: A robotic avatar for oceanic discovery," *IEEE Robotics & Automation Magazine*, vol. 23, no. 4, pp. 20–29, 2016.

[79] J. Yuh, S. Choi, C. Ikehara, G. Kim, G. McMurty, M. Ghasemi-Nejhad, N. Sarkar, and K. Sugihara, "Design of a semi-autonomous underwater vehicle for intervention missions (sauvim)," in *Proceedings of 1998 International Symposium on Underwater Technology*, UT-98, p. 63–68, IEEE, 1998.

[80] D. Ribas, P. Ridao, L. Magi, N. Palomeras, and M. Carreras, "The girona 500, a multipurpose autonomous underwater vehicle," in *OCEANS 2011 IEEE - Spain*, p. 1–5, IEEE, June 2011.

[81] M. Carreras, A. Gori, A. Mallios, N. Palomeras, C. Linares, J. M. Gili, D. Ribas Romagos, N. Hurtós, L. Magí, and P. Ridao, "Seabed monitoring with girona 500 auv working as hrov," in *Instrumentation viewpoint*, pp. 65–66, SARTI, 2016.

[82] P. Cieślak and P. Ridao, "Adaptive admittance control in task-priority framework for contact force control in autonomous underwater floating manipulation," in *2018 IEEE/RSJ International Conference on Intelligent Robots and Systems (IROS)*, pp. 6646–6651, IEEE, 2018. doi: 10.1109/IROS.2018.8593542.

[83] D. Ribas, N. Palomeras, P. Ridao, M. Carreras, and A. Mallios, "Girona 500 auv: From survey to intervention," *IEEE/ASME Transactions on Mechatronics*, vol. 17, no. 1, pp. 46–53, 2012.

[84] S. Mitra, V. Sehgal, S. Rathore, R. Puri, S. Chouhan, and A. Sharma, "Design and control strategy of bio-inspired underwater vehicle with flexible propulsor," *Journal of Modern Mechanical Engineering and Technology*, vol. 8, pp. 57–65, 2021. doi: 10.31875/2409-9848.2021.08.7.

[85] J. McColgan and E. W. McGookin, "Coordination of multiple biomimetic autonomous underwater vehicles using strategies based on the schooling behaviour of fish," *Robotics*, vol. 5, no. 1, p. 2, 2016. doi: 10.3390/robotics5010002.

[86] W. Gorma, M. A. Post, J. White, J. Gardner, Y. Luo, J. Kim, P. D. Mitchell, N. Morozs, M. Wright, and Q. Xiao, "Development of modular bio-inspired autonomous underwater vehicle for close subsea asset inspection," *Applied Sciences*, vol. 11, no. 12, p. 5401, 2021. doi: 10.3390/app11125401.

[87] M. Marcin, S. Adam, Z. Jerzy, and M. Marcin, "Fish-like shaped robot for underwater surveillance and reconnaissance–hull design and study of drag and noise," *Ocean Engineering*, vol. 217, p. 107889, 2020. doi: 10.1016/j.oceaneng.2020.107889.

[88] G. Liu, Y. Ren, J. Zhu, H. Bart-Smith, and H. Dong, "Thrust producing mechanisms in ray-inspired underwater vehicle propulsion," *Theoretical and Applied mechanics letters*, vol. 5, no. 1, pp. 54–57, 2015. doi: 10.1016/j.taml.2014.12.004.

[89] A. Bircher, K. Alexis, M. Burri, P. Oettershagen, S. Omari, T. Mantel, and R. Siegwart, "Structural inspection path planning via iterative viewpoint resampling with application to aerial robotics," in *2015 IEEE International Conference on Robotics and Automation (ICRA)*, pp. 6423–6430, 2015.

[90] R. M. Claro, M. I. Pereira, F. S. Neves, and A. M. Pinto, "Energy efficient path planning for 3d aerial inspections," *IEEE Access*, vol. 11, pp. 32152–32166, 2023.

[91] C. Connolly, "The determination of next best views," in *Proceedings. 1985 IEEE International Conference on Robotics and Automation*, vol. 2, pp. 432–435, 1985.

[92] R. Pito, "A sensor-based solution to the "next best view" problem," in *Proceedings of 13th International Conference on Pattern Recognition*, vol. 1, pp. 941–945 vol.1, 1996.

[93] S. Kriegel, C. Rink, T. Bodenmüller, and M. Suppa, "Efficient next-best-scan planning for autonomous 3d surface reconstruction of unknown objects," *Journal of Real-Time Image Processing*, vol. 10, p. 611–631, Dec. 2013.

[94] G. Hardouin, F. Morbidi, J. Moras, J. Marzat, and E. M. Mouaddib, "Surface-driven next-best-view planning for exploration of large-scale 3d environments," *IFAC-PapersOnLine*, vol. 53, no. 2, pp. 15501–15507, 2020. 21st IFAC World Congress.

[95] G. Hardouin, J. Moras, F. Morbidi, J. Marzat, and E. M. Mouaddib, "Next-best-view planning for surface reconstruction of large-scale 3d environments with multiple uavs," in *2020 IEEE/RSJ International Conference on Intelligent Robots and Systems (IROS)*, pp. 1567–1574, 2020.

[96] S. Song, D. Kim, and S. Choi, "View path planning via online multiview stereo for 3-d modeling of large-scale structures," *IEEE Transactions on Robotics*, vol. 38, no. 1, pp. 372–390, 2022.

[97] M. Zhang, C. Feng, Z. Li, G. Zheng, Y. Luo, Z. Wang, J. Zhou, S. Shen, and B. Zhou, "Soar: Simultaneous exploration and photographing with heterogeneous uavs for fast autonomous reconstruction," in *2024 IEEE/RSJ International Conference on Intelligent Robots and Systems (IROS)*, pp. 10975–10982, 2024.

[98] A. Palomer, P. Ridao, D. Youakim, D. Ribas, J. Forest, and Y. Petillot, "3d laser scanner for underwater manipulation," *Sensors*, vol. 18, p. 1086, Apr. 2018.

[99] J. Han and J. Kim, "Three-dimensional reconstruction of a marine floating structure with an unmanned surface vessel," *IEEE Journal of Oceanic Engineering*, vol. 44, p. 984–996, Oct. 2019.

[100] J. Fan, Y. Ou, X. Li, C. Zhou, and Z. Hou, "Structured light vision based pipeline tracking and 3d reconstruction method for underwater vehicle," *IEEE Transactions on Intelligent Vehicles*, vol. 9, p. 3372–3383, Feb. 2024.

[101] T. Guerneve, K. Subr, and Y. Petillot, "Three-dimensional reconstruction of underwater objects using wide-aperture imaging sonar," *Journal of Field Robotics*, vol. 35, p. 890–905, Mar. 2018.

[102] J. Wu, B. Yu, and M. J. Islam, "3d reconstruction of underwater scenes using nonlinear domain projection," in *2023 IEEE Conference on Artificial Intelligence (CAI)*, pp. 359–361, 2023.

[103] K. Pathak, A. Birk, and N. Vaskevicius, "Plane-based registration of sonar data for underwater 3d mapping," in *2010 IEEE/RSJ International Conference on Intelligent Robots and Systems*, pp. 4880–4885, 2010.

[104] Y. Petillot, I. Tena Ruiz, and D. M. Lane, "Underwater vehicle obstacle avoidance and path planning using a multi-beam forward looking sonar," *IEEE Journal of Oceanic Engineering*, vol. 26, no. 2, pp. 240–251, 2001.

[105] P. N. Leite and A. M. Pinto, "Fusing heterogeneous tri-dimensional information for reconstructing submerged structures in harsh sub-sea environments," *Information Fusion*, vol. 103, p. 102126, 2024.

[106] A. M. Pinto and A. C. Matos, "Maresye: A hybrid imaging system for underwater robotic applications," *Information Fusion*, vol. 55, pp. 16–29, 2020.

[107] J. A. Smith, "Doppler sonar and surface waves: Range and resolution," *Journal of Atmospheric and Oceanic Technology*, vol. 6, p. 680–696, Aug. 1989.

[108] K. Westley, R. Quinn, W. Forsythe, R. Plets, T. Bell, S. Benetti, F. McGrath, and R. Robinson, "Mapping submerged landscapes using multibeam bathymetric data: a case study from the north coast of ireland," *International Journal of Nautical Archaeology*, vol. 40, p. 99–112, Feb. 2011.

[109] D. Zhao, H. Zhou, P. Chen, Y. Hu, W. Ge, Y. Dang, and R. Liang, "Design of forward-looking sonar system for real-time image segmentation with light multiscale attention net," *IEEE Transactions on Instrumentation and Measurement*, vol. 73, pp. 1–17, 2024.

[110] J. Li, M. Kaess, R. M. Eustice, and M. Johnson-Roberson, "Pose-graph slam using forward-looking sonar," *IEEE Robotics and Automation Letters*, vol. 3, no. 3, pp. 2330–2337, 2018.

[111] E. Vidal, J. D. Hernández, K. Istenič, and M. Carreras, "Online view planning for inspecting unexplored underwater structures," *IEEE Robotics and Automation Letters*, vol. 2, no. 3, pp. 1436–1443, 2017.

[112] E. Galceran and M. Carreras, "A survey on coverage path planning for robotics," *Robotics and Autonomous Systems*, vol. 61, no. 12, pp. 1258–1276, 2013.

[113] H. M. Choset, K. M. Lynch, S. Hutchinson, G. A. Kantor, W. Burgard, L. E. Kavraki, and S. Thrun, *Principles of robot motion*. Intelligent Robotics and Autonomous Agents series, Cambridge, MA: Bradford Books, May 2005.

[114] J. D. Tucker, W. Wu, and A. Srivastava, "Analysis of signals under compositional noise with applications to sonar data," *IEEE Journal of Oceanic Engineering*, vol. 39, no. 2, pp. 318–330, 2014.

[115] M. Yu, J. Zhou, Y. Tang, J. Xiao, M. Luo, and B. Zhou, "Time-efficient autonomous exploration in unknown environment by multirepresentation strategy," *IEEE Sensors Journal*, vol. 24, no. 17, pp. 28427–28440, 2024.

[116] E. Galceran and M. Carreras, "Efficient seabed coverage path planning for asvs and auvs," in *2012 IEEE/RSJ International Conference on Intelligent Robots and Systems*, pp. 88–93, 2012.

[117] L. Paull, S. Saeedi, H. Li, and V. Myers, "An information gain based adaptive path planning method for an autonomous underwater vehicle using sidescan sonar," in *2010 IEEE International Conference on Automation Science and Engineering*, pp. 835–840, 2010.

[118] L. Paull, S. SaeediGharahbolagh, M. Seto, and H. Li, "Sensor driven online coverage planning for autonomous underwater vehicles," in *2012 IEEE/RSJ International Conference on Intelligent Robots and Systems*, pp. 2875–2880, 2012.

[119] N. Palomeras, N. Hurtós, M. Carreras, and P. Ridao, "Autonomous mapping of underwater 3-d structures: From view planning to execution," *IEEE Robotics and Automation Letters*, vol. 3, no. 3, pp. 1965–1971, 2018.

[120] F. Amigoni, A. Q. Li, and D. Holz, "Evaluating the impact of perception and decision timing on autonomous robotic exploration," in *2013 European Conference on Mobile Robots*, pp. 68–73, 2013.

[121] E. Vidal, N. Palomeras, K. Istenič, N. Gracias, and M. Carreras, "Multisensor online 3d view planning for autonomous underwater exploration," *Journal of Field Robotics*, vol. 37, p. 1123–1147, May 2020.

[122] N. Palomeras, N. Hurtós, E. Vidal, and M. Carreras, "Autonomous exploration of complex underwater environments using a probabilistic next-best-view planner," *IEEE Robotics and Automation Letters*, vol. 4, no. 2, pp. 1619–1625, 2019.

[123] N. Hurtós, N. Palomeras, A. Carrera, and M. Carreras, "Autonomous detection, following and mapping of an underwater chain using sonar," *Ocean Engineering*, vol. 130, pp. 336–350, 2017.

[124] S. Sivčev, J. Coleman, E. Omerdić, G. Dooly, and D. Toal, "Underwater manipulators: A review," *Ocean Engineering*, vol. 163, pp. 431–450, 2018.

[125] H. Tugal, K. Cetin, Y. Petillot, M. Dunnigan, and M. S. Erden, "Contact-based object inspection with mobile manipulators at near-optimal base locations," *Robotics and Autonomous Systems*, vol. 161, p. 104345, 2023.

[126] R. D. Christ and R. L. Wernli, Sr, "The ROV business," in *The ROV Manual*, pp. 3–20, Elsevier, 2014.

[127] J. Long, Y. Tian, W. Chen, J. Leng, and Y. Wang, "Locating, trajectory planning and control of an underwater propeller cleaning manipulator," *Ocean Engineering*, vol. 243, p. 110262, 2022.

[128] M. Cai, Y. Wang, S. Wang, R. Wang, Y. Ren, and M. Tan, "Grasping marine products with hybrid-driven underwater vehicle-manipulator system," *IEEE Transactions on Automation Science and Engineering*, vol. 17, no. 3, pp. 1443–1454, 2020.

[129] D. Di Vito, D. De Palma, E. Simetti, G. Indiveri, and G. Antonelli, "Experimental validation of the modeling and control of a multibody underwater vehicle manipulator system for sea mining exploration," *Journal of Field Robotics*, vol. 38, p. 171–191, Aug. 2020.

[130] J. Mao, G. Song, S. Hao, M. Zhang, and A. Song, "Development of a lightweight underwater manipulator for delicate structural repair operations," *IEEE Robotics and Automation Letters*, vol. 8, no. 10, pp. 6563–6570, 2023.

[131] B. T. Phillips, K. P. Becker, S. Kurumaya, K. C. Galloway, G. Whittredge, D. M. Vogt, C. B. Teeple, M. H. Rosen, V. A. Pieribone, D. F. Gruber, and R. J. Wood, "A dexterous, glove-based teleoperable low-power soft robotic arm for delicate deep-sea biological exploration," *Scientific Reports*, vol. 8, Oct. 2018.

[132] Z. Shen, H. Zhong, E. Xu, R. Zhang, K. C. Yip, L. L. Chan, L. L. Chan, J. Pan, W. Wang, and Z. Wang, "An underwater robotic manipulator with soft bladders and compact depth-independent actuation," *Soft Robotics*, vol. 7, no. 5, pp. 535–549, 2020. PMID: 32109180.

[133] J. Gancet, P. Weiss, G. Antonelli, M. F. Pfingsthorn, S. Calinon, A. Turetta, C. Walen, D. Urbina, S. Govindaraj, P. Letier, X. Martinez, J. Salini, B. Chemisky, G. Indiveri, G. Casalino, P. Di Lillo, E. Simetti, D. De Palma, A. Birk, T. Fromm, C. Mueller, A. Tanwani, I. Havoutis, A. Caffaz, and L. Guilpain, "Dexterous undersea interventions with far distance onshore supervision: the dexrov project," *IFAC-PapersOnLine*, vol. 49, no. 23, pp. 414–419, 2016. 10th IFAC Conference on Control Applications in Marine SystemsCAMS 2016.

[134] R. Silva, A. Matos, and A. M. Pinto, "Multi-criteria metric to evaluate motion planners for underwater intervention," *Autonomous Robots*, vol. 46, p. 971–983, Sept. 2022.

[135] T. Coleman David, "Reducing the barrier to entry of complex robotic software: a moveit! case study," 2014.

[136] J. Meijer, Q. Lei, and M. Wisse, "Performance study of single-query motion planning for grasp execution using various manipulators," in *2017 18th International Conference on Advanced Robotics (ICAR)*, pp. 450–457, 2017.

[137] L. Kavraki, P. Svestka, J.-C. Latombe, and M. Overmars, "Probabilistic roadmaps for path planning in high-dimensional configuration spaces," *IEEE Transactions on Robotics and Automation*, vol. 12, no. 4, pp. 566–580, 1996.

[138] D. Hsu, J.-C. Latombe, and R. Motwani, "Path planning in expansive configuration spaces," in *Proceedings of International Conference on Robotics and Automation*, vol. 3, pp. 2719–2726 vol.3, 1997.

[139] D. Devaurs, T. Siméon, and J. Cortés, "Enhancing the transition-based rrt to deal with complex cost spaces," in *2013 IEEE International Conference on Robotics and Automation*, pp. 4120–4125, 2013.

[140] S. LaValle, "Rapidly-exploring random trees : a new tool for path planning," *The annual research report*, 1998.

[141] G. Sánchez and J.-C. Latombe, "A single-query bi-directional probabilistic roadmap planner with lazy collision checking," in *Robotics Research* (R. A. Jarvis and A. Zelinsky, eds.), (Berlin, Heidelberg), pp. 403–417, Springer Berlin Heidelberg, 2003.

[142] I. A. Şucan and L. E. Kavraki, *Kinodynamic Motion Planning by Interior-Exterior Cell Exploration*, pp. 449–464. Berlin, Heidelberg: Springer Berlin Heidelberg, 2010.

[143] A. M. Ladd and L. Kavraki, "Motion planning in the presence of drift, underactuation and discrete system changes," in *Robotics: Science and Systems*, 2005.

[144] J. Kuffner and S. LaValle, "Rrt-connect: An efficient approach to single-query path planning," in *Proceedings 2000 ICRA. Millennium Conference. IEEE International Conference on Robotics and Automation. Symposia Proceedings (Cat. No.00CH37065)*, vol. 2, pp. 995–1001 vol.2, 2000.

[145] B. Gipson, M. Moll, and L. E. Kavraki, "Resolution independent density estimation for motion planning in high-dimensional spaces," in *2013 IEEE International Conference on Robotics and Automation*, pp. 2437–2443, 2013.

[146] S. Karaman and E. Frazzoli, "Sampling-based algorithms for optimal motion planning," *The International Journal of Robotics Research*, vol. 30, no. 7, pp. 846–894, 2011.

[147] O. Salzman and D. Halperin, "Asymptotically near-optimal rrt for fast, high-quality motion planning," *IEEE Transactions on Robotics*, vol. 32, no. 3, pp. 473–483, 2016.

[148] R. Bohlin and L. Kavraki, "Path planning using lazy prm," in *Proceedings 2000 ICRA. Millennium Conference. IEEE International Conference on Robotics and Automation. Symposia Proceedings (Cat. No.00CH37065)*, vol. 1, pp. 521–528 vol.1, 2000.

[149] K. Hauser, "Lazy collision checking in asymptotically-optimal motion planning," in *2015 IEEE International Conference on Robotics and Automation (ICRA)*, pp. 2951–2957, 2015.

[150] A. Dobson, A. Krontiris, and K. E. Bekris, "Sparse roadmap spanners," in *Algorithmic Foundations of Robotics X* (E. Frazzoli, T. Lozano-Perez, N. Roy, and D. Rus, eds.), (Berlin, Heidelberg), pp. 279–296, Springer Berlin Heidelberg, 2013.

[151] A. Dobson and K. E. Bekris, "Improving sparse roadmap spanners," in *2013 IEEE International Conference on Robotics and Automation*, pp. 4106–4111, 2013.

[152] L. Janson, E. Schmerling, A. Clark, and M. Pavone, "Fast marching tree: a fast marching sampling-based method for optimal motion planning in many dimensions," 2015.

[153] D. Youakim, P. Ridao, N. Palomeras, F. Spadafora, D. Ribas, and M. Muzzupappa, "Moveit!: Autonomous underwater free-floating manipulation," *IEEE Robotics Automation Magazine*, vol. 24, no. 3, pp. 41–51, 2017.

[154] S. Aldhaheri, G. D. Masi, É. Pairet, and P. Ard'on, "Underwater robot manipulation: Advances, challenges and prospective ventures," *OCEANS 2022 - Chennai*, pp. 1–7, 2022.

[155] N. Palomeras, A. Peñalver, M. Massot-Campos, P. L. Negre, J. J. Fernández, P. Ridao, P. J. Sanz, and G. Oliver-Codina, "I-auv docking and panel intervention at sea," *Sensors*, vol. 16, no. 10, 2016.

[156] R. Conti, F. Fanelli, E. Meli, A. Ridolfi, and R. Costanzi, "A free floating manipulation strategy for autonomous underwater vehicles," *Robotics and Autonomous Systems*, vol. 87, pp. 133–146, Jan. 2017.

[157] G. Brantner and O. Khatib, "Controlling ocean one: Human–robot collaboration for deep-sea manipulation," *Journal of Field Robotics*, vol. 38, p. 28–51, June 2020.

[158] J. Zhou, Y. Si, and Y. Chen, "A review of subsea auv technology," *Journal of Marine Science and Engineering*, vol. 11, no. 6, 2023.

[159] A. Bircher, M. Kamel, K. Alexis, H. Oleynikova, and R. Siegwart, "Receding horizon path planning for 3d exploration and surface inspection," *Autonomous Robots*, vol. 42, p. 291–306, Nov. 2016.

[160] M. Sfakiotakis, D. Laue, and B. Davies, "An experimental undulating-fin device using the parallel bellows actuator," in *Proceedings 2001 ICRA. IEEE International Conference on Robotics and Automation (Cat. No.01CH37164)*, vol. 3, pp. 2356–2362 vol.3, 2001.

[161] H. Zheng, X. Wang, and Z. Xu, "Study on hydrodynamic performance and cfd simulation of auv," in *2017 IEEE International Conference on Information and Automation (ICIA)*, pp. 24–29, 2017.

[162] X. Ci, S. Fan, and Y. Jin, "Design and operation optimization of the flapping fin for auv propulsion," in *2019 IEEE Underwater Technology (UT)*, pp. 1–9, 2019.

[163] A. Honaryar and M. Ghiasi, "Design of a bio-inspired hull shape for an auv from hydrodynamic stability point of view through experiment and numerical analysis," *Journal of Bionic Engineering*, vol. 15, pp. 950–959, 2018. doi: 10.1007/s42235-018-0083-z.

[164] T. Sun, G. Chen, S. Yang, Y. Wang, Y. Wang, H. Tan, and L. Zhang, "Design and optimization of a bio-inspired hull shape for auv by surrogate model technology," *Engineering Applications of Computational Fluid Mechanics*, vol. 15, no. 1, pp. 1057–1074, 2021. doi: 10.1080/19942060.2021.1940287.

[165] F. E. Fish, "Advantages of aquatic animals as models for bio-inspired drones over present auv technology," *Bioinspiration & biomimetics*, vol. 15, no. 2, p. 025001, 2020. doi: 10.1088/1748-3190/ab5a34.

[166] A. Taheri, "Hydrodynamic analysis of bionic chimerical wing planforms inspired by manta ray eidonomy," *Indonesian Journal of Engineering and Science (IJES)*, vol. 2, no. 3, pp. 011–028, 2021. doi: 10.51630/ijes.v2i3.25.

[167] J. Leitão, P. Pereira, R. Campilho, and A. Pinto, "Estimation of the raya uuv hydrodynamic coefficients using openfoam," *OCEANS 2024 - Genova (in press)*, July 2024.

[168] J. Li, P. Wang, H. Dong, X. Wu, X. Chen, and C. Chen, "Shape optimisation of blended-wing-body underwater gliders based on free-form deformation," *Ships and Offshore Structures*, vol. 15, no. 3, pp. 227–235, 2020.

[169] K. W. Moored, F. E. Fish, T. H. Kemp, and H. Bart-Smith, "Batoid fishes: Inspiration for the next generation of underwater robots," *Marine Technology Society Journal*, vol. 45, no. 4, pp. 99–109, 2011.

[170] M. Y. Javaid, M. Ovinis, F. B. Hashim, A. Maimun, Y. M. Ahmed, and B. Ullah, "Effect of wing form on the hydrodynamic characteristics and dynamic stability of an underwater glider," *International Journal of Naval Architecture and Ocean Engineering*, vol. 9, no. 4, pp. 382–389, 2017.

[171] P. Zając, M. Dawidziuk, and A. Olejnik, "Stability testing method for underwater rovs," *Polish Hyperbaric Research*, vol. 74, no. 1, pp. 23–34, 2022. doi: 10.2478/phr-2021-0002.

[172] T. I. Fossen, *Marine Control Systems: Guidance, Navigation and Control of Ships, Rigs and Underwater Vehicles*. Marine Cybernetics, 2002.

[173] D. F. Campos, A. Matos, and A. M. Pinto, "Modular multi-domain aware autonomous surface vehicle for inspection," *IEEE Access*, vol. 10, pp. 113355–113375, 2022. doi: 10.1109/ACCESS.2022.3217504.

[174] A. M. Pinto, J. V. A. Marques, D. F. Campos, N. Abreu, A. Matos, M. Jussi, R. Berglund, J. Halme, P. Tikka, J. Formiga, C. Verrecchia, S. Langiano, C. Santos, N. Sá, J.-J. Stoker, F. Calderoni, S. Govindaraj, A. But, L. Gale, D. Ribas, N. Hurtós, E. Vidal, P. Ridao, P. Chieslak, N. Palomeras, S. Barberis, and L. Aceto, "Atlantis - the atlantic testing platform for maritime robotics," in *OCEANS 2021: San Diego – Porto*, pp. 1–5, 2021.

[175] D. F. Campos, E. P. Gonçalves, H. J. Campos, M. I. Pereira, and A. M. Pinto, "Nautilus: An autonomous surface vehicle with a multilayer software architecture for offshore inspection," *Journal of Field Robotics*, vol. 41, p. 966–990, Feb. 2024.

[176] P. N. Leite, P. N. Pereira, J. M. Dionísio, and A. M. Pinto, "Hybrid underwater imaging for the tri-dimensional inspection of critical structural elements in offshore platforms," *Ocean Engineering*, vol. 314, p. 119658, 2024.

[177] A. M. Pinto, H. Pinto, and A. C. Matos, "A mosaicking approach for visual mapping of large-scale environments," in *2016 International Conference on Autonomous Robot Systems and Competitions (ICARSC)*, pp. 87–93, 2016.

[178] B. Kim, J. Kim, M. Lee, M. Sung, and S.-C. Yu, "Active planning of auvs for 3d reconstruction of underwater object using imaging sonar," in *2018 IEEE/OES Autonomous Underwater Vehicle Workshop (AUV)*, pp. 1–6, 2018.

[179] J. McConnell, I. Collado-Gonzalez, and B. Englot, "Perception for underwater robots," *Current Robotics Reports*, vol. 3, p. 177–186, Oct. 2022.

[180] N. Palomeras, A. Peñalver, M. Massot-Campos, G. Vallicrosa, P. L. Negre, J. J. Fernández, P. Ridao, P. J. Sanz, G. Oliver-Codina, and A. Palomer, "I-auv docking and intervention in a subsea panel," in *2014 IEEE/RSJ International Conference on Intelligent Robots and Systems*, pp. 2279–2285, 2014.

[181] M. E. Atik and Z. Duran, "Selection of relevant geometric features using filter-based algorithms for point cloud semantic segmentation," *Electronics*, vol. 11, no. 20, 2022.

[182] N. Koenig and A. Howard, "Design and use paradigms for gazebo, an open-source multi-robot simulator," in *2004 IEEE/RSJ International Conference on Intelligent Robots and Systems (IROS) (IEEE Cat. No.04CH37566)*, vol. 3, pp. 2149–2154 vol.3, 2004.

[183] A. M. Pinto, J. V. Amorim Marques, N. Abreu, D. F. Campos, M. Inês Pereira, E. Gonçalves, H. J. Campos, P. Pereira, F. Neves, A. Matos, S. Govindaraj, and L. Durand, "Atlantis coastal testbed: A near-real playground for the testing and validation of robotics for o&m," in *OCEANS 2023 - Limerick*, pp. 1–5, 2023.

[184] T. I. Fossen, *Handbook of Marine Craft Hydrodynamics and Motion Control*. Wiley, Apr. 2011.

[185] T. Fong, "Autonomous systems in o&m – removing the barriers to bvlos operations," January 2019.